The effect of dust on the emergent spectra of galaxies; theoretical and observational approaches

by

Mohammadtaher Safarzadeh

A dissertation submitted to The Johns Hopkins University in conformity with the requirements for the degree of Doctor of Philosophy.

Baltimore, Maryland

August, 2016

Abstract

In this thesis we use state-of-the-art theoretical models to study the impact of dust on the emergent spectral energy distribution (SED) of galaxies. We propose new two-dimensional far-infrared templates based on radiative transfer simulations applied to hydro-dynamically modeled galaxies. We suggest having high gas fractions and therefore higher dust content is the reason behind the observed cold far-infrared temperatures of high redshift infrared luminous galaxies (LIRGs). We further show that high-redshift galaxies with strong infrared excesses need not be mergers; in our simulations isolated disk galaxies can populate this portion of parameter space. We show that current simplified approaches to model the dust attenuation in semi analytic frameworks does not capture the trends that are seen in the local LIRGs. We further propose a technique to overcome the confusion noise in crowded field images that can improve far-infrared photometry for high redshift galaxies.

Primary Reader: Henry C. Ferguson

Secondary Reader: Tim Heckman

Acknowledgments

I am thankful to many people whose contributions range from scientific to supportive in nature. I am thankful to my parents for always trying to provide all they could for my comfort from far away in Tehran. I am thankful to Henry C. Ferguson who became my role model in many aspects and for his continuous support. I am thankful to Renyue Cen for broadening my scope in theoretical astrophysics. I am thankful to Alireza Mortazavi who helped me a lot in my first days in Baltimore and always was there for me in times of need. To my close friend Seyed Mojtaba Koohpayeh for his encouraging words and wise suggestions that paved the way for a better living for me. To my other friends who made me laugh and enjoy my days with them.

Dedication

This thesis is dedicated to my parents Mehry and Habib and my brother Ehsan. I did not have a chance to see them while working on my Ph.D., I hope I can compensate for that a tiny bit by this dedication.

Contents

List of Figures

Chapter 1

Introduction

The light we receive from distant galaxies in the universe comes primarily from stars of different ages and masses. However, on their way to reach us these photons experience absorption and scattering by dust grains inside the galaxies themselves and potentially in the intergalactic medium. The impact of dust on these photons is a complicated phenomenon and proper understanding of it requires intensive numerical simulations that capture all the relevant physics that is involved. The intrinsic spectral energy distribution (SED) of galaxies which contains the information about various physical characteristics such as current star formation rate (SFR), star formation history and stellar mass of a galaxy is heavily modified by dust.

Based on the integrated star formation history of the universe, the share of dust is estimated to be $\Omega_{dust} \sim 1 \times 10^{-5}$ in units of present day critical mass density. Ω_{dust}(halo)$\sim 2.5 \times 10^{-6}$ for $r < r_{virial}$ and Ω_{dust}(intergalactic)$\sim 5 \times 10^{-6}$

and the amount of dust in the galaxies' halos is comparable to the dust in their disk $\Omega_{dust}(\text{disk}) \sim 4 \times 10^{-6}$ (Fukugita & Peebles, 2004; Fukugita, 2011; Ménard & Fukugita, 2012). Although a very tiny fraction of the energy budget of the universe is locked into dust, more than 50% of the UV radiation is processed by dust and re-emitted in the infrared. Based on the Cosmic Background Explorer (COBE) observations of the sky (Hauser et al., 1998) the integrated energy from 140-240 micron $\int \nu L_\nu dln\nu = 10.3\, nWm^{-2}sr^{-1}$. In comparison, the energy in the optical regime from Hubble deep field in the wavelength range of 3600 Å to 8100 Å= $4.2\, nWm^{-2}sr^{-1}$. The FIR background energy density is about a factor of 2.5 more than the optical background.

Different observational strategies are adopted to find star forming galaxies at different redshifts. Drop out techniques (Steidel et al., 1996a, 1999, 2003) are implemented to find star forming galaxies at $z > 3$ where most of the Lyman break falls into the optical passbands. The Galaxy Evolution Explorer (GALEX) FUV and near UV (NUV) bands could be used to locate the break at lower redshifts ($0.8 < z < 1.2$) and a combination of the NUV and U bands could be used to detect star forming galaxies at redshifts ($1.5 < z < 2.5$), the so called *redshift desert*. Other techniques based on ground based optical color selection (Adelberger et al., 2004) are introduced to detect star forming galaxies at ($0.8 < z < 2.5$) that are called BM/BX galaxies. Other approaches based on ground based optical colors such as B-z-K technique (Daddi et al., 2004) are devised to study star forming and passive galaxies at $1.4 < z < 2.5$. Oteo

et al. (2014) have shown that the infrared properties of these galaxies are different and that star forming BzK galaxies represent general population of star forming galaxies at $z \sim 2$.

Assessing the completeness of all these techniques requires an understanding of the effects of dust on the SEDs and the variation among galaxies of the same redshift. The star formation activity of a galaxy could be hidden in the rest frame FUV because of dust attenuation. Ignoring this fact can lead to very large errors on the estimates of the SFR. The dust-corrected cosmic SFR density is about an order of magnitude higher than the uncorrected one at its peak $z \sim 3$ (Finkelstein et al., 2015) . In the nearby universe $\sim 60\%$ of the star formation is invisible in the rest frame FUV and the fraction rises to $\sim 90\%$ at $z \sim 1.3$ (Boquien et al., 2016; Burgarella et al., 2013). The dust extinction correction to estimate the star formation rate of star forming galaxies at high redshifts (Lyman break galaxies, LBGs) is estimated to be a factor of $\sim 3 - 10$ (Adelberger & Steidel, 2000).

Dust is a necessary ingredient in theoretical predictions of the high-redshift galaxy luminosity function (Somerville et al., 2008a, 2012; Madau & Dickinson, 2014; Finkelstein et al., 2015; Bowler et al., 2015) New observations are placing constraints on when in the cosmic time the dust impact is the largest. Measuring the bright end of the luminosity function of galaxies at redshifts $z > 5$, Bowler et al. (2015) finds steepening of the bright end slope from $z \sim 7$ to $z \sim 5$ which either points to the onset of mass quenching or the onset of dust obscuration. The infrared LF evolves with

redshift as does the UV LF. Using Photoconductor Array Camera and Spectrometer (PACS) Evolutionary Probe (PEP) Survey, Gruppioni et al. (2013) discovered that the IR LF evolves with redshift out to $z \sim 4$ where the dominant contributor to the IR LF at all redshift bins are galaxies with masses $10 < \log(M/M_{\odot}) < 11$. The IR luminosity density (ρ_{IR}) increases steeply with redshift out to $z \sim 1$, then it flattens between $1 < z < 3$ and appears to decline at higher redshifts. Typical star forming galaxies at $z \sim 3$ are dusty and for the same UV slope, the dustiest high redshift galaxies are more IR luminous than the dustiest low redshift galaxies (Oteo et al., 2014). Infrared luminous LBGs at $z \sim 3$ have a median IR luminosity of $\sim 10^{12} L_{\odot}$ (Magdis et al., 2010b) while GALEX-selected LBGs at $z \sim 1$ (Oteo et al., 2013b) have IR luminosities $\sim 10^{11} L_{\odot}$ which is an order of magnitude lower in comparison.

Because the sensitivities of FIR telescopes are not high enough to detect individual normal star forming galaxies at redshifts $z > 3$, locally observed galaxies are used as proxies to estimate the SFR of high redshift galaxies. However, the nature of galaxies change across redshift, meaning two galaxies both having the same IR luminosity at two different redshifts can have very different UV-optical SEDs, sizes, masses and SFRs. As an example, the SFR estimates of the IRAC and MIPS 24 μm detected LBGs at $z \sim 3$ from UV continuum slope and IR data agree with each other even for very IR bright sources with $L_{IR} > 10^{12} L_{\odot}$ (Magdis et al., 2010a). This indicates that star formation in UV-selected ultra luminous infrared galaxies (ULIRGs) is *not* embedded in optically thick regions unlike what is found for local ULIRGs and for

distant sub-millimeter galaxies (SMGs) at $z \sim 2$. Local ULIRGs are shown to deviate from the local relation found for nearby starburst galaxies in that they are dustier at the same UV continuum slope. However, these results should be revisited in the light of new calibrations of UV continuum slope and infrared excess for the local starburst galaxies (Takeuchi et al., 2012). The fact that these LBGs follow M99 (Meurer et al., 1999a) relation indicates they are still dustier than the local starburst galaxies for the same UV slope (given the new re-calibrations of the relation), however, the fact that even ULIRG LBGs still follow the relation is correctly pointing to the fact that potentially the mode of star formation is different than what is locally observed to be embedded in optically thick regions.

Various methods are used to estimate dust masses. Fitting the FIR part of the SED with a single temperature modified black body (MBB) is the simplest approach. However, measurements of the SEDs of the nearby galaxies in the Herschel reference survey (Boselli et al., 2010, HRS) indicate that either a multi-component dust temperature is needed or the emissivity of dust needs to be modeled as wavelength dependent (Cortese et al., 2014) to explain the observations.

Dunne et al. (2011a) measures the dust mass of $z < 0.5$ galaxies selected by SPIRE at 250 μm and observes a strong evolution from $z = 0$ out to $z \sim 0.5$. The dust content of massive galaxies at $0.4 < z < 0.5$ is about 5 times larger than in the local universe. Comparing these results with the dust mass estimates of SMGs at $z \sim 2.5$ from Dunne et al. (2003), it becomes evident that dust mass function should

not be changing from $z \sim 0.5$ out to $z \sim 2.5$. By cross correlating the Planck High Frequency Instrument maps against quasars drawn from Sloan Digital Sky Survey (SDSS) DR7 across the redshift range $0 < z < 5$, Schmidt et al. (2015) find a rather constant value for the dust density at $z > 0.4$ with slight decrease at $z > 2$. Thacker et al. (2013) analyze the angular power spectrum of cosmic- FIR background in H-ATLAS maps at 250, 350 and 500 μm and their findings show the evolution of Ω_{dust} with redshift is consistent with the results of Dunne et al. (2011a).

An important question to ask is whether the dust density falls at redshifts $z > 5$. The very blue UV continuum slope of LBGs at $z > 4$ (Bouwens et al., 2009, 2012; Finkelstein et al., 2012; Bouwens et al., 2014) found by drop out techniques point to low levels of dust attenuation in star forming galaxies at very high redshifts. However, there are systems that are observed to be very bright in the FIR at $z > 5$ (Dwek et al., 2011; Michałowski, 2015b; Mancini et al., 2015) which argues in favor of dust growth in the interstellar medium (ISM) to explain the large supply of dust mass ($> 10^9 M_\odot$) in these galaxies. Whether selection biases play a role needs further investigation. Cosmological zoom-in simulations are starting to answer some of these question (McKinnon et al., 2016a). Modeling MW type galaxies with moving-mesh code AREPO and following the production, destruction and dust growth with different dust models and feedback recipes, McKinnon et al. (2016a) concludes that Type II SNe are responsible for more than two-thirds of dust mass at $z = 0$ and dust growth dominates over dust destruction. The simulation without grain growth

leads to an order of magnitude lower dust mass at $z = 0$ than simulations with grain growth. Dust to gas ratios increase by an order of magnitude from $z = 2$ to $z = 0$ and McKinnon et al. (2016a) find a significant variation in dust-to-metal ratio among halos at high redshifts. However, dust-regulated cooling of gas at high temperature is not modeled in these simulations and that can potentially lead to significantly different results due to the dominant role of ion-dust induced cooling at $T > 10^6 K$ (Ostriker & Silk, 1973).

Different sources of radiation can heat up the dust. Observations of the nearby galaxy M31 indicate that the dust temperature decreases radially outward. In the central 2 kpc region the dust is heated to temperatures $\sim$ 35K by the old (> 6Gyr) stellar population (Groves et al., 2012). This clearly indicates that the FIR emission does not need to be perfectly correlated with star formation rate and that stars with ages > 10 billion years old, if geometrically close to the dust, can heat the dust to high temperatures. Kajisawa et al. (2015) have shown that low mass stars contribute to the heating of the dust in massive galaxies out to $z \sim 1$. Dust could be heated up by sources other than stars. da Cunha et al. (2013) calculate the impact of cosmic microwave background (CMB) photons on heating of the dust at $z > 5$ and demonstrate that neglecting CMB as a source of dust heating can result in severe underestimates of dust masses from the ALMA observations at high redshifts. By studying a sample of 343 ultra luminous infrared galaxies at $0.3 < z < 2.8$ and decomposing the SEDs into emission from star formation rate and active galactic

nuclei (AGN)-powered continuum, Kirkpatrick et al. (2015) find more than 40% of IR selected sources host an AGN. This implies that AGN need to be properly modeled in cosmological simulations followed by RT post-processing in order to adequately describe the observations of ULRIGs at high redshifts.

Dust temperature depends on its proximity to stellar sources such that dust close to star forming regions will be warm enough to emit at $\lambda < 100\,\mu m$ while dust filling most of the volume in a Milky Way like galaxy will be exposed to the mean interstellar radiation field to temperatures in the range of 15-25 K (Draine et al., 2007a). Fitting the full SED from UV to sub-mm and allowing dust to have different components leads to higher values for the dust mass (Dunne et al., 2011a). The hot dust component, although small in mass, can affect the FIR SED such that a single temperature MBB fit to the FIR SED leads to underestimating the dust mass.

1.1 Size distribution and chemical properties

Dust composition seems to vary between galaxies. The type of dust found in Milky Way exhibits features that are not present in the small and large Magellanic clouds (SMC, LMC.) Moreover, whether the dust composition is silicon or carbon based can affect its efficiency for scattering the UV light from the young stars (Weingartner & Draine, 2001). The absorption and scattering efficiency of dust in the MW shows

a bump around 2175 Å (due to more efficient scattering) with a weaker presence when observing the star forming regions in SMC, LMC or distant galaxies in general. The size distribution of the grains is affected by different physical processes acting at different scales such as metal accretion on the surface of the pre-existing dust grains and grain-grain collisions. Sputtering is needed to produce dust grains with sizes $< 0.01\ \mu m$ which consequently increase the rate of grain growth because of small surface/volume ratio of the dust grains (Asano et al., 2013). Sputtering and evaporative grain-grain collisions return the metal from the dust into the gas phase of the ISM (Dwek, 1998a). The dust distribution is generally described by a power law of the form $dn/da \sim a^{-3.5}$ for grain sizes between $a_{min} \sim 50$ Å and $a_{max} \sim 0.25\ \mu m$ (Weingartner & Draine, 2001). However, smaller grains could be evaporated by radiation. For example by looking at the SED of the transitional disks around stars one can see a dip in the NIR indicative of lack of dust grains close to the star.

1.2 Production and destruction

Dust is primarily produced via two channels. One is when a low intermediate mass star (LIMS) with mass between $M_\odot < M < 8M_\odot$ becomes an Asymptotic Giant Branch (AGB) star. During this phase of stellar evolution, the light elements such as carbon and nitrogen are ejected into the ambient ISM via a stellar wind. AGB stars contribute to the formation of both carbon and silicate-based dust grains.

Whether these stars are the dominant producer of dust in the low metallicity galaxies is a matter of debate. Studying dwarf galaxies with low metallicity, Boyer et al. (2015b,a) find AGB stars to be efficient at dust production even at low metallicities.

The second channel for dust production is through supernova explosions, which can both enrich the ISM with metals (which helps the growth and construction of dust particles) and at the same time destroy the dust grains via sputtering. Heavier elements such as oxygen, iron and silicon are introduced into the ISM through this channel. Type II SNe are believed to dominate the enrichment of the ISM in early phases of the galaxy evolution and AGB stars to take over after about 100 Myr (Maeder, 1992). Silicon-based grains are primarily produced by Type II supernovae and Iron based grain by the Type Ia SNe.

Sub-mm-selected galaxies have large amounts of dust. Rowlands et al. (2014a) point out that it is extremely difficult to reconcile the estimated dust masses with our understanding of the dust production and destruction even under the most optimistic assumptions for production and destruction rates. They suggest that a top heavy IMF with no dust destruction and no grain growth can match the observed dust mass of SMGs. However, Fukugita (2011) argues that the amount of dust inside the disk of nearby galaxies together with the amount of dust in the halo are in agreement with the expected cosmological density of dust based on the integrated star formation history of the universe alone. This implies that the destruction of the dust does *not* play a significant role to reduce the global budget of dust and most of the dust

survives over the cosmic time (Ménard & Fukugita, 2012). The choice of IMF can heavily impact the total dust budget. For example a Chabrier IMF produces about 4 times more interstellar metals after 0.5 Gyr of galactic evolution than a Salpeter IMF because fewer stars with $m < 1M_{\odot}$ are produced in a given population when adopting a Chabrier IMF and therefore less metals are locked up in stars over the cosmic time. Gall et al. (2011) have found top heavy IMF and moderate dust destruction can explain the dust budget of high redshift starbursts. This increase in dust budget is related to dust production by SNe rather than LIMS-sources.

1.3 Absorption, scattering and attenuation

Dust more effectively absorbs and scatters photons with shorter wavelengths. At shorter wavelengths and entering the x-ray ($E > 0.1KeV$) regime, the extinction cross section of the dust grains becomes a decreasing function of photon's energy such that the cross section at 0.1 KeV is about $0.8 \times 10^{-21} cm^2/H$ and at 10 KeV the extinction cross section is $\sim 10^{-24} cm^2/H$. About half of the cross section for the extinction is due to scattering and the rest due to absorption (see Figure 6 of Draine, 2003b). The scattering cross section of the dust grains are calculated according to Mie theory (Bohren & Hoffman 1983) at short wavelengths ($\lambda <$grain size) and assuming spherical geometry for dust grains Draine (2003a). At longer wavelengths, the Rayleigh

scattering describes the scattering cross section where the scattering efficiency goes as $Q_{scat} \propto \lambda^{-4}$. The dust optical depth κ_λ is defined as $\kappa_\lambda = N_{gr}\sigma_{gr}Q_{ext}$ where Q_{ext} is the dimensionless extinction efficiency. The ratio of Q_{scat}/Q_{ext} is called albedo (ω). While Hydrogen atoms are the agents for absorbing the photons with $E > 13.6$ eV, dust gains dominate the absorption of the photons with $E < 13.6$ eV. However, the distribution of dust in a medium with respect to the stars can heavily affect the overall efficiency of dust absorption and scattering. If we gather all the stars at one location and put a dust layer in front of the stars (called screen model), the UV photons coming from the stars will be heavily attenuated proportional to the thickness of the dust layer in front of them. On the other hand, if we distribute the dust homogeneously with stars (called slab model) the same thickness of the dust layer does not attenuate the UV photons as effectively as our previous example. Therefore the same amount of dust, depending on its geometry with respect to the stars, impacts the outcome of the stellar light to different degrees. The questions is how is the dust distributed in real galaxies? Can we model the dust as in screen model or should we think of it as a slab model? The answer may well be dependent on the age of the stellar population (Charlot & Fall, 2000a). Young stars are embedded deeply inside the molecular cloud out of which they are formed. These clouds are primarily dusty and therefore the young stars would seem to be attenuated by dust in screen model. These stars will push away the surrounding clouds on a timescale ~ 10 Myr, and become field stars. The field stars are more mixed with gas (and dust) and therefore a slab model might

better match the status of attenuation that these stars experience.

Although the simple picture above seems intuitive, the details need to be assessed in the light of new high resolution observations of both local and high redshift universe. In order to observationally probe the physics and geometry of dust, one has to observe the galaxies in the rest frame wavelength from FUV to FIR. Such panchromatic datasets now exist for large sample of galaxies in the local universe, and for parsec scale regions of a few galaxies such as M31 (for example the PHAT survey) and the Magellanic clouds.

The shape of the re-radiated emission in the FIR by dust grains is a modified black body because grains are inefficient radiators at longer wavelengths $Q_{em} \propto \nu^{1-2}$.

$$\pi a^2 \int_0^\infty \frac{L_\nu}{4\pi d^2} Q_{abs}(\nu) d\nu = 4\pi a^2 \int_0^\infty Q_{em}(\nu) \pi B_\nu(T_{gr}) d\nu \tag{1.1}$$

Therefore the total radiated flux from a grain would scale as T_{gr}^5 or T_{gr}^6 as opposed to T_{gr}^4 which is true for a blackbody radiator.

Extinction and scattering characteristics of dust grains can be measured for stars of known SEDs, although separating these two effects would be difficult. However, when we are observing an extended object such as a galaxy, the stars of different ages and masses are mixed with dust and the light we receive in our telescopes is composed of the intrinsic light emitted from all those stars, each scattered and absorbed to different amount based on its geometry with respect to the dust in the ISM. There are various methods to arrive at attenuation law for extended objects (see Calzetti,

2001a, for a review on the current methods) and the widely used one is to use the full information in the UV-NIR range to constrain different models of dust distribution for starburst galaxies. A helpful phenomenon for starbursts is that either a burst of star formation with ages $<\sim$ few $\times 10^7$ years or a continuous star formation rate in a galaxy both have similar (around $\sim$ 13% different) intrinsic UV slope which is only modified from a galaxy to galaxy due to the nature of dust geometry and the type of dust in the galaxies (Calzetti et al., 1994a).

The overall effect is summarized as an attenuation curve and is found to be relatively constant for starburst galaxies (Calzetti et al., 1994a) which lacks the 2175Å feature and is grayer than MW extinction law slope. The origin of the Calzetti attenuation law is still a matter of debate with recent simulations suggesting a turbulent ISM structure with lognormal distribution of column densities in dusty foreground screen to reproduce the attenuation law (Fischera et al., 2003).

Conroy et al. (2010) studied the attenuation as a function of inclination for a set of nearby disk galaxies. Trends due to dust opacity alone could be singled out in such studies because the stellar populations do not correlate with inclination. Conroy et al. (2010) find that average FUV-NUV color does *not* depend on the inclination of a system, however, NUV-u and $u-r$ vary strongly. The observed trends suggest the presence of 2175 Å feature in the attenuation curve with strength of the bump $\sim$80% of the canonical MW value and $R_V = 2.1$. These observations indicate $A_{FUV} \sim A_{NUV}$ and they both increase with increasing inclination.

Battisti et al. (2016) studied the relation between the UV slope and Balmer line optical depth (τ_B^l) in ∼10,000 $z < 0.1$ star forming galaxies. Despite a rather large scatter in their data, they find correlation between the UV slope and stellar mass, SFR, metallicity and a weak negative correlation with age of the stellar population. Their derived average attenuation curve does *not* have a significant 2175 Å feature unlike the findings of Conroy et al. (2010).

1.4 Observables and detections

The radiation that is absorbed by dust is re-emitted in the form of a modified black body in the near to far infrared wavelength range with its peak around $\lambda = 100\,\mu m$ from rather large dust grains in thermal equilibrium. The small grains are stochastically heated up to very high temperatures $\sim$ 1000 K and contribute to the thermal emission at $3\,\mu m < \lambda < 40\,\mu m$. At very large attenuation levels, there will be no UV light reaching us from a star forming region in a galaxy and therefore the ongoing star formation activity will be hidden. In such situations, the dust emission in the FIR is the key to properly measuring the amount of hidden star formation rate in a galaxy. In these cases, the galaxy would look red in its SED and might appear as a dead (old) galaxy, while it can potentially have a high SFR. For example, a 20 Myr old dust-free stellar population looks like a 6 Myr system with dust attenuation of $\tau_V \sim 2$ (Calzetti, 2001a). In UV-NIR range, a non negligible degeneracy exists between dust,

age, metallicity and the initial mass function (IMF) of a stellar population.

The first FIR survey dates back to IRAS measurement of nearby galaxies in the 1980s (Hauser et al., 1984) where the observations were carried out at 12, 25, 60 and 100 microns. In 1990s the COBE satellite with the Far-infraRed Absolute Spectrophotometer (FIRAS) on its board observed the sky at $\lambda > 150\ \mu m$ out to sub-millimeter wavelengths. The FIR observations continued with cryogenic telescopes such as *Spitzer*, ISO and AKARI, but their small primary mirror ($\sim 80\,cm$) made them very much limited by confusion noise (Condon, 1974). With a large primary ($\sim 3.5\,m$) mirror, European Space Agency's *Herschel Space observatory* (Pilbratt et al., 2010a) carried out the deepest observations of the sky in the FIR between 2009-2013.

Are there other proxies for the presence of dust in a galaxy? Most of the proxies come from the low redshift observation of galaxies in that we find a correlation between the amount of dust and cold gas mass (measured with CO lines) in a galaxy and extrapolate this to higher redshifts with large uncertainties. It becomes increasing difficult to measure the dust emission at redshifts above $z > 4$ because we would only detect very luminous ones at higher redshifts. However, the space density of these galaxies drop at high redshifts because of the drop in metallicity. Young systems in the early universe had not have enough time to enrich the ISM with metals to subsequently form dust particles. Another way to account for the presence of dust would be to explore the UV continuum slope (β) of these galaxies which would be

redshifted into the visible to NIR bands based on the galaxy's redshift. Either having a high levels of dust obscuration or being an old system would lead to a red UV slope. However, for galaxies at high redshift $z > 4$ the constraints on the possible age of the stellar population can reduce the degeneracies and help us better understand the dust obscuration at high redshift. We discuss in chapter 5 how current radiative transfer simulations help us understand the variation of the β with other physical characteristics of a galaxy such as its merger state and SFR.

1.5 Radiative transfer simulations

There are two basic approaches to modeling the dust. One can use the statistical approach in which a simple model with few variables are required to match a large observed dataset composed of rest-frame colors, mass, star formation rate, redshift and morphology of the galaxies. These models are widely used for example in semi analytic models (SAM) of galaxy formation (Silva et al., 1998; Somerville et al., 2008a; Silva et al., 2012). The other approach is to do realistic simulations of galaxies where the distribution of stars and gas is motivated or set by hydro dynamical simulations of galaxies (either isolated or drawn from a cosmological simulations). These galaxies are then post-processed with radiative transfer computations to determine the final (dust scattered) rest frame color of the galaxies. These datasets can be compared with observations to reveal how well our current understanding of galaxy formation

and dust processing are representative of the real world (Jonsson, 2006; Jonsson et al., 2010; Younger et al., 2009a; Narayanan et al., 2010a; Hayward et al., 2011a, 2012; Snyder et al., 2011, 2013; Lanz et al., 2014).

These models are all based on many different assumptions, some of which could play a non-negligible role in the final outcome of the simulations. It is shown that SAMs in general have difficultly to match the observed sub-mm number counts. Baugh et al. (2005a) have shown incorporating a top-heavy IMF in the starburst phase can reproduce the observed number counts while matching the observed LBG distribution at high z and $z = 0$ K-band luminosity function and IRAS 60 μm LF. This result is later challenged by high resolution 3D hydrodynamical simulation of isolated disks and mergers post-processed with dusty radiative transfer simulations (Hayward et al., 2011b). Hayward et al. (2011b) showed there is no need to invoke top-heavy IMF to match the observed number counts due to long sub-mm duty cycle for mergers.

At some level, it would be out of the scope of SAMs to account for all the relevant physics because of the computational feasibility. If it were computationally feasible, one would rather do a direct simulation of dust and gas in realistically simulated environment than trying to model the many different relevant physics by fitting formulas.

Another approach to model the panchromatic SEDs of the galaxies is advocated by da Cunha et al. (2008, MAGPHYS). In this model the dust emission SED in

stellar birth clouds is computed from the sum of three components: a component of polycyclic aromatic hydrocarbons (PAHs); a mid-infrared continuum characterizing the emission from warm grains at temperatures in the range 130 - 250 K; and a component of cold grains in thermal equilibrium with adjustable temperature between 30 - 60 K. In the ambient ISM, an extra component of cold grains is included with adjustable temperatures 15 - 25 K. The fractional contributions of the four components $\xi_{\rm PAH}, \xi_{\rm MIR}, \xi_{WM}$, and ξ_C are varied separately for stellar birth clouds and for the diffuse ISM. SED libraries can be constructed for any choice of these parameters. MAGPHYS libraries consist of 25000 optical SEDs covering the FUV-NIR wavelength range and 25000 Infrared SEDs covering NIR-FIR. The two libraries are connected to each other based on total L_{dust} and requiring the absorbed and the re-radiated parts of the spectrum to have f_μ within 15% of each other, where f_μ is the fraction of L_{dust} that is coming from the ISM rather than the birth clouds. MAGPHYS has been used extensively in studies of SEDs and dust contents of the galaxies, such as in Herschel-ATLAS survey (Rowlands et al., 2014b; Dunne et al., 2011a). MAGPHYS has also been shown to give consistent result in estimating the SFR of hydro-dynamically simulated galaxies where the true SFR is known (Hayward & Smith, 2015).

Although libraries such as MAGPHYS are becoming popular, one still needs to generate a realistic panchromatic SED to further test the successes and shortcomings of these approaches. The library needs to be tested for extreme cases such as ULIRGs and our own analysis has shown there to be a bias with respect to the estimates of

hidden star formation rate in MAGPHYS libraries.

It is desirable to generate SEDs that we believe are the closest to the reality of observed galaxies. This goal makes us enter the world of radiative transfer simulations. Early dusty radiative transfer simulations adopted on simplified assumptions about the geometry of dust with respect to stars (Witt & Gordon, 1996a, 2000a; Gordon et al., 2001a; Misselt et al., 2001a; Silva et al., 1998; Efstathiou et al., 2000; Takagi et al., 2003; De Geyter et al., 2014) or AGN (e.g., Fritz et al. 2006; Siebenmorgen & Krügel 2007; Stalevski et al. 2012). More recent simulations have explored more complicated geometries (Dopita et al., 2005; Popescu et al., 2011; De Looze et al., 2011, 2014; De Geyter et al., 2015). These simulations have been qualitatively successful in generating SEDs similar to those observed. For example, Witt & Gordon (2000a) find that the Calzetti attenuation law could be explained if the dust model used is SMC type and if the geometry of dust with respect to the stars is a clumpy shell-type distribution.

Performing three-dimensional (3D) dust radiative transfer on the outputs of hydrodynamical simulations of galaxies in post-processing is now a popular approach (e.g. Jonsson, 2006; Jonsson et al., 2006, 2010; Chakrabarti et al., 2007, 2008; Chakrabarti & Whitney, 2008; Narayanan et al., 2010b,a; Hayward et al., 2011a, 2012; Snyder et al., 2013; Lanz et al., 2014; Granato et al., 2015). Even here, one needs to adopt an approach for the sub-grid modeling. The hydro simulations at best have a resolution of about tens of parsecs and we would need a prescription on how to model physical

processes below these scales which relates to resolving the HII regions. The solution adopted by (Jonsson, 2006; Jonsson et al., 2006, 2010) is to use MAPPINGSIII photoionization code (Dopita et al., 2005; Groves et al., 2008) to model the subgrid physics and model the larger scales with Monte Carlo radiative transfer simulation.

In this thesis we delve into several different, inter-twined, topics aimed at improving our understating of dust's effect in reprocessing the stellar light. In the second chapter we discuss source confusion in FIR observations and how to improve them by novel techniques. Developing better 'priors' for this photometry project was the motivation for much of the theoretical work in later chapters. In the third chapter we discuss the nature of FIR SEDs from the radiative transfer simulations. These simulations are performed as a post-processing step on hydro-dynamically simulated galaxies representative of both low and high redshift universe. Our approach to analyze these dataset is Principle Component Analysis (PCA) and by finding the Eigen FIR SEDs, we explain puzzling observations that high redshift galaxies tend to have lower dust temperature at fixed IR luminosity. In the fourth chapter we extend our analysis of the radiative transfer output to UV regime and combine the information in UV and FIR to explain how the information in the UV wavelength is coupled with the information in the FIR. We show that dusty star forming galaxies (DSFGs), IR luminous high redshift galaxies with high star formation rates, can be both isolated disks and merger systems. In Chapter five, we discuss the power and shortcomings of the simple dust treatments that are widely used in the Semi Analytic Model (SAMs).

We show that a simple implementation of the prescription provided by Charlot & Fall (2000a) falls short of explaining the observations of local (Ultra)Luminous Infrared Galaxies (LIRGs). We propose solutions to fix this issue in the current implementations which involves including a population of young stars that are not heavily embedded in dust.

Chapter 2

The problem of confusion noise

2.1 Introduction

A significant fraction of the radiation emitted by stars and Active Galactic Nuclei (AGN) over the lifetime of the universe is absorbed by dust and re-radiated at long wavelengths. It is thus crucial to measure this re-emitted radiation and develop an understanding of how dusty radiative transfer evolves in galaxies over cosmic time. There has been a revolution over the past two decades in our ability to measure far-infrared (FIR) radiation, with the increasing sensitivity of sub-mm telescopes and detectors and with the launch of the *Herschel* Far-infrared Observatory (Pilbratt et al., 2010a). However, at the flux levels relevant for typical galaxies at redshifts $z > 1$, our deepest images of the sky at wavelengths 24-1000μm are dominated by confusion noise (Condon 1974). If we were to boost the Milky Way′s star-formation

rate (SFR) by a factor of 100, it still would not be detectable in the deepest Herschel images if it were placed at redshifts $z > 2$. Furthermore, the main-sequence of star-forming galaxies (Elbaz et al., 2011; Noeske et al., 2007) drops below the confusion limit at $z > 2$ (Magnelli et al., 2013a). It is therefore important to find techniques to overcome or mitigate confusion noise.

Currently studies of the massive end of the main sequence of star-forming galaxies at $z > 2$ in the FIR have been limited to stacking analysis. Stacking has the intrinsic assumption that the underlying distribution of galaxies is a normal distribution where the mean and median are well behaved. Furthermore, the median or mean of some derived physical quantity for a sample of galaxies is not necessarily the same as the value for that physical quantity derived from the mean or median of the stacks (Ryan et al., 2014; Vargas et al., 2014). In stacking, the presence of local background around a particular object can skew the final results. Moreover, because galaxies are clustered, a portion of any detected signal could be due to physical neighbors. Detected sources are often subtracted before doing the stacking (to improve the S/N), but this risks subtracting a portion of the flux of the sources of interest. In addition, the estimate for the mean optical/FIR flux ratio from the stacks can be biased by sources in the tails of the distribution. Therefore individual detections (i.e. not stacked photometry) of high redshift galaxies will provide more reliable estimates of their SFRs; however source confusion restricts the ability to detect faint objects and de-blend neighbors. FIR studies of individual high redshift lensed galaxies are

currently limited to a small number of systems (e.g. Egami et al., 2010).

Confusion noise was first recognized in the context of deep radioastronomical observations (Scheuer, 1957). An image can be considered as confusion limited when the uncertainties in the measured fluxes of the sources are dominated by the uncertainties due to overlapping sources. Murdoch et al. (1973) discussed two types of confusion: blending confusion which comes from a high number density of faint (but detectable if observed individually) sources in the beam and the latter photometric confusion which is due to sources with fluxes less than the instrumental detection limit (S_{lim}). The quadrature sum of these two causes of photometric scatter is designated as confusion noise σ_{conf}.

Apart from radio astronomy (Blain et al., 1998; Condon, 1974; Condon et al., 2012), confusion noise is important for many other types of observations as well, such as FIR observations (Nguyen et al., 2010; Magnelli et al., 2013a; Kennedy & Wyatt, 2012), X-ray deep observations (Barcons & Fabian, 1990; Barcons, 1992), gravitational waves (Crowder & Cornish, 2004), weak lensing (Melchior & Viola, 2012), Sunyaev-Zel'dovich (SZ) cluster surveys (Bartlett & Melin, 2006), high precision astrometry (Hogg, 2001) and studies of the galactic center (Eckart et al., 2012; Stone et al., 2012).

A typical rule of thumb has been that one reaches diminishing returns when there are more than 1/30 sources per beam. The classic treatment of source confusion assumes that you know nothing about the sources other than their statistical density

on the sky. Moreover, it is assumed that the sources are distributed uniformly on the sky with Poisson statistics. However, we know galaxies are clustered and this changes the confusion noise limit (Takeuchi & Ishii, 2004; Negrello et al., 2004; Barcons, 1992).

It is useful to consider an alternative hypothetical case, where one knows everything about all the sources in the image, even below the detection limit, except for one source. In this case, all of the contaminating sources can be subtracted perfectly. One is left with just the detector noise, residual Poisson noise from the subtracted sources and noise from the smooth sky background (cirrus and zodiacal dust in the case of FIR observations). The source in question is no longer contaminated by confusion. Provided there is not a systematic noise floor, the photometric uncertainty for this source will beat down as the square root of the exposure time.

For deep extragalactic surveys, reality is somewhere in between these two idealized cases. The detected source density in the deepest PACS (Poglitsch et al., 2010) 160μm images is ~ 3.1 sources arcmin^{-2} (Magnelli et al., 2013a). In the same region of the sky, the average detected source density in the shallowest tier of the *Hubble* CANDELS (Koekemoer et al., 2011; Grogin et al., 2011) $1.6\mu m$ image is $\sim$200 arcmin^{-2} and for the Hubble Ultra-Deep Field (HUDF, Beckwith et al., 2006) is $\sim$1200 arcmin^{-2}. This is illustrated in Figure 2.1.

From existing archival data, we have excellent estimates on the position, redshift (spectroscopic and photometric), UV–NIR SED shape, morphology, size and axis ratio of sources that are *not* individually detected by *Herschel*, with which we can

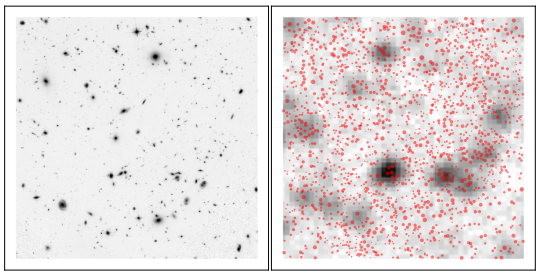

Figure 2.1: Illustration of the confusion problem. On the left is the *Hubble* image of the Ultra-Deep Field at 1.6μm . On the right is the deepest *Herschel* PACS 160μm image of the same field. The positions of the sources detected in the *Hubble* image (red dots) are overlaid on the *Herschel* image with their size proportional to their H band magnitude.

constrain their L_{IR} (Wuyts et al., 2011). To date, none of this information has been used to help reduce the confusion in the *Herschel* images. In this paper we show that provided we can constrain the L_{IR} of the galaxies to within an order of magnitude using all the above properties, we can reduce the confusion noise significantly and obtain reliable photometry for much fainter objects.

2.2 Method

The procedure for improving the *Herschel* photometry using Bayesian priors is outlined in Figure 2.2 using a PACS-160μm image as an example. We need both positional and flux priors for every single source that is detected in the *Hubble* image. The positions come from *Hubble* H band imaging and we assume a delta function for the position of the source. Due to PACS much lower resolution compared with the *Hubble* , all the sources are considered as point source in this analysis. The flux

priors from both analyzing the PACS-160μm image and also the short wavelength ($\lambda < 2\mu$m) SED fitting of the sources that are detected in the *Hubble* images using a mock library of SEDs(sections 2.2.1,2.2.2). For each source, we only need a rough estimate of the PACS-160μm flux to be within ± 1 dex of the corresponding true value. We use our best-guess prediction for the PACS-160μm fluxes (section 2.2.3) of the sources along with their positions to feed a graphical algorithm (section 2.2.4) which breaks the image into smaller regions each identifying the blended groups. Subject to the positional and flux priors, a Markov Chain Monte Carlo (MCMC) simulation is run for each blended group with the number of dimensions being the number of sources with an additional background level to produce an estimate for the full posterior distribution of the flux of each source (section 2.2.5).

2.2.1 Library

The library we propose to use for SED fitting and estimating the FIR flux of a given source is a set of simulated CANDELS light cones based on SAMs (Somerville et al., 2008a, 2012; Fontanot et al., 2009a; Lu et al., 2014a). The library should be large enough so that cosmic variance would not play a major role and using all of the CANDELS fields' light cones reduces the cosmic variance to the desired level. The SAM is applied on a set of halo merger trees extracted from a large cosmological N-body simulation which has a box size of $250h^{-1}\,Mpc$ on a side with a mass resolution to follow galaxies with a stellar mass $\sim 10^8 M_\odot$. Following the merger trees, the model

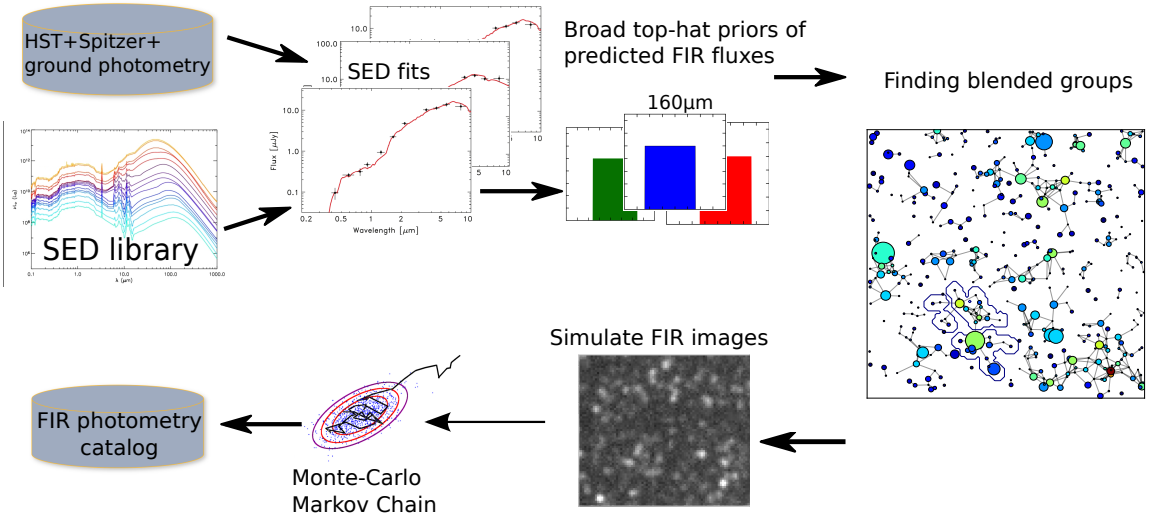

Figure 2.2: Illustration of the fitting procedure. Semi-analytical models are used to generate an SED library based on realistic star-forming histories and chemical evolution and dust treatment. The SEDs are compared to the HST+*Spitzer* +ground-based photometry. This comparison yields a probability distribution function (PDF) for predicted fluxes in each FIR band, which we broaden into top-hat PDFs centered on the peak of the PDF from the SED fit, illustrated in the top center of this diagram. The sources predicted to be brighter than some minimum flux are grouped together based on criteria that combine proximity and predicted brightness of the neighbors. Each circle shows one source with its size being proportional to the source's predicted flux. Each circle is color coded based on the number of neighbors it has. The contour plot around one of the disjoint graphs shows the pixels that are fit simultaneously for that group of sources. The sources in the disjoint graphs with an additional parameter accounting for the background are simultaneously fit and the posterior distributions are determined via a MCMC simulation.

calculates the rates of gas cooling, star formation, outflow induced by star formation feedback, and galaxy-galaxy mergers. The model predicts realistic star formation histories and metallicity histories for (a number) galaxies in the entire volume in a cosmological context. These are used to produce SEDs based on the BC03 model for the library. The SED library includes normal star forming, quiescent and starburst galaxies. In this set of SAM SEDs, FIR flux of galaxies are estimated via a slab model for dust attenuation and estimating the amount of absorbed starlight (L_{IR}) based on inclination of the model galaxy and its face on optical depth value. The FIR flux in each band is based on the shape of the FIR SED via templates of Chary & Elbaz (2001a) while other templates could be used as well.

2.2.2 Priors

Our priors consist of strong positional priors and weak flux priors for the sources. Positions of the sources are taken from a deep, high-resolution image from the *Hubble* Space Telescope. For the CANDELS fields, the detection band will generally be at 1.6μm , with a spatial resolution of about 0.1 arc seconds. SExtractor (Bertin & Arnouts, 1996) is used for the source detection, and used for PSF-matched photometry of the sources in the *Hubble* images. Our fitting technique requires priors for the FIR fluxes for every source detected in the *Hubble* images. However, we find that these can be reasonably weak ($\pm$1 dex in flux) and still yield good photometry for most sources. We have verified that we generally are able to predict the FIR fluxes of

galaxies at low redshift to within ±1 dex using only their SEDs at $\lambda < 2\mu$m for a sample of local normal star forming galaxies in SINGS sample (Kennicutt Jr et al., 2003a) and LIRGs in GOALS sample (Armus et al., 2009a). Apart from being able to estimate the L_{IR} for a given galaxy, a portion of the uncertainty for high redshift galaxies comes from the error in the photometric redshift estimates. Currently the uncertainty $\delta z/(1+z)$ is about 0.06 (Dahlen et al., 2013) in the CANDELS data which suggests that its effect on the SED fitting derived quantities will be negligible. However 5% of the sources are outliers with the true redshifts significantly different from photo-z estimates. While the SED fits produce full probability distribution functions (PDFs) for the mid- and far-IR fluxes in each band, to avoid too much reliance on the SED models, we turn these PDFs into broad (2.2 dex wide) top-hat priors which are centered on the peak of each source's flux PDF.

2.2.3 Initial source's flux estimate

Our fitting procedure begins with an initial guess for the 160μm flux for each source. These initial guesses are used to find the blended group of the sources which is the next step in our de-confusion method. For sources brighter than $3\sigma_{conf}$, the initial guess is based on the measured flux with the standard PSF matching photometry technique (Magnelli et al., 2013a).

For sources fainter than $3\sigma_{conf}$, our initial guess will based on SED fitting. The SED for each source is fit using a library of SEDs we described in section 2.2.1. The

fits use photometry short-wards of rest-frame 2μm – i.e. light dominated by dust attenuated stellar emission. Ideally, we would like to use as much information as possible to make this prediction, including the spectroscopic redshift, the full SED from UV to mid-IR, and possibly the galaxy axial ratio, size and morphology. For this proof-of-concept, we have simply assumed that for every galaxy that is detected in *Hubble* images, we can predict the *Herschel* PACS-160μm flux to within an order of magnitude. As described later, we expect that we can generally identify post-facto the cases where this prediction has failed, and iterate the procedure to address this.

2.2.4 Decomposing domains for image fitting using graphs

In analyzing the PACS image, it is computationally convenient to split the image into subsections to be analyzed separately. The benefit of doing this is the reduction of the computation time and parallelization of the process among different CPUs. Each CPU will be given one patch to analyze without interfering with other CPUs.In this method we use graphs to identify the most blended groups of sources in the PACS image. The graph is constructed on the PACS image but the sources (nodes) that makes up the graph are those sources that are detected in the *Hubble* image. Each node is connected to other nodes in the PACS image if there is a strong interaction between them according to their predicted PACS-160μm flux and distance from each

other. The flux in a given PACS pixel at $\mathbf{r}$ from a source x at position r_0 is:

$$F'_{\mathbf{r}} = F_{x,\mathbf{r_0}} * PSF(\mathbf{r}, \mathbf{r_0}) \tag{2.1}$$

if $F'_{\mathbf{r}} > \alpha \times F_{y,\mathbf{r}}$,then sources x and y are connected with each other. For a PSF centered at $\mathbf{r_0}$, $PSF(\mathbf{r}, \mathbf{r_0})$ gives its value at position $\mathbf{r}$ (the PSF is normalized such as its central pixel value is 1) and * denotes the convolution operation. α is the sensitivity parameter. $\alpha = 1$ implies we only connect source A and source B if flux of source A at the position of source B is more than flux of source B at its central pixel position. $\alpha = 0.1$ would imply connecting sources A and source B if flux of source A at the position of source B is more than 10% of flux of source B at its own central pixel position (so more sensitivity). In this paper, we have used $\alpha = 0.5$ (lower values of α will result into large graphs that expand the whole image whose analysis is computationally expensive). The result is a set of disjoint graphs that can be independently analyzed. We separately focus on each disjoint graph, select pixels that encompass that graph and constrain ourselves to those pixels when fitting the image.

2.2.5 Fitting the image

Sources in a blended group have to be fit simultaneously. Due to the dispersion of the fluxes of the sources that are not detected by PSF matching technique, the

resulting graphs have a different connectivity of nodes than the graph based on the true input fluxes, but this is what will happen in reality. Figure 2.3 shows the result of grouping the sources after dispersing their true fluxes by 1 dex. We draw a contour around one of the isolated graphs to show the pixels that will be analyzed in studying the sources in that particular blended group of sources.

We select a disjoint group of blended sources in the simulated PACS-160μm image and estimate their flux through MCMC sampling. We chose to implement EMCEE, a python based affine invariant sampler for our purpose (Foreman-Mackey et al., 2013). The EMCEE algorithm would have failed if we were using weak positional priors because of the label-switching degeneracy. A standard Metropolis algorithm would work better in that case. The convergence of the chains are based on the Gelman-Rubin test (Gelman & Rubin, 1992) and requiring the $\chi^2_r = \chi^2/(N_p - N_s - 1)$ to be close to 1. N_p is the number of pixels we use to fit when estimating the flux of N_s blended sources together. χ^2 is defined as:

$$\chi^2 = \sum_{j=1}^{N_p} \frac{(\sum_{i=1}^{N_s} F_i * PSF_{i,j} - I_j)^2}{\sigma^2_{RMS}} \tag{2.2}$$

where F_i is the flux of source i and $PSF_{i,j}$ gives the value of the PSF (centered on the position of source i) at the pixel j and * denotes the convolution operation. I_j is the value of pixel j flux in the image. σ_{RMS} is the instrumental pixel noise of the image which is the same as the science image. The variables we fit for are flux (F_i) of N_s

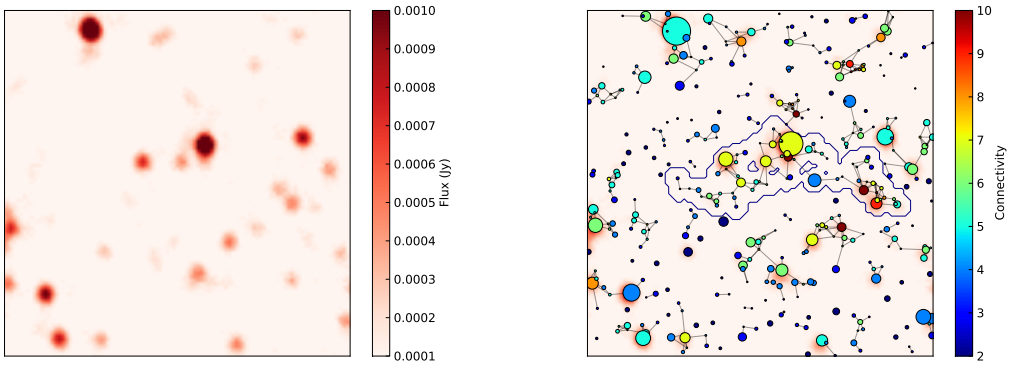

Figure 2.3: The process of fitting the simulated images. Panel (a) shows a section of the simulated PACS-160μm the image of GOODS-S field. Panel (b) shows the same image overlaid with the graph whose nodes represents the galaxies and color coded by the number of neighbors each node (galaxy) has. The size of each node is proportional to the galaxy's flux and in this image we use true flux for each node (fluxes are not dispersed). The presence of an edge between two nodes in the graph implies strong influence of one's flux on the other due to proximity and brightness. We have dispersed the flux of the sources that are not detected in the PSF matching analysis by 1 dex and then constructed the graphs. The contour plot around one of the disjoint graphs shows the pixels that we fit for in order to infer the flux of the blended sources in that graph. In panel (b), the color of each point indicates the number of neighbors of each node, as indicated on the color bar.

sources with an additional background level flux that is not zero due to the presence of faint sources. The likelihood function L is defined as:

$$\ln L = \frac{-\chi^2}{2} \tag{2.3}$$

2.3 Test of the method

In this section we present a demonstration of the technique we proposed on a simulated PACS-160μm image.

2.3.1 Constructing simulated PACS-160μm image

In order to account for the effect of clustering on the resulting confusion noise, for our simulations we use the actual positions of detected sources in the CANDELS GOODS-S catalog. For the purposes of our simulation, we need only a plausible SED from the optical through the FIR, not one that is necessarily close to the truth for that galaxy. We use a custom-generated GOODS-South light cone mock catalog constructed from a SAM (Somerville et al., 2008a, 2012; Fontanot et al., 2009a) to provide the library of physically plausible galaxy SEDs. For each galaxy in the CANDELS image, we select galaxy at random from this catalog within 0.5 mag in H-band apparent magnitude and 0.05 in redshift. These are inserted as point sources–as the intrinsic size of the galaxies in GOODS-S PACS images is negligible– and convolved with *Herschel* PACS-160μm PSF without adding a background level to the image. Noise is added to the image from the RMS map of PACS science image. Figure 2.4 illustrates the statistical similarity between our simulated image and the science image of PACS-160μm of GOODS-South field.

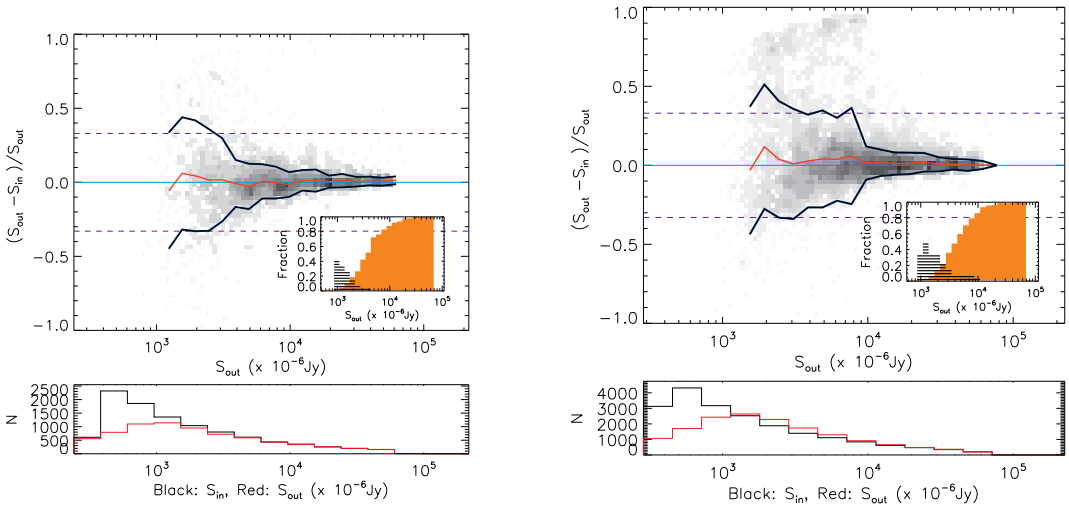

Figure 2.4: a)Results of MC simulations in the GOODS-South field using PSF matching method. Blue lines represent the average photometric accuracy defined as the standard deviation of the $(S_{out} - S_{in})/S_{out}$ distribution in each flux bin (after 3σ clipping). Red lines show the mean value of the $(S_{out} - S_{in})/S_{out}$ distribution in each flux bin. Inset plots show the fraction of artificial sources detected in the image (i.e., completeness) as a function of input flux (orange plain histogram) and the fraction of spurious sources (i.e., contamination) as a function of flux density (striped black histogram). b)Results of MC simulations on our simulated PACS-160μm image. The lines are the same as in (a). The science and simulated PACS-160μm images are statistically similar.

2.3.2 Flux priors and initial guesses

We analyze the simulated PACS-160μm image with PSF matching photometric technique (Magnelli et al., 2013a) and for sources which are detected to be brighter than $3\sigma_{conf}$, we use their measured flux as our initial guess. In order to do so, we simulated the corresponding *Spitzer* MIPS 24μm and *Spitzer* IRAC Ch1 of our PACS-160μm simulated image. In PSF matching technique, the MIPS and IRAC images are used as priors for analyzing the PACS image. The current procedure for source detection and construction of the current *Herschel* catalogue is outlined in Elbaz et al. (2011); Magnelli et al. (2013a).

For sources fainter than $3\sigma_{conf}$ in the PACS image, because in our simulation we know the true flux of the sources, we disperse their flux by drawing from a uniform random deviate within a range ±1 dex of the true value to mimic our ability in predicting the FIR fluxes to within an order of magnitude and use that as our initial guess. It should be noted that although we propose to use SAMs libraries for SED fitting and use the predicted FIR flux as the initial guess, for the demonstration of the method, we only disperse the fluxes to within ±1 dex to mimic our inability to predict the precise FIR flux of the sources. If we were to use the SAMs library to predict the FIR flux via SED fitting, as our sources are drawn from the same library, the predictions would have been unrealistically close to the true values.

2.3.3 Results

For a given blended group of sources that we analyze with our technique, we compare our result with the standard photometry technique (Magnelli et al., 2013a; Elbaz et al., 2011) on the same set of sources. The result is presented in Figure 2.5. In the standard technique, sources with true flux fainter that $3\sigma_{conf}$ of 2.7 mJy are barely detected. For sources below this limit, only statistical upper limits are provided, based on the overall confusion noise of the image, not an upper limit based on the crowding of each individual source. Even for sources that are brighter than this limit, flux estimates from the standard technique to be biased high relative to the true fluxes, due to the contribution of nearby neighbors. The de-confusion method presented in this paper is able to probe sources as faint as the instrumental noise limit giving a posterior PDF for each individual source. The overall performance comparison of de-confusing technique and the standard technique is illustrated in Figure 2.6. We define the outlier fraction (OLF) as the fraction of the sources whose measured flux is 5σ (σ denoted the uncertainty on the measured flux) away from the true flux. For sources brighter than $3\sigma_{conf}$, the OLF is about 4% in the standard method and 0% in the de-confusion method. For fainter sources, while there is no detection in the standard technique, the OLF is about 5% in de-confusion technique.

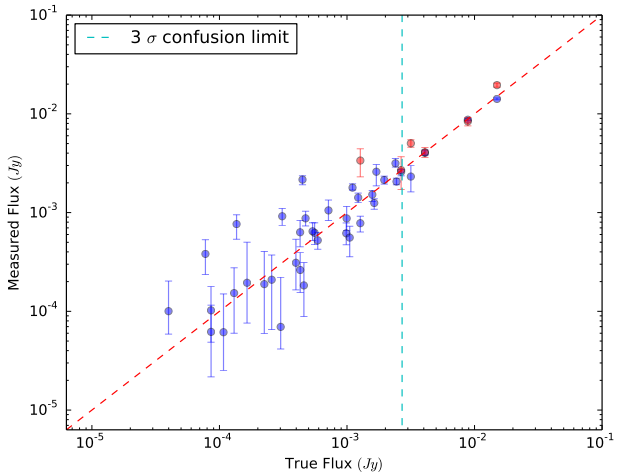

Figure 2.5: The measured flux from our method (Blue dots) compared with the fluxes estimated from the more conventional technique of Magnelli et al. (2013a) (in red). Only about 10% of the sources brighter than instrumental noise limit (0.2 mJy) are detected in (Magnelli et al., 2013a). The $3\sigma_{conf}$ is 2.7 mJy in our simulated image which is shown by the blue vertical line.

2.4 Summary and Discussions

We have demonstrated via simulations that we are able to obtain reliable fluxes for sources significantly below the nominal confusion limit of the deepest 160μm *Herschel* images. To achieve this, we use strong priors on source positions and weak top-hat priors of ± 1 dex wide on source fluxes. We also assume perfect knowledge of the point-spread function.

In a confused image, it is crucial to simultaneously estimate the flux of sources that are strongly affect by each other due to their proximity in position and relative brightness. In order to do so, we have developed a graphical method for identifying sources that need to be fit simultaneously. This also makes the problem computa-

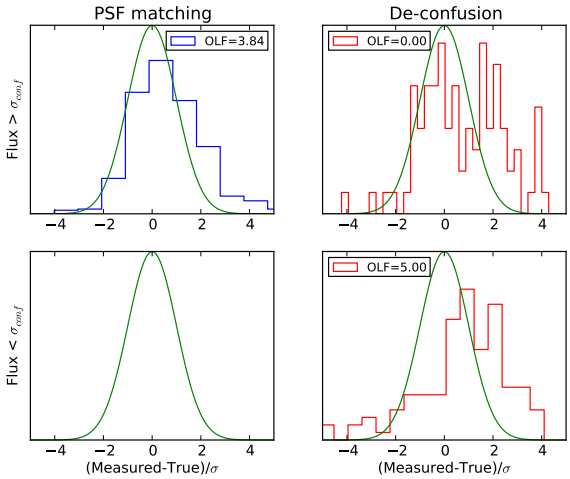

Figure 2.6: Comparison of the percentage of the OLF (defined in the text) of de-confusion method and the standard photometry on a simulated PACS-160μm image. The top row shows the result of flux measurement of sources that are detected to be brighter than the $1\sigma_{conf}$ in the simulated image. The bottom row shows the result for the sources that are detected to be below the $1\sigma_{conf}$. There is no source detected below this limit in the standard photometry technique while our method only results in OLF of 5%. Due to the computational costs of the MCMC, we have run our demonstration on only about a quarter of the image. Therefore the number of sources shown in the top panel is about four times larger for the PSF-matching technique (left) than for our de-confusion technique (right). In all the panels, the green is a Gaussian curve with mean zero and standard deviation of 1. The histograms would follow the green curve if sources were isolated (not blended) and the background noise is gaussian.

tionally tractable as we do not have to fit for all the HST sources in the image at once. This segregation results in imperfect estimates of photometry and uncertainties for some sources. Nevertheless, our simulations indicate that both our fluxes and our uncertainties appear to be generally reliable down to 1 mJy, which is a factor of ~ 3 below the nominal $3\sigma_{conf}$ confusion limit.

In our proposed method we have used top hat priors based on the assumption that the FIR flux of the sources could be predicted to within an order of magnitude. The top hat prior then is wide enough to encompass the true flux of the source about 95% of the time. Relative to a Gaussian, this flattens the core at the expense of chopping off the wings of the distribution. If we had adopted a Gaussian with the same 95% confidence interval of 1 dex, the initial guesses would be closer to the truth much more often than for our flat prior. Therefore, we believe using a top hat prior is sufficiently conservative. Nevertheless, we expect this to fail 5% of the time. In the case of real data where we do not know which sources have good photometry in our technique, there are various tests that can be carried out to identify possible problems. We discuss how to identify these cases in the following paragraphs. A final advantage is the following: for many uses of a general photometry catalog, one will be using and plotting some measure of the most probable value of the flux, and not using the whole PDF. With a peaked distribution for the prior, in the case where the the Herschel photometry is not completely determinative, the peak of the posterior PDF will be biased toward the peak of the prior PDF. Many users of a photometry

catalog may be uncomfortable with this behavior.

(1) Analyzing the residual image: Comparing the result of the image based on the predicted fluxes with the original image can reveal if there was a source not included in the set of priors or in the group that was simultaneously de-blended. This could also be revealed in the χ_r^2 value of the fits as well. Examining the residual image is also a way to check for the positional registration between the low and high resolution images. If there are zonal mis-registrations then the "registration dance" approach adopted by TFIT (Laidler et al., 2007) is a possible solution.

(2) Repeat the flux estimation within a different graph. Using different initial guesses for the fluxes of sources will result in different connectivity between sources, and hence different blended groups of sources that will be simultaneously fit. Repeating the photometry with a variety of initial guesses will then provide multiple flux estimates for each source, and sources with a wide range of predicted fluxes can be more easily identified and flagged.

(3) Decreasing α. The parameter α which is described in section 2.2.4, determines what sources are considered to be in a given blended group. Decreasing α will result in having more sources joining a given blended group and increases the number of sources that have to be fit simultaneously. Although higher number of sources to fit simultaneously will be more computationally expensive, the resulting photometry is more accurate. If there is a faint source whose flux is easily affected by other far distant sources, decreasing α to values around 0.1 or even less could help improve the

photometry.

(4) We expect that there will be a few optically-undetected Herschel sources in each CANDELS field. This will lead to posterior PDFs for a few groups of sources that are catastrophically wrong. Cases like this can be revealed by comparing the initial guesses to the measured fluxes, and examining cases where the fluxes moved unusually far (and generally became brighter) than the initial guesses.

2.5 Future improvements

While we consider the method we have outlined so far to be robust enough already to construct a good photometric catalog, there are various ways in which it can be improved and extended. We briefly outline these here.

(1) Improving the priors. We show in a companion paper (Safarzadeh et al 2016 in preparation) that we can typically predict FIR fluxes of low-redshift galaxies to within ± 1 dex using existing SAM SED libraries. Compared to local star-forming galaxies, main-sequence galaxies (Noeske et al., 2007) at high redshift have higher SFR (Whitaker et al., 2012), higher gas fractions (Magdis et al. 2012a; Daddi et al. 2010), smaller sizes (van der Wel et al., 2014) and chemistry (Magdis et al., 2010a). SAMs have been successful at generating the same trend for high redshift galaxies and we intend to use SAM libraries for predicting the FIR flux of high redshift galaxies. For the first-generation catalog, we envision using the results of SED fitting of the

photometry short wards of rest-frame 2μm to predict the FIR fluxes. However, we are well aware that this is not ideal and there is room for improvement by considering other information such as galaxies size, axial ratio and morphology.

(2) Fit multiple bands. The demonstration here used only the *Herschel* PACS-160μm image (although we used the simulated IRAC 3.6μm and MIPS 24μm images to drive the standard PSF-fitting photometry for the simulation). Our goal is to apply the de-confusion technique to all the FIR bands in order to weed out sources with discrepant photometry. For example, if the measured observed 160μm flux is significantly different from the measured 100μm flux, the measured photometry should be flagged. The most important bands to include are those in SPIRE, which are heavily confused for most of the sources of interest at $z > 2$.

(3) De-confusing the PACS-100μm and 160μm images will give us the rest frame 40μm and $\sim$ 50μm for a $z \sim 3$ galaxy, which is not very close to the peak of the FIR SED. However, de-confusing the SPIRE (Nguyen et al., 2010) images – which trace the peak of FIR emission for galaxies at $z \sim 3$ – can better constrain the FIR luminosity. In order to fit the SPIRE images, we plan to use the result of de-confusing PACS-100μm and 160μm and together with shorter wavelength SED priors, de-confusing SPIRE images, starting with SPIRE 250μm and progressively move up to de-confusing longer wavelength SPIRE images.

Chapter 3

What shapes the FIR SED of galaxies?

3.1 Introduction

Understanding what drives the variation in the far-infrared (FIR) spectral energy distributions (SEDs) of galaxies is a key goal if we wish to maximize the physical insight that can be gleaned from the wealth of data in the era of *Herschel* (Pilbratt et al., 2010b) and the Atacama Large Millimeter Array (ALMA). Unfortunately, interpreting FIR SEDs is difficult because spatially resolved data are not available for the vast majority of galaxies (although ALMA will help greatly in this regard). Moreover, there are various degeneracies (e.g., between the dust temperature distribution and the power-law index of the dust emissivity curve; see Kelly et al. 2012 and references

therein) that are difficult to break.

FIR SEDs are fit using a wide variety of methods (see Casey et al. 2014a for a recent review). Often, one or a sum of a few modified blackbody SEDs are used to fit FIR SEDs, but the physical information that can be gained from such models is limited (see, e.g., Hayward et al. 2012 and Smith et al. 2013 for detailed discussions). Another common approach is to use templates: by fitting the available photometry with an IR SED template, the IR luminosity can be estimated. Various empirically based, single-parameter templates are widely used (e.g., Chary & Elbaz, 2001b; Pope et al., 2008; Rieke et al., 2009a; Magdis et al., 2012b), although the limitations of this approach due to the luminosity dependence of the shape of FIR SEDs have long been recognised in the literature (e.g. Chapman et al., 2004).

Although empirically based FIR SED templates have many practical uses, physical models are necessary if one wishes to learn about the radiation field, dust properties of a galaxy and the geometry of dust with respect to the radiation sources. Because of the computational expense of radiative transfer and difficulty of constraining many free parameters with a limited number of FIR photometric data points, approaches to modeling FIR SEDs without doing radiative transfer calculations have been advocated (e.g., Desert et al., 1990; Devriendt et al., 1999; Dale et al., 2001; Dale & Helou, 2002a; Draine & Li, 2007; da Cunha et al., 2008; Somerville et al., 2012). Some authors (e.g., Dale et al., 2001; Dale & Helou, 2002a) model FIR SEDs by assuming that the mass distribution of dust that is exposed to radiation fields of different

intensities can be described by a truncated power law. Draine & Li (2007) expanded this model by adding a delta function to the intensity distribution (at the minimum intensity) to represent diffuse ISM dust (see also Draine et al. 2007a). Such models can provide good fits to observed SEDs. Similarly, other authors (e.g., Kovács et al., 2010; Magnelli et al., 2012) parameterize SEDs by assuming a power-law distribution of dust temperatures.

Radiative transfer calculations, either with simplified assumptions about the geometry of dust with respect to stars (Witt & Gordon, 1996b, 2000b; Silva et al., 1998; Efstathiou et al., 2000; Gordon et al., 2001b; Takagi et al., 2003; De Geyter et al., 2014) or active galactic nuclei (AGN; e.g., Fritz et al. 2006; Siebenmorgen & Krügel 2007; Stalevski et al. 2012), or more complicated geometries (Dopita et al., 2005; Popescu et al., 2011; De Looze et al., 2011, 2014; De Geyter et al., 2015), have been qualitatively successful in producing SEDs similar to those observed. It is also possible and (has become increasingly common) to 'forward-model' FIR SEDs by performing three-dimensional (3D) dust radiative transfer on the outputs of hydrodynamical simulations of galaxies in post-processing (e.g. Jonsson, 2006; Jonsson et al., 2006, 2010; Chakrabarti et al., 2007, 2008; Chakrabarti & Whitney, 2008; Narayanan et al., 2010b,a; Hayward et al., 2011a, 2012; Snyder et al., 2013; Lanz et al., 2014; Granato et al., 2015).

Because explicit radiative transfer calculations can best capture complicated source and dust geometries; directly treat dust absorption (including not only absorption of

primary radiation from stars and AGN but also dust self-absorption), scattering, and re-emission; and fully characterize the 3D distribution of dust temperature, which depend on both the local radiation field and the grain properties, they provide the best tool for studying how FIR SEDs depend on galaxy properties. By performing 3-D Monte Carlo radiative transfer calculations for idealized geometries (i.e., not outputs of hydrodynamical simulations), Misselt et al. (2001b) studied the dependence of the shape of the FIR SED on global parameters of the emitting regions. They found that higher dust mass leads to colder SEDs when the other parameters in their model are fixed. This is a simple consequence of thermal equilibrium. Moreover, a 'shell' (aka foreground screen) geometry results in a broader SEDs compared to a geometry in which stars and dust are mixed (which they term the 'dusty' geometry) because of differences in the temperature structures of the two models.

Performing radiative transfer on hydrodynamical simulations of galaxy formation has the benefit of including more realistic source and dust geometries than simpler approaches, such as that of Misselt et al. (2001b). This approach has been demonstrated (Jonsson et al., 2010) to yield SEDs that agree well with observed local samples of normal star forming galaxies from the Spitzer Infrared Nearby Galaxies Survey (SINGS; Kennicutt Jr et al., 2003b) and local luminous infrared (IR) galaxies (LIRGs) from the Great Observatories All-sky LIRG Survey (GOALS; Armus et al., 2009b). Moreover, Lanz et al. (2014) have shown that the SEDs of local interacting galaxies from the *Spitzer* Interacting Galaxies Survey (SIGS; Lanz et al., 2013; Brassington et al.,

2015) can be fit reasonably well with SEDs predicted in this manner; this is also the case for 24-μm-selected galaxies at $z \sim 0.3 - 2.8$ (Roebuck et al., in preparation). Unfortunately, performing 3D radiative transfer on hydrodynamical simulations is orders-of-magnitude more computationally expensive than less detailed approaches that assume smooth axisymmetric geometries (e.g., Silva et al., 1998): the former typically requires of order $10 - 10^3$ CPU-hours per galaxy, whereas the latter requires at most a few minutes. Thus, it is instructive to determine whether the high computational expense of performing 3D dust radiative transfer on hydrodynamical simulations of galaxies can be avoided, as it may be possible to characterize the variation among the simulated SEDs using only a few global parameters.

In this work, we investigate whether we can predict the FIR SEDs of simulated galaxies, which were calculated using 3D dust radiative transfer in previous works, using a simple, computationally inexpensive method. The method that we use to study these SEDs is principal component analysis (PCA). In our case, PCA yields FIR SED eigenvectors (principal components, hereafter PCs) such that linearly combining them with the mean SED of the sample can capture the variance in the simulated SEDs. The coefficients of each PC are different for each galaxy, and studying how the coefficients depend on global parameters, such as the star formation rate (SFR) or IR luminosity, can give physical intuition regarding what drives the dispersion in the FIR SEDs.

The simulated galaxy SEDs used in this work have been analyzed extensively

in previous works. These or similar simulations have been demonstrated to exhibit good agreement with the SEDs/colors of various classes of real galaxies, including local 'normal' galaxies (Jonsson et al., 2010) and (U)LIRGs (Younger et al., 2009b; Jonsson et al., 2010; Lanz et al., 2014), high-redshift dusty star-forming galaxies (Narayanan et al. 2010b,a; Hayward et al. 2011a, 2012; Roebuck et al., in prep.), obscured AGN (Snyder et al. 2013; Roebuck et al., in preparation), post-starburst galaxies (Snyder et al., 2011), and compact quiescent galaxies (Wuyts et al., 2010). Thus, although the simulations used herein naturally have some associated limitations (see Section 3.8.6), they have the advantage of being well-tested and in agreement with many observational constraints. Furthermore, to the best of our knowledge, they still represent the state of the art in terms of ultraviolet (UV)–millimeter (mm) SEDs generated from 3D hydrodynamical simulations of galaxies.

In addition to determining what physical insights about galaxies can be gained from their FIR SEDs, we hope to identify possibilities for improving how semi-analytic models (SAMs) of galaxy formation predict FIR SEDs. Some SAMs (e.g., Silva et al., 1998; Granato et al., 2000a) employ radiative transfer calculations that assume axisymmetric geometries or analytic models that are designed to capture the results of such calculations (e.g., González et al., 2011). Such calculations have been widely employed, but it is unclear how well their results agree with those of 3D radiative transfer calculations performed on hydrodynamical simulations of galaxies with more complex geometries. Other SAMs (e.g., Somerville et al., 2012) use empirically de-

rived templates that are a function of a single parameter, $L_{\rm IR}$, to predict FIR SEDs. However, such an approach is insufficient; for example, it cannot capture the redshift evolution of the effective dust temperature–IR luminosity relation (Casey et al. 2014a and references therein) by construction. Thus, we aim to determine one or more additional physical parameters, besides $L_{\rm IR}$, that can be used to predict the FIR SEDs of galaxies. Having determined what additional parameter(s) is necessary to predict the variation in IR SEDs, we can then generate a set of multi-parameter SED templates. By incorporating these templates in a SAM, we may be able to resolve the tension between the observed FIR and submillimeter number counts and those predicted by the SAM (Somerville et al., 2012; Niemi et al., 2012); this will be explored in a future work. These templates could be also used in semi-empirical models (e.g., Béthermin et al., 2012, 2013; Bernhard et al., 2014). Finally, these two-parameter templates will be useful for fitting observed SEDs to infer the total IR luminosity and predict fluxes at wavelengths for which data are not available.

The remainder of this paper is organized as follows: in Section 5.2, we describe the properties of the simulated galaxy SED dataset that we use and summarize the details of the hydrodynamical simulation and dust radiative transfer calculation methods. Section 3.3 summarizes the PCA technique and how we use the PCA results to predict the simulated galaxies' SEDs. In Section 3.4, we present the results of the PCA of the simulated galaxy SEDs. Section 3.5 demonstrates that the dust mass is a key parameter, in addition to the IR luminosity, that determines the SED shape, whereas

in Section 3.6, we show that incorporating the galaxy size does not improve our ability to predict the FIR SEDs. In Section 3.7, we present a two-parameter family of SED templates that depend on the IR luminosity and dust mass. In Section 3.8, we discuss some observational support for the importance of dust mass in determining the SED shape; speculate regarding the unimportance of galaxy size, the origin of catastrophic failures to predict the SEDs, and the possible implications of using the proposed two-parameter templates in SAMs; and highlight some limitations of our work. Section 3.9 lists our primary conclusions.

3.2 Simulated galaxy SED dataset

In this work, we analyze two sets of FIR SEDs of simulated isolated and merging disk galaxies that were presented in previous works. We will first summarize the properties of the two datasets and then briefly discuss the simulation methodology. The first SED dataset was originally presented in Lanz et al. (2014) and Hayward et al. (2014a). The four progenitor galaxies span a stellar (baryonic) mass range of $6 \times 10^8 - 4 \times 10^{10}$ $M_\odot$ ($10^9 - 5 \times 10^{10}$ $M_\odot$), and their properties were selected to be representative of typical star-forming galaxies in the $z \sim 0$ universe (see Cox et al. 2008 for details). Each of the four progenitors was simulated in isolation, and binary mergers of all possible combinations of progenitors were simulated for a single representative orbit (i.e., the results for other 'non-special' orbits are similar; the

results for perfectly co-planar and other rare special configurations can sometimes differ significantly; e.g., Cox et al. 2008), thereby yielding 10 merger simulations. The total dataset contains $\sim 12,000$ SEDs. We refer to this dataset as the $z \sim 0$ dataset.

The second set of SEDs of simulated isolated disk and merging galaxies was presented in Hayward et al. (2011a, 2012, 2013b). For this dataset, the structural properties of the progenitor (bulgeless) disk galaxies were scaled to $z \sim 3$ following the method of Robertson et al. (2006), and the initial gas fractions of the disks, 0.6-0.8, are significantly greater than those of the $z \sim 0$ simulations.[1] Because the original purpose of these simulations was to model high-redshift submillimeter galaxies (SMGs), the progenitor disks span a relatively narrow baryonic mass range of $\sim 1{-}4{\times}10^{11}$ $M_{\odot}$, but a variety of merger orbits and mass ratios are included (see Hayward et al. 2012 for details). This dataset contains 37 hydrodynamical simulations, from which ~ 6500 SEDs were calculated. We refer to this dataset as the $z \sim 3$ dataset.

The SEDs contained in the two datasets were generated by performing dust radiative transfer in post-processing on the outputs of 3-D hydrodynamical simulations. The full methodology is described in the aforementioned works and references therein, so we will only summarize it here. First, idealized isolated (i.e., non-cosmological) galaxy models were created following the method described in Springel et al. (2005). Each initial disk galaxy is composed of a dark matter halo, stellar and gaseous disks,

[1]Such large gas fractions were used to ensure that the gas fraction at the time of coalescence was consistent with observational constraints for $z \sim 2$ galaxies. For all snapshots considered in this work, the gas fractions are < 0.5. See Hayward et al. (2013b) for more details.

and a supermassive black hole (SMBH); for the $z \sim 0$ simulations only, a stellar bulge is also included. Then, the isolated galaxies and binary mergers of these galaxies were simulated using a heavily modified version of the GADGET2 N-body/smoothed-particle hydrodynamics (SPH) code (Springel, 2005).[2] The simulations include the effects of gravity, hydrodynamical interactions, and radiative heating and cooling. Star formation and stellar feedback are incorporated via the two-phase sub-resolution interstellar medium (ISM) model of Springel & Hernquist (2003), and BH accretion and AGN feedback are treated following Springel et al. (2005). Each gas particle is enriched with metals according to its associated SFR, assuming a yield of 0.02.

Every 10 Myr, 'snapshots' of the physical state of the simulations were saved. Then, to calculate UV–mm SEDs, 3-D dust radiative transfer was performed in post-processing on a subset of the snapshots using the code SUNRISE (Jonsson, 2006; Jonsson et al., 2010). For a given snapshot, the SUNRISE calculation proceeds as follows: the stellar and BH particles in the GADGET2 simulation, which are the sources of radiation, are assigned source SEDs according to their properties (age and metallicity for the star particles and luminosity for the BH particles). The metal distribution from the simulation is projected onto an octree grid for the purpose of calculating the dust optical depths (assuming a dust-to-metal density ratio of 0.4; e.g., Dwek 1998b; James et al. 2002; Sparre et al. 2014). The Milky Way $R_V = 3.1$

[2]The traditional density–entropy formulation of SPH was used. However, we note that the results of idealized non-cosmological galaxy simulations such as these are relatively insensitive to the numerical method and thus do not consider the use of traditional SPH to be a significant limitation.

dust model of Draine & Li (2007) was used.

The most significant uncertainty (of which we are aware) in these calculations is the sub-resolution structure of the ISM. Specifically, the simulations do not resolve the ISM structure on scales of less than a few hundred parsecs, but observations clearly indicate that the ISM has substantial structure on smaller scales. We can crudely investigate this uncertainty through the use of two alternate treatments for the sub-resolution ISM.[3] In the first treatment (referred to as 'multiphase on' or 'default ISM' in previous works), it is assumed that the cold clouds implicit in the Springel & Hernquist (2003) model have negligible volume filling factors. Thus, for the purpose of the radiative transfer calculations, this dust is ignored. To account for the obscuration of young stars from their birth clouds, a sub-resolution model for HII and photodissociation regions (Groves et al., 2008) is used. In the second treatment ('multiphase off' or 'alternate ISM'), the entire dust mass (i.e., dust in both the implicit diffuse phase and cold clouds) is considered in the radiative transfer calculations. In this work, we use the 'multiphase off' model to ensure that all of the dust emission is calculated self-consistently (i.e., there is no component from the sub-resolution HII and photodissociation region model). However, we have checked that our conclusions are qualitatively unchanged if the 'multiphase on' model is used.

After the source and dust properties are specified, radiation transfer is performed using the Monte Carlo method to calculate the effects of dust absorption, scatter-

[3]This issue has been discussed extensively in previous works (e.g., Hayward et al., 2011a; Snyder et al., 2013; Lanz et al., 2014; Hayward & Smith, 2015), and we refer the interested reader to those papers for additional details.

ing, and re-emission. Importantly, dust self-absorption is treated using an iterative procedure in which the transfer of IR radiation and dust temperature calculation are repeated until the luminosity absorbed in each cell is sufficiently converged. For each snapshot, this process yields spatially resolved UV–mm SEDs of the simulated galaxy/merger viewed from 7 viewing angles.

We only analyze the SEDs of galaxies that are either isolated systems or mergers that are experiencing coalescence (defined by a black hole separation of <1 kpc) or are post-coalescence. The reason for this choice is that we only want to study systems that can be considered a single galaxy. Using this black hole separation criterion excludes early stage mergers, which would often be considered separate systems in low-redshift observations (although they would be unresolved in the FIR at high redshift when observed with single-dish FIR or submillimeter telescopes). Moreover, when the system consists of widely separated galaxies, the radiative transfer within individual galaxies is decoupled (i.e., the radiation within one galaxy does not have a significant effect on the dust in the other galaxy when the two galaxies are separated by many kiloparsecs). Using a less conservative criterion, such as 5 kpc, does not qualitatively affect our results.

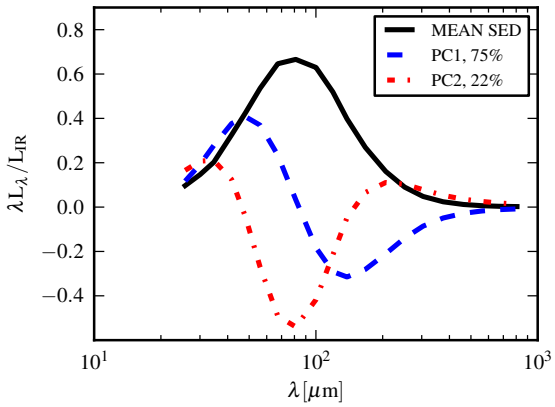

Figure 3.1: The black solid line corresponds to the mean FIR SED of our full sample; it has been normalized by dividing by $L_{\rm IR}$. The first (PC1; blue dashed line) and second (PC2; green dash-dotted line) PCs are also shown. These PCs are added to the mean with a unique coefficient for each galaxy to reconstruct the individual FIR SEDs. The fraction of the variance in the data that is explained by each PC is indicated as a percentage in the legend. Together, the top 2 PCs can explain 97% of the total variance of the data in the full SED sample, which includes both low- and high-redshift simulated galaxies.

3.3 Predicting the SEDs based on PCA

Given a sample of FIR SEDs, PCA finds the mean SED of the entire sample ($\langle \lambda L_\lambda \rangle$) and based on the mean SED, finds the PCs that encapsulate most of the variance of the entire sample. PCs are eigenvectors that are orthogonal to each other. The PCs are not guaranteed to have a physical interpretation; rather, they are a tool to reduce the dimensionality of the problem. The PCs are ranked in terms of how much of the variance is explained by each PC.

Because we are interested in studying the shape of the SEDs, we normalize the FIR SEDs by dividing them by the IR luminosity.[4] The units of the data on which

[4]We define $L_{\rm IR}$ as the integral of the SED over the wavelength range of 8-1000 μm .

the PCA is performed do not affect the results, and we have chosen to work in dimensionless units of $\lambda L_\lambda / L_{\rm IR}$.

The SED belonging to a given galaxy (j) in the sample can be reconstructed as a linear combination of principal components:

$$\lambda L_{\lambda,j} = \langle \lambda L_\lambda \rangle + \sum_{i=1}^{N} C_{i,j} \times PC_i, \tag{3.1}$$

where N is the number of PCs used, PC_i is the ith PC, and $C_{i,j}$ is the coefficient of the ith PC for the jth galaxy.

Having identified the most important PCs, we then examine how the coefficients of the PCs correlate with various global physical parameters of the galaxies. Our goal is to be able to predict the PC coefficients, and thus the FIR SED, of a galaxy based on a small number of galaxy properties, such as the SFR. To predict the PC coefficients, we use functions of the following form:

$$C'_{i,j} = \alpha_i + \sum_{k=1}^{M} \beta_{i,k} \log P_{i,j,k}, \tag{3.2}$$

where $C'_{i,j}$ is the predicted value of the ith coefficient for galaxy j, α_i is the fit intercept for the ith PC coefficient, $\beta_{i,k}$ is the fit coefficient for the ith PC coefficient and kth parameter, and $P_{i,j,k}$ is galaxy j's value for the kth physical property used to predict the ith PC coefficient; example properties include the SFR and dust mass. As we will discuss below, we found that 2 PCs were sufficient to explain 97% of the variance.

Thus, we used $N = 2$. To predict the PC coefficients, we tried relations with both a single physical property ($M = 1$) and a pair of physical properties ($M = 2$).

Given predicted values for a galaxy's PC coefficients determined using Equation (3.2), we predict its SED as follows:

$$\lambda L'_{\lambda,j} = \langle \lambda L_\lambda \rangle + \sum_{i=1}^{N} C'_{i,j} \times PC_i. \tag{3.3}$$

To quantify how well an SED can be predicted, we use the following quantity:

$$\chi^2_r = \frac{1}{df} \sum_{i=1}^{P} \frac{(L_{\lambda_i} - L'_{\lambda_i})^2}{\sigma^2_{\lambda_i}}, \tag{3.4}$$

where where L_{λ_i} and L'_{λ_i} denote the true and predicted luminosity density values at wavelength λ_i, σ_{λ_i} is the uncertainty at wavelength λ_i, $P = 20$ is the total number of wavelength bins in the FIR, and $df = P - M - 1$ is the number of degrees of freedom. Because our data are noise-free, for the purposes of calculating the χ^2_r value, we have arbitrarily assumed a signal-to-noise ratio of 5 in each band (i.e., $\sigma_{\lambda_i} = 0.2 L_{\lambda_i}$).[5]

[5]We have used the form of the reduced chi-squared statistic, but we avoid using this terminology and do not mean to imply that the statistic should follow a chi-squared distribution (because the uncertainties are arbitrary). However, we opted to use the χ^2_r notation so that the reader can easily recall the definition of the quantity. Thus, the χ^2_r values are useful in a relative sense (i.e., to determine which SEDs are predicted better than others), but the absolute values are not very meaningful.

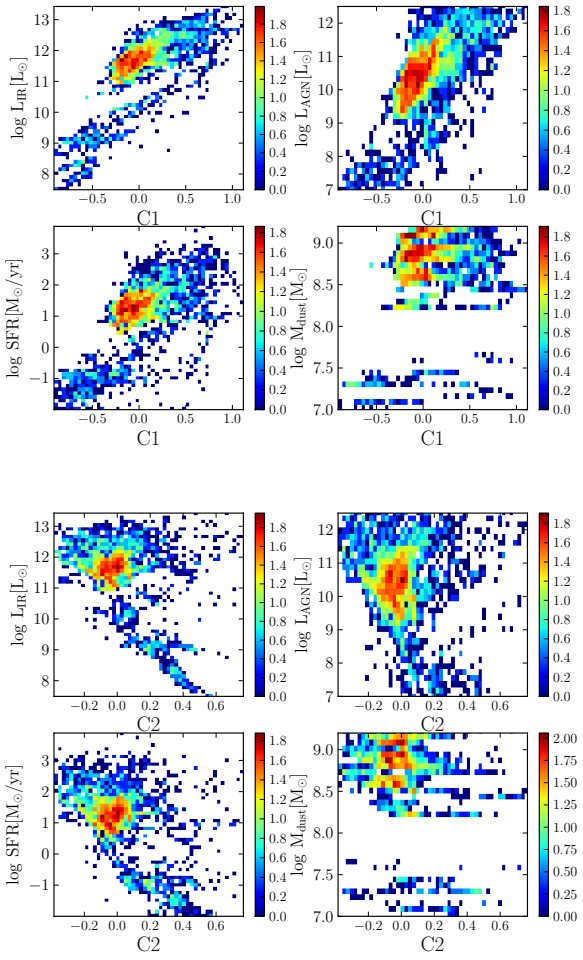

Figure 3.2: The *top* set of four figures shows how the coefficient of the first PC depends on four global physical parameters of the galaxies in the entire sample: IR luminosity (*upper left*), AGN luminosity (*upper right*), SFR (*lower left*), and dust mass (*lower right*). The *bottom* set of four figures shows the same plots for C2. In each panel, the parameter value is shown on the y-axis, and the x-axis corresponds to the value of the coefficient. The color of each bin corresponds to the logarithm of the number of points in the bin, as specified by the colorbars. C1 is correlated with IR luminosity, SFR and AGN luminosity, although there is a large scatter. This result indicates that as the IR luminosity, SFR or AGN luminosity is increased, the SED peak shifts toward shorter wavelengths. C2 is anti-correlated with all of the four physical parameters, although the correlations are weaker (see the text for details). This result indicates that there is a weak tendency for higher-luminosity or/and higher-dust mass galaxies to have narrower FIR SEDs.

3.4 PCA results

We performed PCA on the FIR ($\lambda > 25\ \mu m$) SEDs from our entire sample, which includes both low- and high-redshift simulated galaxies. Figure 3.1 shows the mean SED and first two PCs of our sample. The percentage of the variance in the SEDs that can be explained by each PC is indicated in the figure. Each PC is multiplied by a coefficient (which is unique for each galaxy) and added to the mean SED of the sample to reconstruct the FIR SED of a particular galaxy. The coefficient can be negative or positive. From Figure 3.1, it is clear that adding the first PC (PC1) with a positive coefficient to the mean FIR SED tends to make the SED warmer with respect to the mean SED (i.e., the wavelength at which the FIR emission peaks shifts to shorter wavelengths); if it is added with a negative coefficient, the resulting SED is cooler than the mean. Thus, the coefficient of PC1 can be considered a proxy for the effective dust temperature of the SED. In contrast, the second PC (PC2) affects the width of the SED: if it is added with a positive coefficient to the mean FIR SED, it tends to broaden the SED by increasing the power in the wings and removing power from the center. Conversely, it makes the FIR SED peak narrower if added with a negative coefficient.

The coefficients of the PCs for a galaxy determine how its FIR SED differs from the mean SED. Figure 3.2 shows how the coefficients of PC1 and PC2 (we refer to them as C1 and C2, respectively) for each galaxy in the entire sample depend on four different global physical parameters (SFR, AGN luminosity, IR luminosity

and dust mass) that we expect to affect the FIR SEDs. We focus on these specific parameters because they are simple global parameters that are clearly important for the radiative transfer, and they are typically available in SAMs. The first two characterize the radiation that can potentially heat the dust. The IR luminosity tells us how much radiation is absorbed by dust; of course, this quantity depends on both the bolometric luminosity of the stars and AGN and what fraction of the intrinsic luminosity is absorbed.[6] The dust mass characterizes the radiation sinks. As detailed below, we have also explored using other individual or pairs of parameters to predict the coefficient values, but we do not show them in this plot because we do not focus on them in the bulk of the analysis below.

Figure 3.2 indicates that C1 correlates with IR luminosity (with a Pearson correlation coefficient of $r = 0.71$), SFR ($r = 0.60$) and AGN luminosity ($r = 0.73$), although there is a large scatter. This result indicates that as the IR luminosity, SFR or AGN luminosity is increased, the SED peak shifts toward shorter wavelengths, which is to be expected because of the known correlation between effective dust temperature and IR luminosity. The correlations between C2 and the four properties shown in Figure 3.2 are all weak negative correlations (all have $-0.5 < r < 0$). This result indicates

[6]Throughout this work, we use $L_{\rm IR}$ calculated by integrating the SEDs over the wavelength range of $8 - 1000$ μm . When dust self-absorption is negligible, this quantity is independent of viewing angle and identical to the luminosity absorbed by dust. However, when dust self-absorption is non-negligible, $L_{\rm IR}$ can depend on viewing angle, whereas the luminosity absorbed by dust is an intrinsic property of the simulated galaxy that does not depend on viewing angle (see Hayward et al. 2011a for more details). We opt to use $L_{\rm IR}$ rather than the absorbed luminosity because (1) the former can be inferred from observations without recourse to radiative transfer modeling, (2) the average of $L_{\rm IR}$ taken over a sufficient number of viewing angles must equal the absorbed luminosity, and (3) dust self-absorption does not lead to significant variation in $L_{\rm IR}$ with viewing angle for the bulk of the simulated galaxies.

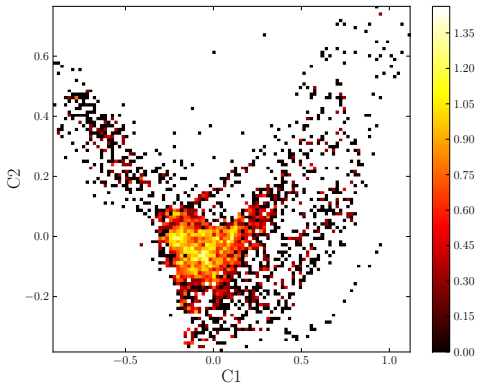

Figure 3.3: Biplot of C1 versus C2. The color bar indicates the logarithm of the number of SEDs in the bin. Recall that higher values of C1 correspond to hotter SEDs, and higher values of C2 correspond to broader SEDs. The white space corresponds to no data in this plot. There appears to be a negative correlation between C1 and C2 at values of C1 less than -0.3. However, the density of our data points are more than 10 times higher in the dense (yellow) region where we see no correlation between C1 and C2. Therefore, we tend to not drive strong conclusions based on the possible correlation between C1 and C2 when C1<0. Regions outside -0.3<C1 <0.4 and -0.3<C2<0.1 are sparsely populated and we can not reach a firm conclusion by studying those regions.

that there is a weak tendency for higher-luminosity or/and higher-dust mass galaxies to have narrower FIR SEDs.

Other than correlations between the PCs and the global parameters, it is also interesting to consider whether there is a correlation between the PC coefficients. Although PC1 and PC2 are orthogonal by construction, their coefficients may still be correlated. In our case, a correlation between C1 and C2 would indicate a relation between the effective temperature of the SED and its broadness. To see if there is such correlation, we plot C1 versus C2 for all the SEDs in our sample in Figure 3.3. We find that C1 and C2 are uncorrelated.

Because the scatter in the correlations between the coefficients and global galaxy parameters shown in Figure 3.2 is large, it is worth considering whether we can better predict the coefficients using two parameters simultaneously. In particular, thermal equilibrium considerations suggest that combining dust mass and a luminosity-related parameter (e.g. IR luminosity or SFR) could be promising.[7] Thus, in Figure 3.4, we show the results of predicting C1 (top) and C2 (bottom) in four different manners: 1) using $\log L_{\rm IR}$ (e.g., C1 $= A \log L_{\rm IR} + B$), 2) using log SFR (e.g., C1 $= A \log$ SFR $+B$), 3) using $L_{\rm IR}$ and $M_{\rm dust}$ (e.g., C1 $= A \log L_{\rm IR} + B \log M_{\rm dust} + C$) and 4) using log SFR together with $\log M_{\rm dust}$ (e.g., C1 $= A \log$ SFR $+B \log M_{\rm dust} + C$). [8] It is clear that

[7] We have not used the AGN luminosity as a predictor despite the correlation evident in Figure 3.2 for the following reason: for most of the simulated galaxies, the AGN contributes less than 10 percent of the bolometric luminosity, and the FIR luminosity is not AGN-dominated (a detailed analysis of the contribution of AGN to FIR emission will be presented in Hayward et al., in prep.) Consequently, the correlation between the AGN luminosity and C1 does not indicate causation; rather, it arises because in the simulations that we analyze, the black hole accretion rate and SFR are correlated.

[8] We have explored using various other combinations of parameters and found that these combi-

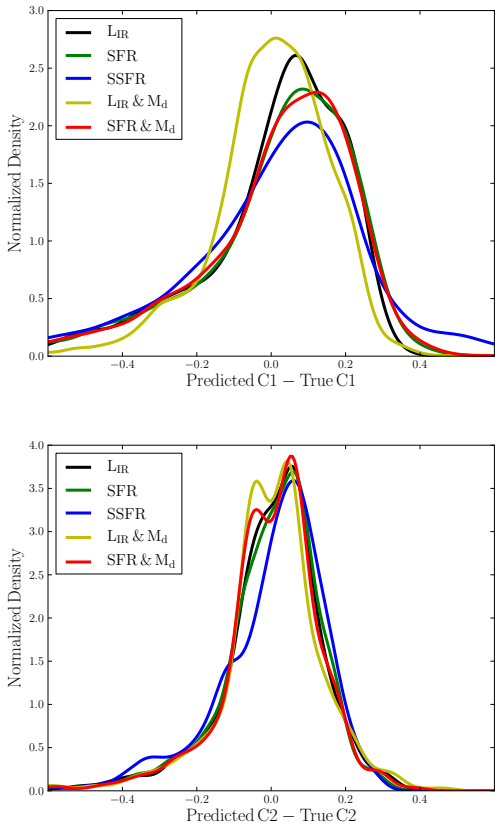

Figure 3.4: The *top* panel shows the difference between the predicted and true values of C1 (the coefficient of the first PC). C1 is estimated using five different estimators that depend on either one or two physical parameters; see the figure legend for the parameters used. In all cases, the logarithm of the parameter is used. Using both IR luminosity and dust mass helps reduce the bias in the predicted C1 values compared with the other estimators. In the *bottom* panel, the same is shown for C2. Again, the combination of IR luminosity and dust mass is superior to the others, although the difference in predictive power is less than for C1.

the combination of $\log L_{\rm IR}$ and $\log M_{\rm dust}$ results is best able to predict C1, and this combination is superior to $\log L_{\rm IR}$ alone (i.e., incorporating the dust mass reduces the error in the prediction). For C2, the combination of $\log L_{\rm IR}$ and $\log M_{\rm dust}$ is again superior to the others, but the differences in predictive power are less significant than for C1. Our best-fitting relations for C1 and C2 are the following:

$$\mathrm{C1} = 0.52 \log\left(\frac{L_{\rm IR}}{L_\odot}\right) - 0.47 \log\left(\frac{M_{\rm dust}}{\mathrm{M}_\odot}\right) - 1.88 \quad (3.5)$$

$$\mathrm{C2} = -0.014 \log\left(\frac{L_{\rm IR}}{L_\odot}\right) - 0.10 \log\left(\frac{M_{\rm dust}}{\mathrm{M}_\odot}\right) + 1.05. \quad (3.6)$$

We note that the coefficients for $\log L_{\rm IR}$ and $\log M_{\rm dust}$ in Equation (3.5) have similar magnitudes but opposite signs. This suggests that the value of C1 depends on the ratio $L_{\rm IR}/M_{\rm dust}$. We shall discuss this in detail in Section 3.8.1. C2 depends only weakly on dust mass and is effectively independent of $L_{\rm IR}$. Thus, there is a mild tendency for sources with higher dust masses to have narrower SED peaks. Because of the weakness of the dependence, we will not interpret it further.

We now investigate how well we can predict the SEDs by predicting the PC coefficients using Equations (3.5) and (3.6) and using Equation (3.3) to predict the SED. Figure 3.5 compares the predicted and true SEDs for 9 randomly chosen SEDs from our entire sample. The true SED is shown in blue. The red (green) line is the

nations had the best predictive power.

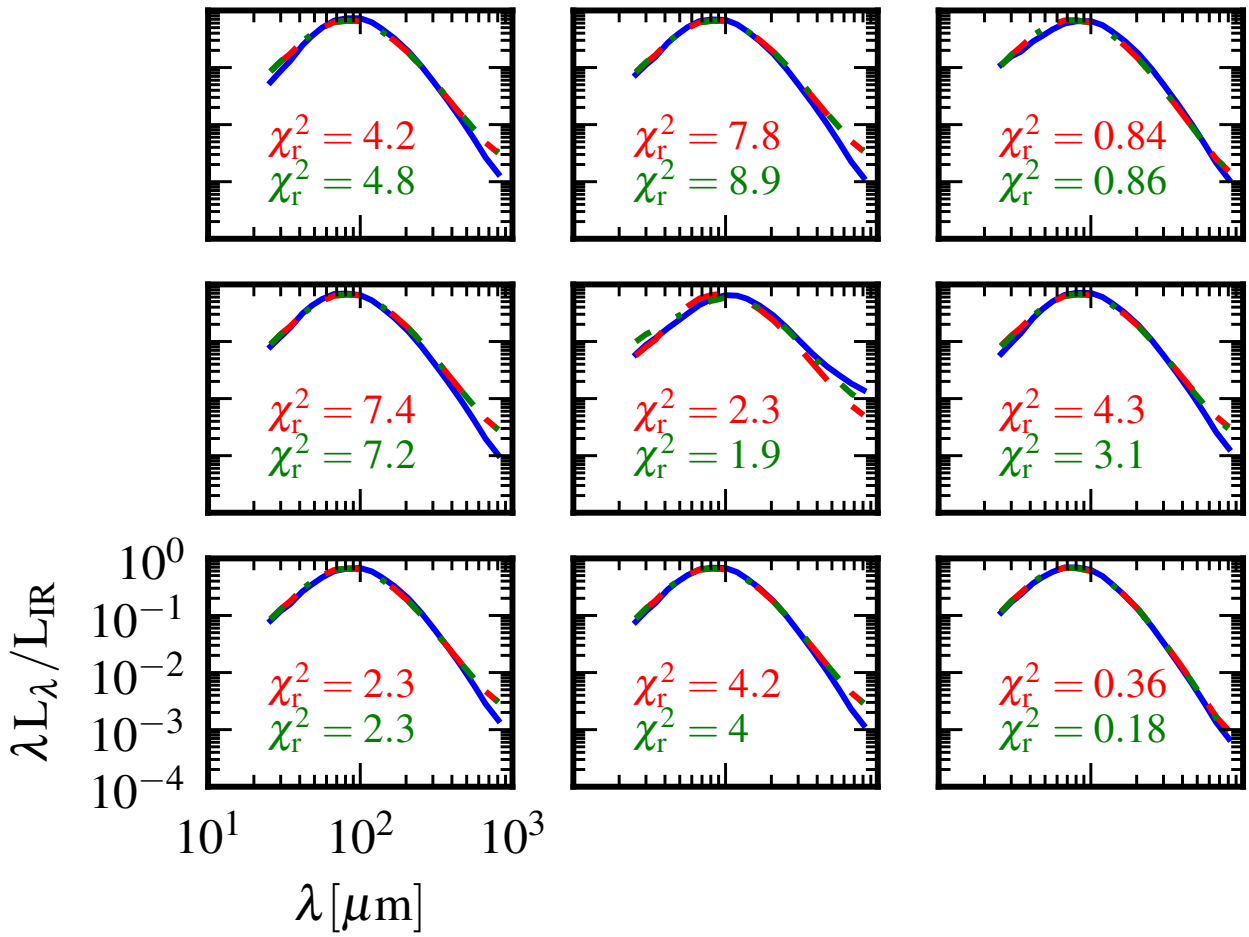

Figure 3.5: Comparisons of the predicted and true SEDs for 9 SEDs randomly chosen from the entire sample. The blue line is the actual SED. The red (green) line is the predicted SED obtained by adding the first PC (first and second PC) to the mean SED with the coefficient value(s) predicted using $L_{\rm IR}$ and $M_{\rm dust}$. The numbers indicate the χ^2_r value (Equation 3.4); a signal-to-noise ratio of 5 in each band was arbitrarily assumed when computing the χ^2_r. Note that using the second PC leads to a better prediction in only some of the cases.

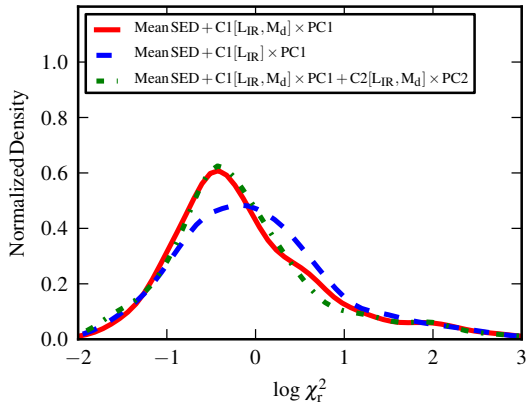

Figure 3.6: This figure shows how well the SEDs of the simulated galaxies can be predicted, as characterized by the χ_r^2 values, using the PCs. The red line corresponds to when only PC1 is used; its coefficient is predicted using $L_{\rm IR}$ and $M_{\rm dust}$. The dashed blue line shows the result when only PC1 is used and its coefficient is predicted using only $L_{\rm IR}$. The dot-dashed green line shows the result when both PC1 and PC2 are used; their coefficients are predicted using both $L_{\rm IR}$ and $M_{\rm dust}$. When C1 is predicted using both $L_{\rm IR}$ and $M_{\rm dust}$, the χ_r^2 distribution shifts significantly to the left compared with when only $L_{\rm IR}$ is used; the median χ_r^2 value is 0.56 (0.82) when both $L_{\rm IR}$ and $M_{\rm dust}$ are (only $L_{\rm IR}$ is) used to predict C1. Thus, incorporating the dust mass yields considerably better SED predictions. The similarity of the red solid and green dot-dashed lines indicates that using PC2 does not lead to significantly better χ_r^2 values, and the median value (0.54) is only slightly less than when only PC1 is used (assuming that C1 is predicted using both $L_{\rm IR}$ and $M_{\rm dust}$).

predicted SED obtained by adding the first PC (first and second PC) to the mean SED with the coefficient value(s) predicted based on the galaxy's $L_{\rm IR}$ and $M_{\rm dust}$ values (using Equations 3.5 and 3.6). The red (green) number in each panel indicates the χ^2_r value (Equation 3.4) obtained when only PC1 (both PC1 and PC2) is (are) used to predict the SED. From these examples, we see that the FIR SEDs are generally predicted very well near their peaks. Generally, when $\chi^2_r > 1$, the reason is that the predicted and actual FIR SEDs differ at long wavelengths. Finally, using PC2 improves the prediction (in particular, at long wavelengths) in only some cases, and it can actually make the prediction worse; this is true even if we use the true values of C1 and C2 rather than those predicted using Equations (3.5) and (3.6). We shall discuss these points in more detail below.

Figure 3.6 shows the distribution of χ^2_r (Equation 3.4) for all SEDs in the full sample when the SEDs are predicted in this manner (the green line). We also show the χ^2_r distributions obtained when using only PC1 and predicting its coefficient, C1, using either $L_{\rm IR}$ alone (the blue dashed line) or $L_{\rm IR}$ and $M_{\rm dust}$ (the red solid line). A comparison of the solid red and blue dashed lines indicates that incorporating the dust mass results in significantly more accurate SED predictions compared with using $L_{\rm IR}$ alone. The median χ^2_r value is 0.56 (0.82) when both $L_{\rm IR}$ and $M_{\rm dust}$ are (only $L_{\rm IR}$ is) used to predict C1. This result indicates that the SEDs should be parameterized in terms of $L_{\rm IR}$ and $M_{\rm dust}$, not just $L_{\rm IR}$; we shall discuss this in detail below. The similarity of the green dashed and solid red lines indicates that using PC2 in addition

to PC1 does not yield significantly better SED predictions in terms of χ_r^2; in this case, the median χ_r^2 is 0.54, only 0.02 less than when PC1 alone is used (and both $L_{\rm IR}$ and $M_{\rm dust}$ are used to predict C1). This is consistent with our observation from Figure 3.5 that adding PC2 sometimes leads to a better prediction at long wavelengths but sometimes causes the prediction to be worse.

We consider the SED predictions with $\chi_r^2 >> 10$ to have failed catastrophically relative to those with $\chi_r^2 \sim 1$. By exploring the locations of these galaxies in different parameter spaces, we determined that the catastrophic failures tend to have a high AGN contribution to the bolometric luminosity or/and $L_{\rm IR} > 10^{12.5} L_{\odot}$, as indicated by Figure 3.7. This figure shows each galaxy in the plane of $L_{\rm IR}$ and $L_{\rm AGN}$. The colors of the points indicate the χ_r^2 value of the predicted SED. The top panel shows the results for the prediction based on only PC1, whereas the bottom panel shows the results for the prediction based on using both PC1 and PC2. Thus, the red circles represent galaxies for which the SED prediction fails catastrophically. It is clear that in both cases, the galaxies for which the SEDs are predicted least well tend to be galaxies that have high AGN luminosities given their $L_{\rm IR}$ values (i.e., high AGN luminosity fractions) or/and have $L_{\rm IR} > 10^{12.5} L_{\odot}$. We analyzed the galaxies with high AGN fractions separately, but we were unable to determine global parameters that we could use to predict their SEDs well. We speculate regarding the reasons for our inability to predict the FIR SEDs of such galaxies in Section 3.8.4. We retain the high-AGN galaxies in our subsequent analysis, but the results are not significantly

changed if we exclude them because only a small fraction of the simulated galaxies have $L_{\rm AGN} > 0.1$.

3.5 Impact of dust mass on the SEDs

FIR SEDs are often parameterized using templates that depend on the IR luminosity alone (e.g., Chary & Elbaz, 2001b; Rieke et al., 2009a; Lee et al., 2013; Symeonidis et al., 2013). At fixed redshift, the effective dust temperature is observed to increase (i.e., the peak of the FIR SED shifts to shorter wavelengths) with increasing $L_{\rm IR}$ (Casey et al., 2014a, and references therein). As discussed above, Figure 3.4 indicates that using both the IR luminosity and dust mass increases our ability to predict the C1 coefficients for galaxies compared with using the IR luminosity alone as a predictor. Because we know that C1 basically makes an SED cooler or warmer with respect to the mean SED (higher C1 values tend to make the SEDs hotter), it is instructive to examine how C1 behaves on the $L_{\rm IR}$ and $M_{\rm dust}$ plane. This is shown in Figure 3.8. One can see that at fixed $L_{\rm IR}$, higher values of $M_{\rm dust}$ correspond to lower values of C1, i.e., cooler SEDs. At fixed $M_{\rm dust}$, higher values of $L_{\rm IR}$ lead to higher values of C1, i.e., hotter SEDs.

To more explicitly demonstrate the effect of the dust mass on the SEDs, we have re-run a subset of the dust radiative transfer calculations with artificially lower and higher dust masses by changing the default dust-to-metal density ratio of 0.4 to 0.2

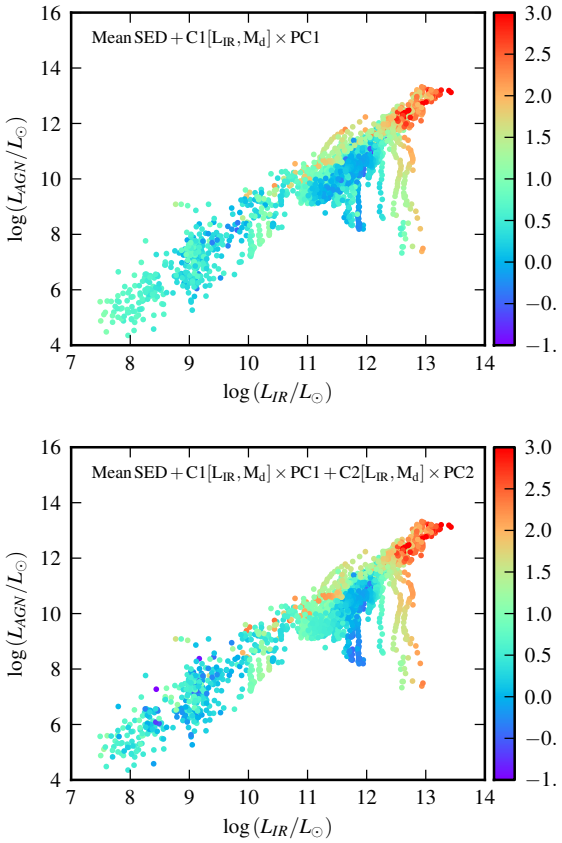

Figure 3.7: Shows the $\log \chi_r^2$ values for the predicted SEDs. In the *top* panel, the SEDs are predicted based on using only the first PC component, with its coefficient predicted using both IR luminosity and dust mass. In the *bottom* panel, the SEDs are predicted based on using both PC1 and PC2; for both PCs, the coefficients are predicted using $L_{\rm IR}$ and dust mass, but the relations used differ (see Equations 3.5 and 3.6). The colors of the circles indicate the value of the logarithm of χ_r^2. The galaxies for which the SEDs are predicted least well tend to be galaxies that have high AGN luminosities given their $L_{\rm IR}$ values or/and have $L_{\rm IR} > 10^{12.5} L_\odot$.

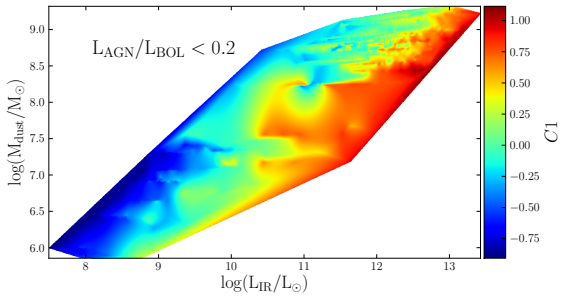

Figure 3.8: Shows the value of the C1 coefficient (see the colorbar) as a function of $L_{\rm IR}$(on the y-axis) and $M_{\rm dust}$ (on the x-axis). The interpolation between data points is performed using the nearest-neighbor method, which can result in some artifacts, but the trend that we see is robust. At fixed $L_{\rm IR}$, higher $M_{\rm dust}$ results in lower C1 values (i.e., lower effective dust temperature). At fixed $M_{\rm dust}$, higher $L_{\rm IR}$ results in higher C1 values (i.e., higher effective dust temperature).

and 0.8, respectively. Consequently, the relative distribution of the dust remains the same, but the overall normalization and thus total dust masses are half or twice those of the standard run. Representative results for two snapshots are presented in Figure 3.9; each panel shows how the FIR SED for a single time and viewing angle varies as the dust-to-metal density ratio is varied. The legends specify the assumed dust-to-metal ratio and values of $L_{\rm IR}$ and $M_{\rm dust}$ for each of the SEDs.

The results qualitatively agree with our expectations based on the above analysis. The top panel corresponds to the pre-coalescence phase of the most-massive major merger simulation from the $z = 0$ dataset. As the dust-to-metal ratio is increased, $L_{\rm IR}$ increases, and the peak of the SED shifts slightly to longer wavelengths (i.e., the SED becomes colder). In this case, a substantial fraction of the luminosity is not absorbed

when the dust-to-metal ratio is 0.2. Consequently, increasing the dust-to-metal ratio leads to higher optical depths and thus a larger fraction of light being absorbed and re-emitted in the IR.

The SEDs shown in the bottom panel correspond to the M3M3e merger simulation, the most-massive equal-mass merger simulation of $z \sim 0$ progenitors presented in Lanz et al. (2014), near the peak of the starburst induced at final coalescence. Because the luminosity is dominated by a central dust-enshrouded starburst, the simulated galaxy is already opaque to effectively all of the radiation when the dust-to-metal ratio is 0.2. Consequently, $L_{\rm IR}$ does not increase as the dust-to-metal ratio (and thus dust mass) is increased. Instead, it actually decreases by 0.1 dex; this occurs because we are considering the $L_{\rm IR}$ associated with a single viewing angle. When there is a non-negligible optical depth in the FIR, as can be the case for (U)LIRGs (see the discussion in Hayward et al. 2012), $L_{\rm IR}$ can depend on the viewing angle. The increased viewing-angle dependence as the dust-to-metal ratio is increased explains the aforementioned decrease because as the dust-to-metal ratio is increased, more of the short-wavelength IR emission is removed from this particular line of sight. The absorbed luminosity, which is independent of viewing angle, is effectively identical in this case for all dust-to-metal ratios.

Because the $L_{\rm IR}$ values are almost identical for the three SEDs shown in the bottom panel, they provide a clean test of how the SED varies with dust mass for fixed IR luminosity. We see that as expected based on the trend shown in Figure 3.8,

the FIR SED systematically shifts to longer wavelengths as the dust-to-metal ratio, and thus total dust mass, is increased; all other properties of the galaxy are kept fixed.

The reason why at fixed dust mass, increasing the IR luminosity increases the temperature of the SED is that there are more photons available to heat the same amount of dust; consequently, thermal equilibrium dictates that the dust temperature must increase. The reason why at fixed IR luminosity, increasing the dust mass tends to make the SED cooler is that the luminosity is distributed over a greater mass of dust (because of dust self-absorption). Thus, thermal equilibrium implies that the dust temperature will decrease. For an isothermal modified blackbody, the temperature scales as $T \propto (L_{\rm IR}/M_{\rm dust})^{1/(4+\beta)}$, where β is the power-law index of the dust opacity curve in the FIR (e.g. Hayward et al., 2011a; Lanz et al., 2014). Although the simulated SEDs are not quantitatively well-described by this simple model (Hayward et al., 2011a, 2012; Lanz et al., 2014), it provides physical motivation for the claim that the effective dust temperature increases (decreases) when $L_{\rm IR}$ ($M_{\rm dust}$) is increased and $M_{\rm dust}$ ($L_{\rm IR}$) is kept fixed.[9] Put another way, the mean intensity 'seen' by a dust grain is proportional to $L_{\rm IR}/M_{\rm dust}$ (see Draine & Li 2007 and Draine et al. 2007a for detailed discussions). Thus, as $L_{\rm IR}$ is increased or $M_{\rm dust}$ is decreased, the mean intensity of light absorbed by the dust and thus typical grain temperature increases,

[9]For observational values of $L_{\rm IR}$ and $M_{\rm dust}$ inferred from fitting galaxy SEDs with an isothermal modified blackbody, this relation is obeyed by construction. However, this is not the case for the simulations, in which the SED shape, and thus effective dust temperature, can in principle depend not only on the total luminosity heating the dust and the dust mass but also other factors, including the spatial distribution of the dust and sources and the dust composition.

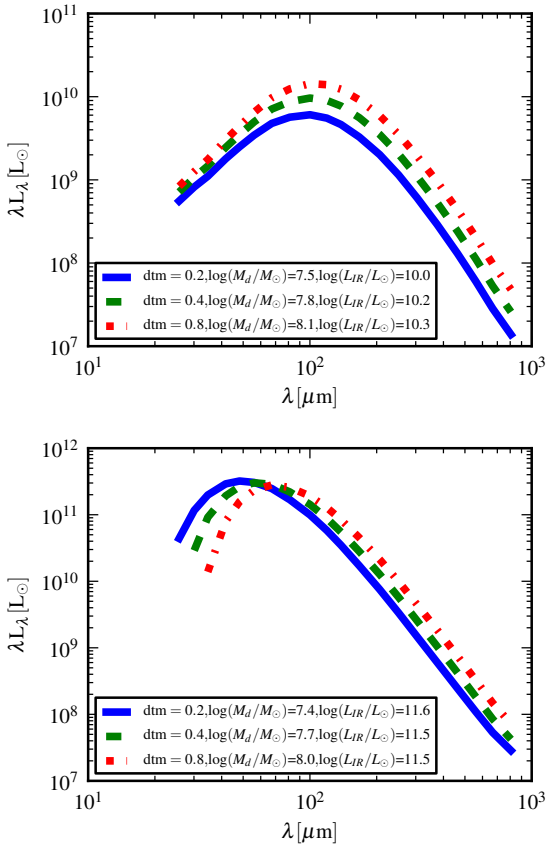

Figure 3.9: Shows the effect of changing the dust-to-metal ratio, and thus dust mass, on the SED. Each panel shows the SEDs of a simulated galaxy at a single time and viewed from a fixed viewing angle for three different dust-to-metal ratios, as specified in the legend; all other properties of the galaxies are unchanged. The $L_{\rm IR}$ and $M_{\rm dust}$ values for each SED are also shown in the legend. In the *top* panel, the galaxy is not fully opaque when the dust-to-metal ratio is 0.2. Consequently, as the dust-to-metal ratio is increased, $L_{\rm IR}$ increases by a factor of ~ 2, and the SED shifts only slightly to the right. In the *bottom* panel, $L_{\rm IR}$ decreases by 0.1 dex as the dust-to-metal ratio is increased; this is a consequence of the viewing-angle dependence of $L_{\rm IR}$ (see the text for details). The SED systematically shifts to longer wavelengths as the dust-to-metal ratio is increased, which is consistent with our expectation based on the relationship shown in Figure 3.8 and considerations of thermal equilibrium.

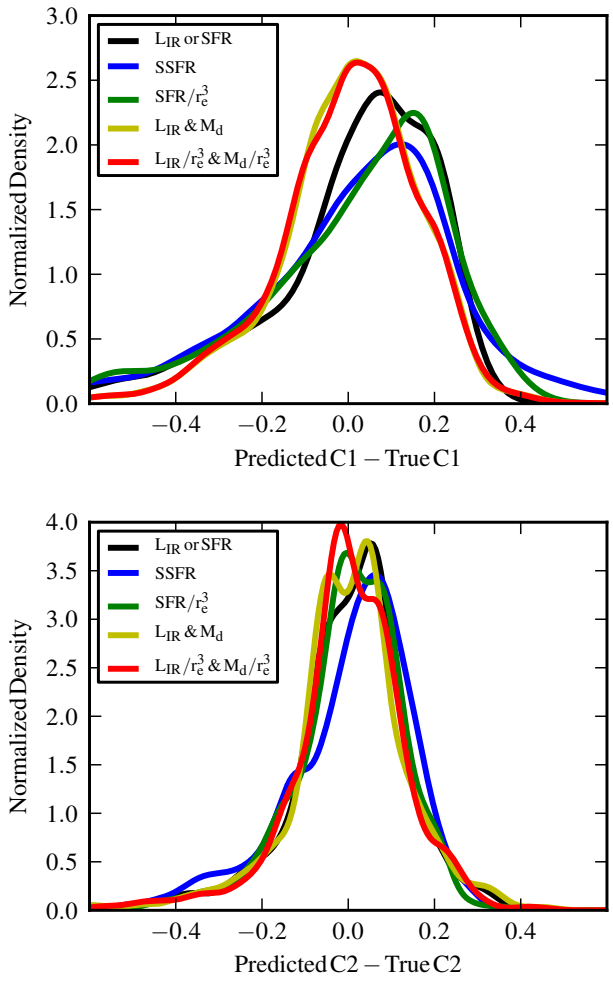

Figure 3.10: The difference between the predicted and true values of the coefficients for various estimators (similar to Figure 3.6). In this case, some of the estimators used include the galaxy sizes. The estimator used in each case is labeled in the legend, and in all cases, we use the logarithm of the parameter. For both C1 (*top*) and C2 (*bottom*), incorporating the size does not significantly increase the predictive power. We have experimented with other combinations of size such as using r_e^2 instead of r_e^3, also using different measures for the radius such as half mass radius of young stars, but we saw no improvement in the predictive power of the C1 or C2 and therefore do not present them here.

.

and vice versa.

3.6 Impact of galaxy sizes on the SED shape

In addition to the total absorbed luminosity and dust mass, both of which must affect the SED shape because of thermal equilibrium, the geometry of radiation sources and dust can influence the SED. The surface densities of various components (e.g., all stars, young stars, gas, and dust) are global (observable) parameters that crudely characterize the global geometry of a galaxy and are often used in observational studies to interpret the evolution in the FIR SED shapes of galaxies (e.g., Elbaz et al., 2011; Rujopakarn et al., 2013). Thus, it is worthwhile to investigate whether the PCA coefficients can be predicted better by incorporating information regarding the sizes.

We calculated the 3D baryonic half-mass radii (r_e) and used these to approximate various average volume densities by dividing integrated quantities – such as the SFR, $L_{\rm IR}$, and stellar, gas, and dust masses – by the half-mass radii cubed.[10] We then investigated whether various combinations of volume densities could be used to predict the values of C1 and C2 better than using our standard parameterizations, C1($L_{\rm IR}$,$M_{\rm dust}$) and C2($L_{\rm IR}$,$M_{\rm dust}$).

Figure 3.10 shows the difference between the true values of the PCA coefficients and those predicted using various estimators, as indicated in the legends (for clarity, we show only a subset of the combinations that we tried; the others fared comparably

[10]We opted to use volume densities rather than surface densities because the former are more relevant for the radiation transfer (albeit more difficult to infer from observations).

or worse). The top panel shows the results for C1, and the bottom shows those for C2. To relate the coefficients' values to a single galaxy parameter, we used models of the form $C1 = A \log X + B$, where X is the galaxy parameter indicated in the figure legend and A and B are fitting coefficients. Similarly, when two parameters were used, we employed models of the form $C1 = A \log X + B \log Y + C$.

Examination of Figure 3.10 reveals that incorporating the size of the system when predicting the coefficients yields yields at best a very marginal improvement in the predictive power compared with using the total IR luminosity and dust mass values alone. The difference in the final likelihood of the model where we use only L_{IR} and M_d to predict C1 and consequently reconstruct the SEDs and that of the model where we use $M_d/{r_e}^3$ and $L_{IR}/{r_e}^3$ to estimate the C1 coefficient and consequently predict the SEDs is negligible (~ 0). Therefore, based on the Akaike Information Criterion (AIC; Akaike, 1974), we prefer the model that does not have size as an extra parameter. Thus, we have not used the sizes to predict the SEDs. This lack of improvement from incorporating the galaxy sizes suggests that, at least for the simulated galaxies, the overall spatial extent does not play a significant role in determining the shape of the FIR SED. We discuss this perhaps surprising result in detail in Section 3.8.3.

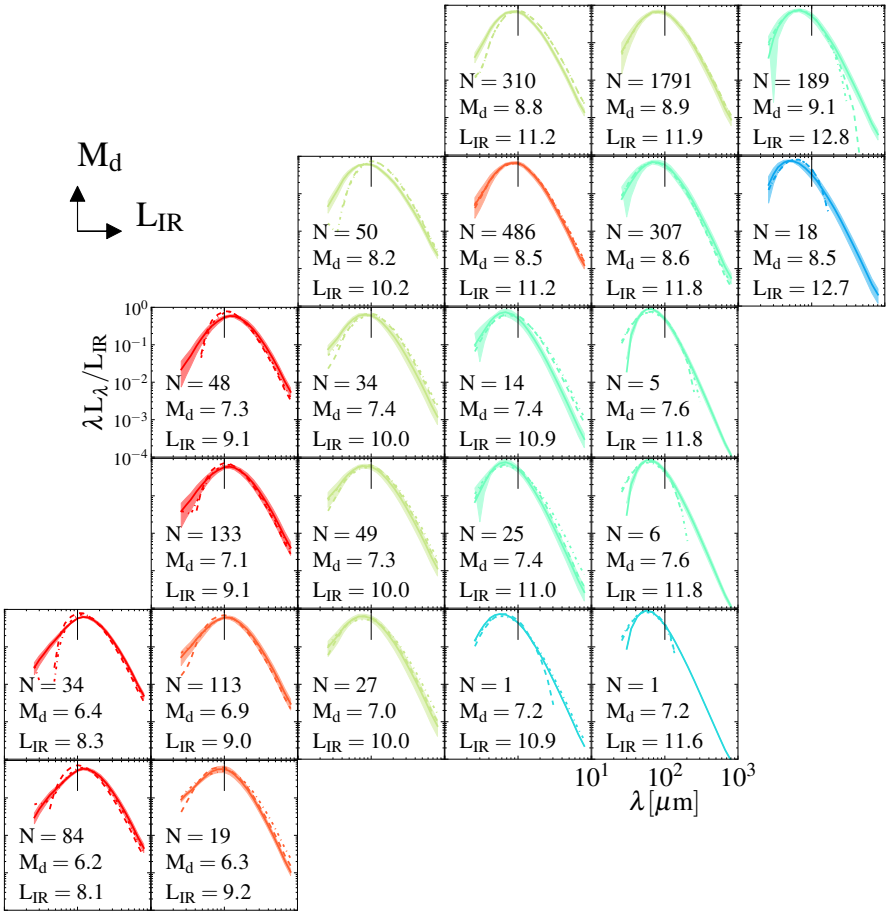

Figure 3.11: SEDs of our simulated galaxies binned according to IR luminosity and dust mass. In each panel, the median FIR SED in that bin is indicated by the solid line, and the shaded region represents the 16 – 84th percentile range of the FIR SEDs in that bin. The dashed (dot-dashed) line shows the SED predicted using PC1 (PC1 and PC2), with the coefficient(s) predicted using the median $L_{\rm IR}$ and $M_{\rm dust}$ values for that bin. The SEDs have been normalized by dividing by $L_{\rm IR}$. The color coding is based on where the peak of the FIR SED is located, with redder colors corresponding to longer peak wavelengths (i.e., colder effective dust temperatures). The logarithms of the median dust mass and IR luminosity (in solar units) are indicated in each panel, and the number of SEDs in each bin (N) is also shown. The dust mass increases in the upward direction, and $L_{\rm IR}$ increases to the right. In most columns, the SEDs become redder from bottom to top; this visually illustrates the trend for increasing $M_{\rm dust}$ to result in cooler SEDs when $L_{\rm IR}$ is fixed. In a given row, the SEDs become bluer from left to right because at fixed $M_{\rm dust}$, the SEDs become hotter as $L_{\rm IR}$ is increased. The trend with $L_{\rm IR}$ is more apparent that the with $M_{\rm dust}$ because except for the bottom row, the $L_{\rm IR}$ values in a given row span 2-3 orders of magnitude, whereas the $M_{\rm dust}$ values in a given column span only 1-2 orders of magnitude. Generally, the SEDs are predicted very well near their peaks. In some cases, the SEDs are underpredicted significantly at long wavelengths, although use of PC2 reduces the amount by which the SED is underpredicted compared with using only PC1.

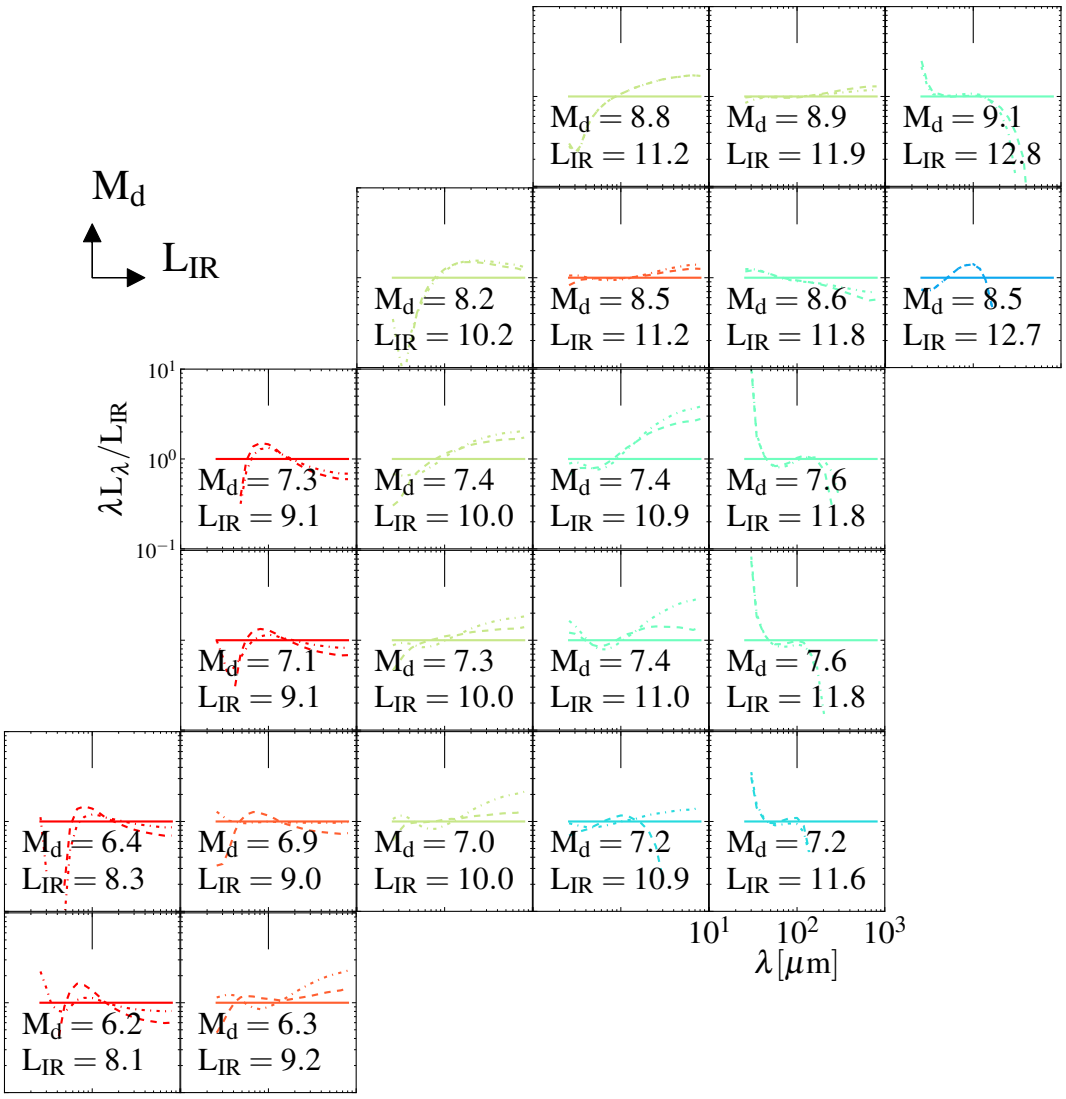

Figure 3.12: The predicted FIR SED divided by the true FIR SED when PC1 (PC1 and PC2) is (are) used to predict the median SED in each bin is shown by the dashed (dot-dashed) lines. The solid lines correspond to a ratio of unity. The $(L_{\rm IR}, M_{\rm dust})$ bins are the same as in Figure 3.11. This figure clearly shows that near their peaks, the median SEDs can be predicted well based on their $L_{\rm IR}$ and $M_{\rm dust}$ values alone. At wavelengths significantly shorter or longer than the peak wavelength, the SEDs are predicted very well in some bins but are sometimes incorrect by greater than an order of magnitude. Incorporating PC2 makes the predictions more accurate in some cases, but it can also make them worse.

3.7 Two-parameter FIR SED templates

Motivated by the results we have presented in the previous section, we now introduce a set of templates that is a function of both $L_{\rm IR}$ and $M_{\rm dust}$. [11] Motivated by the PCA results, we separated the simulations' FIR SEDs into ($L_{\rm IR}, M_{\rm dust}$) bins and calculated the median SED in each bin. These are shown in Figure 3.11. Each panel shows the median FIR SED for each bin as a solid line, and the 16–84th percentile range is indicated by the shaded area. The dashed lines represent the SEDs predicted by adding PC1 to the mean SED with the coefficient value predicted by inputting the median $L_{\rm IR}$ and $M_{\rm dust}$ values for each bin into Equation 3.5. The dot-dashed lines indicate the SEDs predicted when both PC1 and PC2 are used. The SEDs have been normalized by dividing by $L_{\rm IR}$ and are colored according to the wavelength at which the FIR peak is located, with redder colors indicating longer wavelengths. The trends revealed in the above analysis are apparent from the templates: (1) at fixed M_d, the SEDs become warmer as $L_{\rm IR}$ is increased (i.e., from left to right). (2) At fixed $L_{\rm IR}$, the SEDs become cooler when the $M_{\rm dust}$ is increased (i.e., from bottom to top).

Figure 3.12 shows the ratios of the predicted SEDs to the true SEDs, L'_λ/L_λ, both when only PC1 is used (dashed lines) and when both PC1 and PC2 are used (dot-dashed lines). These figures demonstrate that the median SEDs in each bin are best predicted near their peaks. Shortward of the SED peaks, the median SEDs of most bins can be predicted to within a few tens of percent. However, for some

[11] The templates are available at the following URL: `http://dx.doi.org/10.7910/DVN/X1OVSU`.

bins, the prediction is worse; in one (the bin with median values $M_{\rm dust} = 10^{6.4}$ $M_\odot$ and $L_{\rm IR} = 10^{8.3} L_\odot$), the SED is underpredicted by more than an order of magnitude at $\lambda \sim 35$ μm . At wavelengths > 150 μm , the SEDs are sometimes predicted to within a few tens of percent. However, in many bins, the SEDs are underpredicted considerably. Using PC2 in addition to PC1 sometimes makes the prediction better (i.e., the dashed line is closer to 1 than is the solid line).

The goal of PCA is to explain the variance in a dataset. Thus, it is unsurprising that the peaks of the SEDs are predicted best, because this is the region that dominates the variance in the dataset. Because the luminosity density at long wavelengths is $\sim 1-2$ orders of magnitude less than that at the SED peak, the long-wavelength regions of the SEDs contribute relatively little to the variance. Consequently, it would be necessary to use higher-order PCs to predict the long wavelength emission well.

3.8 Discussion

3.8.1 The simplicity of the FIR SEDs of galaxies

We have found that the FIR SEDs of our simulated galaxies can be well predicted based on the galaxies' IR luminosities and dust masses alone. Our results extend those of Hayward et al. (2011a), who demonstrated that the observed-frame submm flux densities of simulated $z \sim 2$ SMGs could be well predicted using these two parameters. Moreover, as noted in Section 3.4, C1 effectively depends on $\log L_{\rm IR}/M_{\rm dust}$ because

the best-fitting coefficients for ($L_{\rm IR}$ and $M_{\rm dust}$) have almost the same magnitude but opposite signs (0.52 and -0.47, respectively). Interestingly, in the simple isothermal modified blackbody model, the dust temperature scales with $L_{\rm IR}/M_{\rm dust}$.[12] In the more realistic case of a continuum of dust temperatures, the mean intensity of the radiation absorbed by the dust is proportional to $L_{\rm IR}/M_{\rm dust}$ (Draine & Li, 2007). Thus, both simple models and our simulations suggest that the ratio $L_{\rm IR}/M_{\rm dust}$ is a key determinant of the FIR SED of a galaxy.

These results indicate that the FIR SEDs of our simulated galaxies are rather simple. The skeptical reader may suggest that this simplicity is a consequence of the simplicity of our simulations. However, even in the simulations, the FIR SEDs could in principle exhibit greater complexity because the simulated galaxies contain dust with a continuum of temperatures (which are set by the 3D interstellar radiation field, 3D distribution of dust, and grain properties). Thus, the fact that $L_{\rm IR}/M_{\rm dust}$ encodes so much of the variance in the simulated SEDs is somewhat surprising.

Similar conclusions have been obtained based on observed FIR SEDs of galaxies. In particular, by fitting observed galaxy SEDs using the model of Draine & Li (2007), Magdis et al. (2012b) have argued that the redshift evolution of 'main sequence' galaxies' SEDs is driven by redshift evolution in the $L_{\rm IR}/M_{\rm dust}$ ratio. For this reason, they suggest using SED templates for 'main sequence' galaxies that depend on $L_{\rm IR}/M_{\rm dust}$.

[12]However, it is important to note that how the effective dust temperatures of the simulated galaxies' SEDs depend on $L_{\rm IR}/M_{\rm dust}$ is not fully captured by this model (Lanz et al., 2014).

Magnelli et al. (2013b) studied how the effective temperature of galaxies depends on their position in the SFR–$M_\star$ plane and redshift. They found that at all redshifts, the effective dust temperature smoothly increases with $L_{\rm IR}$, specific SFR, and the distance from the 'main sequence' (i.e. excess SSFR relative to what one would expect for a 'main sequence' galaxy of the same mass), with the latter two correlations being more significant than the first. They interpret the dependence on the distance from the 'main sequence' in terms of changes in the global star formation efficiency, SFR/$M_{\rm gas}$. However, we note that for an approximately constant dust ratio, this quantity would serve as a proxy for $L_{\rm IR}/M_{\rm dust}$. Thus, the results of Magnelli et al. (2013b) are likely consistent with those of Magdis et al. (2012b) and this work.

3.8.2 Observational support for the importance of dust mass

Observational studies of the dust masses of different types of galaxies, including submillimetre galaxies (Rowlands et al., 2014a), normal massive star-forming galaxies (Dunne et al., 2011b), early type galaxies (Martini et al., 2013) and high-redshift galaxies (Michałowski, 2015a), all point to the presence of unexpectedly large quantities of dust in high-redshift galaxies. For example, Rowlands et al. (2014a) found that the dust masses of submillimetre galaxies could be as much as two orders of magnitude greater than the expectations from the inferred star-formation histories

and theoretical dust production and destruction rates.

Moreover, observations indicate that at fixed $L_{\rm IR}$, $z \sim 2-3$ galaxies have lower effective dust temperatures than do local galaxies (Casey et al. 2014a and references therein). Our results suggest that the observed trend could be a natural consequence of high-redshift galaxies having more dust per unit IR luminosity. Thus, the evolution of the effective dust temperature–IR luminosity relation might be a consequence of evolution in the global properties of the ISM of galaxies rather than changes in the small-scale geometry of star-forming regions.

The dust mass of a galaxy depends on the gas mass, gas-phase metallicity, and dust-to-metal ratio. As stars are formed, the ISM is enriched, which can increase the dust mass. However, star formation simultaneously reduces the dust content of the ISM because the stars are formed from dust-enriched gas. Simple models that encapsulate this competition between gas enrichment and consumption indicate that the maximum dust mass of a galaxy depends weakly on the gas fraction: it is maximal when the gas fraction is 37 percent, but it varies by less than a factor of 3 for gas fractions in the range of 4–86 percent (Edmunds & Eales, 1998). This result is for a closed box, but the limit also holds if outflows or unenriched inflows are allowed. Thus, although $z \sim 2-3$ ULIRGs are less metal-rich than local ULIRGs, they may still have higher dust masses.

There is some observational evidence that supports our claim that the lower effective dust temperatures of $z \sim 2-3$ ULIRGs are associated with higher dust masses

relative to local ULIRGs. Figure 3.13 shows $L_{\rm IR}$ versus $M_{\rm dust}$ for a sample of local LIRGs and ULIRGs (U et al., 2012) and a sample of $z \sim 2-3$ SMGs (da Cunha et al., 2015). For $L_{\rm IR} \sim 10^{11.5-12.5} L_{\odot}$, the local ULIRGs have a median dust mass of $10^{7.43}$ $\rm M_{\odot}$, whereas the $z \sim 2-3$ SMGs have a median $M_{\rm dust} \approx 10^{8.64}$ $\rm M_{\odot}$. Thus, the SMGs have dust masses that are more than an order of magnitude greater than those of the $z \sim 0$ ULIRGs. We argue that the increased dust masses are the reason that the SMGs have cooler SEDs. This is consistent with Magdis et al. (2012b) suggestion that $z \sim 0.5-2$ 'main sequence' ULIRGs have cooler SEDs than local ULIRGs because the former have lower $L_{\rm IR}/M_{\rm dust}$ ratios.

We have used the $L_{\rm IR}$ and $M_{\rm dust}$ data from da Cunha et al. (2015) because they were inferred from high-resolution ALMA data and *Herschel* data that were deblended based on the ALMA data. Thus, their photometry should be much less affected by blending than typical datasets from *Herschel* and other single-dish FIR/(sub)millimeter telescopes. This is highly desirable, because the fact that blending becomes more severe at longer wavelengths could cause the SEDs extracted from blended data to be colder than the true SEDs of individual sources. However, the significant caveat regarding our use of this dataset is that the SMG selection is biased toward colder effective dust temperatures, and thus the $L_{\rm IR}/M_{\rm dust}$ values of $z \sim 2$ SMGs likely do not represent the full range of $L_{\rm IR}/M_{\rm dust}$ values exhibited by $z \sim 2$ ULIRGs. To conclusively determine how the $L_{\rm IR}/M_{\rm dust}$ ratios of $z \sim 2$ ULIRGs compare with those of local ULIRGs, high-resolution FIR and (sub)millimeter ob-

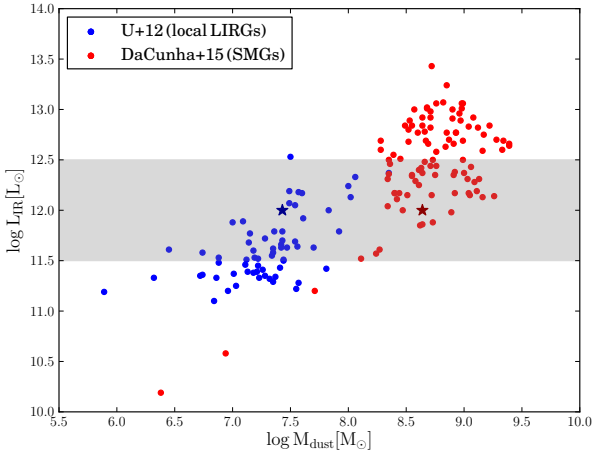

Figure 3.13: IR luminosity versus dust mass for two samples of IR-luminous galaxies, local LIRGs and ULIRGs from U et al. (2012) and $z \sim 2-3$ SMGs from da Cunha et al. (2015). The stars indicate the median dust mass for the subset of each sample within the shaded region, which is defined by $10^{11.5} < L_{\rm IR}/L_{\odot} < 10^{12.5}$. The median dust mass of the SMGs is an order of magnitude greater than that of the local (U)LIRGs.

servations of a sufficiently large, unbiased (in terms of effective dust temperature) sample of $z \sim 2$ ULIRGs are required.

3.8.3 The unimportance of galaxy sizes in determining the SED shape

In Section 3.6, we demonstrated that incorporating information regarding the galaxy sizes did not significantly improve our ability to predict the FIR SEDs. This result may be surprising to some readers, given that it is often suggested that $z \sim 2$ ULIRGs have lower effective dust temperatures than local ULIRGs because the former

are more extended (e.g., Elbaz et al., 2011; Rujopakarn et al., 2011, 2013). It is true that for a central source surrounded by dust (i.e., the 'shell' geometry of Misselt et al. 2001b), increasing the spatial extent of the absorbing material will result in colder dust because the dust grains receive a more 'diluted' radiation field. This geometry may be a reasonable approximation (especially if the shell is allowed to be clumpy) for individual HII regions and highly obscured AGN. Indeed, more compact HII regions exhibit hotter dust temperatures (e.g., Groves et al., 2008). However, the overall geometry of both real galaxies and our simulated galaxies is likely more similar to the 'dusty' geometry of Misselt et al. (2001b), in which the stars and dust are mixed, because both the SFR density and dust density are correlated with the gas density (see also Jonsson et al. 2006). In such a geometry, the temperature of the dust is insensitive to the size (assuming that the sizes of the stellar and dust distributions are scaled in the same manner; Misselt et al. 2001b).

It is worth considering suggestions in the literature that the correlation between the $L_{\rm IR}$ surface density ($\Sigma_{L_{\rm IR}}$) and T_d is tighter than that between $L_{\rm IR}$ and T_d, which would suggest that size is important for determining the FIR SED shape, in contrast with our findings. As discussed below, the observational evidence in favor of a correlation of dust temperature with galaxy size is somewhat tentative; this seems to have become conventional wisdom perhaps based more on the the intuition that an individual dust grain will become cooler as it is moved away from the radiation source. However, this naive physical picture is overly simplistic: as already demon-

strated by Misselt et al. (2001b) over a decade ago, for a more realistic geometry in which dust and sources are intermixed, the overall size of the galaxy does not affect the characteristic dust temperature.

A literature search did reveal a few works that are particularly relevant. Chanial et al. (2007) used radio continuum-derived sizes as a proxy for IR sizes to compute the IR luminosity surface density for two samples of IR-luminous galaxies, one selected at 60 μm and the other selected at 100 μm . They argued that introducing galaxy size as an additional parameter reduced the dispersion in the $L_{\rm IR} - T_d$ relation. Moreover, their bootstrap estimation of the power-law indices indicated that the 60-to-100-μm flux ratio (which was used as a proxy for dust temperature) depended on the IR surface density. However, they did not investigate the effect of including dust mass as a parameter. Thus, their results are not necessarily inconsistent with our result that incorporating size does not increase our ability to predict the FIR SEDs relative to when $L_{\rm IR}$ *and* $M_{\rm dust}$ are used. It would certainly to be worthwhile to perform a similar analysis using *Herschel* data and including dust mass as a parameter.

Elbaz et al. (2011) found that IR8$\equiv L_{8\mu{\rm m}}/L_{\rm IR}$ and $\Sigma_{L_{\rm IR}}$ are correlated. They argued that IR8 is correlated with the IR luminosity surface density (i.e. compactness) and 'starburstiness' of galaxies. (However, we note that whether the strength of this correlation differed significantly from that between IR8 and $L_{\rm IR}$ was not quantitatively demonstrated.) They then constructed template SEDs for extended ('main sequence') and compact ('starburst') galaxies. It could be argued that the differences in the

effective dust temperatures of their 'starburst' and 'main sequence' SEDs (40 and 31 K, respectively) supports the suggestion that effective dust temperature is inversely correlated with IR luminosity surface density. However, we note that their compact galaxies, which they suggest are starbursts, are systematically more luminous than the non-compact, 'main sequence' galaxies (e.g. their Fig. 16). Thus, the differences in the two SEDs may be driven by differences in IR luminosity, and it is unclear whether galaxy size plays a role.

Rujopakarn et al. (2011) reported a correlation between L_{IR} and $\Sigma_{L_{\rm IR}}$; as in Chanial et al. (2007), the IR size was inferred from radio continuum observations. However, the authors did not quantify the extent to which using IR luminosity surface density rather than IR luminosity reduced the dispersion in the correlations (or even if it did). Closer inspection of the sizes in Rujopakarn et al. (2011) indicates that they exhibit a large scatter with no clear trend between size and L_{IR}, except for local LIRGs, which have smaller sizes than less-luminous local star-forming galaxies. Therefore, the correlation between L_{IR} and $\Sigma_{L_{\rm IR}}$ in Rujopakarn et al. (2011) is likely to be largely driven by the intrinsic correlation between $L_{\rm IR}$ and $L_{\rm IR}$. Moreover, in an independent study, Tateuchi et al. (2015) measured the Paα sizes of local LIRGs and found no correlation between $L_{\rm IR}$ and size.

We conclude that the existing evidence that correlation between effective dust temperature and IR luminosity density is stronger than that between effective dust temperature and IR luminosity (i.e. that galaxy size is affects the IR SED shape

when $L_{\rm IR}$ is fixed) is weak, and this topic is worthy of further investigation. ALMA should be incredibly helpful in this regard because it can probe the rest-frame FIR emission of high-redshift galaxies at sub-arcsecond resolution. Thus, ALMA can be used to directly measure FIR sizes rather than relying on sizes from e.g. radio observations (although nuclear starbursts may still be unresolved; Scoville et al. 2015). Moreover, ALMA maps can be used to de-blend data from FIR telescopes such as *Herschel*, thereby providing FIR SEDs that are minimally affected by blending. We look forward to seeing whether ALMA observations confirm our predictions.

We have not computed the luminosity surface densities because we only computed integrated SEDs owing to computational constraints. Our analysis indicates that the 3-D size, which is arguably the most physical measure of the relative distribution of stars and dusts, plays a subdominant role in the determination of the FIR SED shape. However, it is possible that a correlation between luminosity surface density at some wavelengths arises because of radiative transfer effects. For example, all else being equal, if the total dust mass is increased by increasing the dust-to-metal ratio (such that the relative spatial distribution is fixed), dust self-absorption can cause the radius measured from dust emission to increase because the $\tau = 1$ surface will move outward. Thus, the luminosity surface density would decrease and, based on the results we have presented, the SED would become colder (because of the increased dust mass). This effect could introduce a correlation between IR luminosity surface density and effective dust temperature, but it would not indicate that the *physical*

size of the galaxy affects the SED shape (because in the test described above, the half-mass radius would not change). We defer a detailed exploration of this issue to future work.

3.8.4 The origin of catastrophic failures in the SED prediction

Figure 3.7 indicates that most galaxies for which the SED prediction is a catastrophic failure (i.e., $\chi_r^2 >> 10$) have either high $L_{\rm AGN}/L_{\rm IR}$ or/and $L_{\rm IR} > 10^{12.5} L_{\odot}$. There are a few potential reasons that the SEDs of such sources would prove to be especially difficult to predict. For the simulated galaxies in which the AGN contributes significantly to the bolometric luminosity, the AGN can heat host-galaxy dust and cause FIR emission (this will be discussed in detail in Hayward et al., in prep. and Roebuck et al., in prep.) Sources in which the AGN dominates the dust heating can differ from star formation-dominated sources in terms of the SED of the radiation absorbed by the dust. The geometry of such sources may also qualitatively differ: when the AGN dominates, the geometry is more similar to the 'shell' geometry of Misselt et al. (2001b) than the mixed geometry, whereas the latter should better describe sources in which star formation dominates the dust heating, as argued in the previous subsection. Finally, in the AGN-dominated and most-IR luminous sources, dust self-absorption is likely more significant than in the other sources. Some

or all of the above differences between star formation-powered and AGN-powered IR sources may explain why the SEDs of many of the sources with high $L_{\rm AGN}/L_{\rm IR}$ or/and $L_{\rm IR} > 10^{12.5} L_{\odot}$ cannot be predicted well.

3.8.5 Implications for IR counts in hierarchical models

Cosmological galaxy formation models have long struggled to correctly reproduce the observed IR and sub-mm counts without introducing fairly radical assumptions such as an extremely top-heavy stellar initial mass function (Devriendt & Guiderdoni 2000; Baugh et al. 2005b; Lacey et al. 2010; Davé et al. 2010; Somerville et al. 2012; Niemi et al. 2012, but cf. Hayward et al. 2013b; see also the discussion in Casey et al. 2014a). Due to the infeasibility of carrying out full 3D radiative transfer calculations on a cosmological hydrodynamic simulation (see 3.8.6), to date most such calculations have relied on semi-analytic models combined with a simplified approach to computing the FIR SEDs. For example, the models of Devriendt & Guiderdoni (2000) and Somerville et al. (2012) used empirical libraries of dust emission templates parameterized only by $L_{\rm IR}$. These libraries clearly cannot capture the observed redshift evolution of the relationship between effective dust temperature and IR luminosity. The SAMs presented by Somerville et al. (2012) and further investigated by Niemi et al. (2012) underpredicted IR number counts at wavelengths > 100 μm , and the

discrepancy became worse with increasing wavelength. Our work here suggests a straightforward and physically motivated way to improve the modeling of dust emission in SAMs by using templates that depend on both $L_{\rm IR}$ and $M_{\rm dust}$. Our results are also encouraging for the use of SAMs to model dust emission for large samples of galaxies, as they suggest that the sizes and detailed geometries of galaxies (which are properties that SAMs cannot model accurately) are sub-dominant compared to the global parameters $L_{\rm IR}$ and $M_{\rm dust}$.

If indeed the dust is colder (at fixed $L_{\rm IR}$) in high-redshift galaxies, as indicated by observations, adopting two-parameter templates like the ones we have presented here will clearly work in the direction of alleviating the tension between the SAM predictions and observations. Accounting for the effects of blending will further reduce the discrepancy (Hayward et al., 2013a,b; Muñoz Arancibia et al., 2014; Cowley et al., 2015). However, whether SAMs will predict a strong enough evolution of $M_{\rm dust}$ with $L_{\rm IR}$ and redshift to reproduce the observed IR-submm counts, once observational effects such as blending have been taken into account, remains to be seen. We plan to investigate this by incorporating two-parameter dust emission templates in the Somerville et al. (2008b) SAM in a future work (Safarzadeh et al., in prep.).

3.8.6 Limitations and future work

The detailed simulation methodology that we have employed in this work has the advantages of being well studied, and in previous works, the specific simulations used

in this work and similar simulations have been demonstrated to reproduce the properties of a wide range of real galaxies, as discussed in Section 3.1. However, there are naturally some limitations. First, because of the manner in which our sample was constructed, the demographics of the population are by no means representative of those of the real Universe. To achieve a cosmologically representative population, it would be necessary to perform 3D radiative transfer on galaxies selected from a large-volume cosmological simulation. Unfortunately, such simulations typically have spatial resolution > 1 kpc and thus do not resolve galaxy disk scaleheights, much less the internal structure of the ISM. Moreover, state-of-the-art cosmological simulations lack starbursts (i.e., there are significantly fewer outliers above the 'star formation main sequence' than observed; Sparre et al. 2015b), which are thought to power local ULIRGs and a non-negligible fraction of $z \sim 2 - 3$ ULIRGs (Hopkins et al., 2010a; Hayward et al., 2013a,b; Cowley et al., 2015). Consequently, the utility of such simulations for investigating the FIR SEDs of galaxies remains limited. Cosmological 'zoom-in' simulations can be used to achieve orders-of-magnitude better spatial resolution; thus, radiative transfer can be meaningfully applied to such simulations (e.g., Granato et al., 2015). However, the considerable computational expense of such simulations strongly constrains the subset of the parameter space that can be sampled.

Even for idealized, comparatively simple simulations such as ours, the computational expense required to perform the radiative transfer is significant. Consequently, the parameter space spanned by our simulation suite is not exhaustive, and the sam-

pling of the parameter space is rather coarse. This limitation can be addressed in the future through the use of a (considerably) larger simulation suite or through performing radiative transfer on all resolved galaxies in a large-volume cosmological simulation; however, we again stress that for the latter, the limited spatial resolution will continue to be a significant hurdle for the foreseeable future. We have no reason to expect that our qualitative conclusions would differ if we were to use a larger or/and cosmologically representative simulation suite, especially given the demonstrated agreement between our simulated galaxies' and real galaxies' SEDs. However, it is possible that the details, such as the variation in the SED templates, are sensitive to the specific simulations used.

Another significant limitation is that the hydrodynamical simulations do not resolve the detailed structure of the ISM, both because of the spatial resolution and the ISM model employed. As discussed in Section 5.2, we assume that the dust is uniformly distributed on sub-resolution scales. Using our current methods, it is possibly to crudely characterize the uncertainty associated with the sub-resolution ISM structure by comparing two extremes, the default model and one in which the dust in the cold clouds implicit in the Springel & Hernquist (2003) ISM is completely ignored (i.e., the clumps have a volume filling factor of zero). We have performed such a comparison and found that the results do not qualitatively differ. In fact, it is actually easier to predict the SEDs when the latter treatment is used. We speculate that the reason for this result is that all optical depths are smaller (by construction);

consequently, dust self-absorption is less significant.

Moreover, we by no means claim that our treatments of stellar and AGN feedback are state-of-the-art, and various groups are now utilizing more sophisticated and likely more realistic feedback models (e.g., Agertz et al., 2013; Agertz & Kravtsov, 2015; Hopkins et al., 2014a). However, to our knowledge, no UV–mm SEDs for such simulations have been presented in the literature; thus, the SEDs used in this work still represent the state-of-the-art for UV–mm SEDs computed by performing dust radiative transfer on hydrodynamical simulations. Computations of UV–mm SEDs of galaxies from the Feedback in Realistic Environments (FIRE) cosmological zoom-in simulations (Hopkins et al., 2014a) using *Sunrise* are underway, but this is a significant undertaking in and of itself. Our method could be applied to these and other SED datasets in the future.

Finally, we have demonstrated that PCA is a useful tool for identifying which parameters drive the variation in galaxy SEDs. However, the PCA results cannot be used to predict SEDs of galaxies outside of our parameter space because the mean SED and PCs depend on the dataset on which the PCA is performed. Moreover, because of the dependence on the mean SED and the fact that our simulation suite is not cosmologically representative in terms of the galaxy demographics, the PCA results cannot even be used to predict the SEDs for samples in which the parameter space is a subset of that spanned by our simulations but the distribution within the parameter space differs. Thus, the templates that we provide are a better tool for

predicting FIR SEDs than are the PCA results. Moreover, other statistical methods, such as neural networks, may prove to be more useful than PCA for this purpose (e.g., Silva et al., 2012).

3.9 Conclusions

We performed PCA on a sample of FIR SEDs of simulated galaxies that we generated by performing dust radiative transfer on hydrodynamical simulations in post-processing. Our goal was to determine what drives the variation in galaxies' FIR SEDs. Our main conclusions are the following:

- The PCA indicated that only two PCs are sufficient to explain 97 percent of the variance in our SED sample. The first component characterizes the peak of the SED, whereas the second characterizes the breadth of the peak.

- The coefficient of the first PC, C1, is correlated with the IR luminosity, SFR, and AGN luminosity. This result indicates that the SEDs are hotter when the IR luminosity, SFR, or AGN luminosity are greater.

- Incorporating dust mass increases our ability to predict the value of C1 and thus the FIR SEDs. At fixed IR luminosity, increased dust mass leads to lower C1 values and thus cooler SEDs.

- The coefficient of the second PC, C2, is weakly anti-correlated with IR luminos-

ity, SFR, AGN luminosity, and dust mass. It can also be predicted using $L_{\rm IR}$ and $M_{\rm dust}$, but the dependences on both quantities are weak. Using the second PC improves how well the SEDs can be predicted in some cases but makes the predictions worse in others.

- Examination of the catastrophic failures to reconstruct SEDs revealed that the bulk of such SEDs correspond to simulated galaxies with high AGN fractions or/and $L_{\rm IR} > 10^{12.5} L_{\odot}$. For this sample, we were unable to predict the PC coefficients and thus SEDs well.

- Incorporating galaxy sizes does not improve our ability to predict the SEDs. Previous work (Misselt et al., 2001b) has demonstrated that when sources and dust are well mixed, the overall spatial extent of the system does not affect the dust temperature. Because in the simulations (and likely in reality), both star formation and dust density are correlated with gas density, the geometry more resembles such a mixed geometry than a 'shell' or 'foreground screen' geometry in which the dust surrounds a central source (and for which the size of the system *does* affect the dust temperature). Thus, our result is consistent with the calculations of Misselt et al. (2001b). A review of the literature indicated that the evidence that the correlation between effective dust temperature and IR luminosity surface density is stronger than that between effective dust temperature and IR luminosity is rather weak.

- The above conclusions suggest that the redshift evolution in effective dust temperature (i.e., at fixed $L_{\rm IR}$, $z \sim 2-3$ galaxies exhibit lower effective dust temperatures compared with $z \sim 0$ galaxies) is not a consequence of higher-redshift ULIRGs being more extended, as is often suggested. Instead, our work suggests that this difference is driven by $z \sim 2-3$ ULIRGs having higher dust masses at fixed $L_{\rm IR}$ (because of their higher gas fractions than local galaxies), as suggested by some observations.

- Because of the importance of dust mass in determining the FIR SED shape, a two parameter set of IR SED templates that depend on both $L_{\rm IR}$ and $M_{\rm dust}$ should be superior to those that depend on $L_{\rm IR}$ alone. We have generated such a set of templates based on our simulated SEDs and made them publicly available. They should be useful for fitting observed galaxy SEDs and predicting galaxy SEDs in unobserved wavelength regimes, and they can be used to predict IR SEDs of galaxies in cosmological simulations and SAMs as long as the luminosity absorbed by dust and dust mass can be estimated.

Chapter 4

Semi Analytic Modeling of dust attenuation

4.1 Introduction

In modeling large statistical samples, it is important to have fast approximate methods for characterizing the attenuation, scattering, and re-emission of radiation incident on interstellar dust as a function of a small number of global parameters of the galaxy. Such a library could be provided by SAMs that have dust treatment implemented in them (Somerville et al., 2008c, 2012) or when the output of a SAM is coupled to the radiative transfer simulations with simple assumptions regarding the geometry of dust with respect to the radiation sources(Silva et al., 1998; Granato et al., 2000b; Baugh et al., 2005c; Lacey et al., 2008; Fontanot et al., 2009b).

We would like to know how much information about the FIR emission of the galaxies is encoded in their FUV-NIR part of the SEDs. We need observed samples that cover the whole range from the FUV to the FIR with robust FIR estimates that are free from the confusion noise present at high redshift FIR measurements. Two local samples match our requirement. The Spitzer Infrared Nearby Galaxy Survey (SINGS, Kennicutt Jr et al., 2003b) and the Great Observatories All-Sky Luminous Infrared Galaxy Survey (GOALS, Armus et al., 2009b). The SINGS sample consists mostly of normal star-forming galaxies spanning a wide range of L_{IR}. The GOALS sample consists of galaxies classified as LIRGS and ULIRGS – with infrared luminosities $L_{IR}(8-1000\mu m) > 10^{11}L_{\odot}$. We predict the FIR luminosity of both sample of galaxies by SED fitting in FUV-NIR range against galaxies in our mock library.

A parallel approach to account for the effect of dust on the intrinsic SED of galaxies is to model the observed attenuation in the rest frame UV part of the SED through the UV continuum slope β ($f_{\lambda} \propto \lambda^{\beta}$:Meurer et al. 1999b; Calzetti et al. 1994b; Reddy et al. 2012a). However, the large scatter in the correlation between β and the ratio of FIR to UV luminosity $IRX = \log L_{IR}/L_{UV}$(Meurer et al., 1999b) renders its ability to estimate the extinction problematic (Conroy, 2013). Moreover, extremely dusty galaxies such as LIRGs and ULIRGs do not obey any well-defined $\beta - IRX$ relation (Goldader et al., 2002; Howell et al., 2010a; Casey et al., 2014b). Even if the attenuation in the rest-UV is known, galaxies can have a diversity of

attenuation curves, i.e. the attenuation as a function of wavelength (A_λ).

Similar approaches to what has been done in this paper, namely to use the information in the SED shape (UV-optical) to constrain the extinction parameters, have been carried out in the literature to study high redshift galaxies. Different libraries are used in the literature based on different assumed star formation histories (SFH), from an exponentially declining SFR, referred to as τ-models (Maraston et al., 2010), to rising SFHs that seem more suitable for high redshift galaxies (Lee et al., 2010; Pforr et al., 2012; Lee et al., 2014). Cosmological galaxy evolution models provide more complex SFHs and chemical enrichment (Pacifici et al., 2012, 2014), and a similar approach is adopted in this study.

Our SED library is based on the SAM presented in Somerville et al. (2012, hereafter S12) and Somerville et al. (2008c). These models are based within the cosmological framework of Λ Cold Dark Matter (ΛCDM), represented via dark matter halo merger trees, and have a diverse set of cosmologically motivated SFHs. Dust attenuation arises from two components: dense, cold "birth clouds" that enshroud young stars, and a more diffuse, extended cirrus component, as suggested in the models presented by (Charlot & Fall, 2000b, hereafter CF00). The attenuation due to the diffuse component depends on the galaxy inclination via a simple "slab" model. Unlike in the original CF00 model, the dust optical depth of both components is linked to physical parameters of the galaxies, such as their cold gas content, gas phase metallicity, and size. We then simply assume that all energy absorbed by dust is re-radiated in the IR

(we neglect scattering). The dust treatment in S12 model has been compared with more detailed radiative transfer calculations and found to provide good agreement (Fontanot et al., 2009b).

da Cunha et al. (2008) find CF00 can indeed explain the IR luminosity of the observed SINGS sample based on SED fitting against the MAGPHYS library of SEDs. An advantage of using libraries based on cosmologically situated galaxy evolution models, over purely parametric approaches such as MAGPHYS, is that real galaxies show many correlations between their physical, structural and spectrophotometric properties, and state-of-the-art models are at least qualitatively successful at reproducing these correlations and the demographics of different types of galaxies (e.g. Somerville & Davé, 2014, and references therein). For example, the part of MAGPHYS that estimates the stellar SED, including the modeling of dust attenuation, is extremely similar to our approach. The main difference is that SAMs provide an ensemble of diverse and physically motivated star formation and chemical enrichment histories, and produce galaxies with sensible correlations between properties like mass, physical size, gas content, and metallicity, which we make use of in our dust modeling.

The structure of the paper is as follow: In Section 4.2 we describe how we have complied the data from the SINGS and GOALS sample avoiding possible aperture mis-match between different set of observations and excluding active AGNs from either of the samples. In section 4.3 we describe in more detail the physics of galaxy

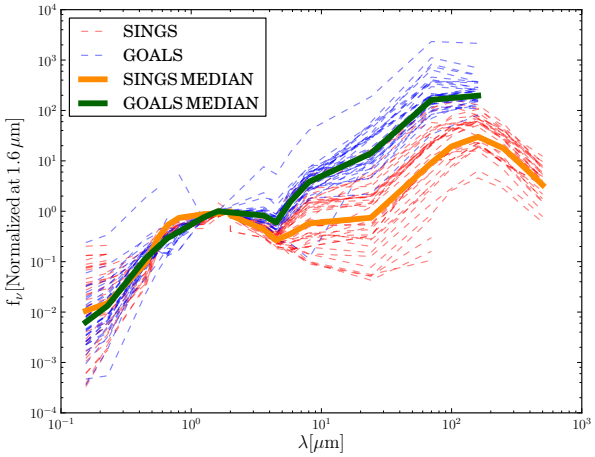

Figure 4.1: Showing the individual SEDs for both SINGS and GOALS sample that is used in this study and outlined in the text in detail about their selection criteria. The solid lines show the median SED of the respective sample.

formation and dust treatment implemented in the SAM. Section 4.4 describes the details of the SED fitting. We present our results in section 5.3 with discussion of the result presented in section 4.6 and the summary in section 4.7.

4.2 Data

We have compiled the full FUV to FIR SEDs of two reference samples of nearby galaxies, the SINGS and GOALS sample. Figure 4.1 shows the individual galaxies in each sample with dashed lines and the median of each sample with solid lines as labeled in the figure. In the following we describe in detail how we selected a subsample of galaxies from SINGS and GOALS samples.

4.2.1 SINGS sample

We assemble the SEDs with GALEX UV and IRAC/MIPS IR data from Dale et al. (2007b) , optical data from Muñoz-Mateos et al. (2009) and sub-mm data from Dale et al. (2012). The optical BVRI data in Dale et al. (2007b) suffered from zero-point calibration problems, so we use the SDSS data and re-calibrated BVRI data in Muñoz-Mateos et al. (2009) instead. The full SINGS sample has 75 galaxies, spanning a wide range in optical morphology, luminosity and infrared to optical ratio. We remove 9 galaxies (NGC 0584, NGC 1404, NGC 3034, NGC 4552, M87 Dwarf A, M87 Dwarf B, Holmberg IX, DDO 154 and DDO 165) due to background contamination, detection saturation or poor detection issues as explained in Draine et al. (2007b) Then we remove 8 galaxies for which GALEX FUV fluxes are not available. Finally we remove 15 galaxies for which no optical fluxes are available to arrive at a sample of 43 galaxies. Each galaxy in the resultant sample has complete data in the UV, near-IR and IRAC/MIPS bands, and at least 2 bands in the optical. Our SED selection procedure happens to eliminate most of the elliptical and irregular galaxies.

For the SINGS sample, we compute the sample's L_{IR} following (Dale & Helou, 2002b):

$$\begin{aligned} L_{\rm TIR} = \zeta_1 \nu L_\nu(24\mu{\rm m}) + \\ \zeta_2 \nu L_\nu(70\mu{\rm m}) + \zeta_3 \nu L_\nu(160\mu{\rm m}) \end{aligned} \tag{4.1}$$

where $[\zeta_1, \zeta_2, \zeta_3] = [1.55, 0.76, 1.34]$. According to this definition, the total infrared is

the dust continuum emission between 3 and 1100 μm.

4.2.2 GOALS sample

From GOALS sample, U et al. (2012) publish the SEDs of 65 local LIRGSs and ULIRGs. Our final sample is total of 38 galaxies based on the following filtering: 1)Exclude galaxies that lack both FUV and NUV: 56 galaxies left 2)Exclude galaxies that lack MIPS70: 56 galaxies left 3)Exclude galaxies that lack MIPS160: 45 galaxies left 4)Exclude galaxies that have $EQW_{6.2}$ <0.27 μm (Stierwalt et al., 2014) to remove those with AGN indicators): 38 galaxies left.

These galaxies have consistent aperture photometry to make sure the bolometric flux in each band is coming from the same exact region. In the merger systems where two galaxies are visible in the aperture, the aperture contains both galaxies and it is extended such that the outer part of the system(where the cold dust is present) is contained in the aperture.

For GOALS sample, we take the values of $L_{\rm IR}$ reported in U et al. (2012) where they derive it from the following equation:

$$\begin{aligned} F_{\rm IR} &= 1.8 \times 10^{-14} \\ &\times (13.45 f_{12} + 5.16 f_{25} + 2.58 f_{60} + f_{100}) \quad [\mathrm{Wm}^{-2}] \end{aligned} \tag{4.2}$$

$$L[8 - 1000 \mu m] = 4\pi D_L^2 F_{\rm IR} \tag{4.3}$$

Here f_{12}, f_{25}, f_{60}, f_{100}, are the flux densities in Jy at 12, 25, 60, and 100 μm, respectively, and D_L is the luminosity distance. This definition of L_{IR} refers to the luminosity emitted in the wavelength range 8–1000 μm.

We note that in some of the merger systems of the GOALS sample, the two galaxies have different colors but the reported flux is their combined flux in a given photometric band. Such composite systems are not naturally included in the SED library from the SAM, but since part of the motivation for this study is to apply the results to high redshifts, we have decided to include composite systems in this study, because it will often be the case at high redshift that both components of an early-stage merger are treated as one object.

4.3 Semi-analytic model and dust attenuation model

SAMs have been successful in reproducing the observed UV-NIR luminosity function (LF) of galaxies, UV-NIR number counts, and trends in many galaxy physical properties across different redshifts (Somerville et al., 2008c, 2012; Lu et al., 2014b). The dust parameters that Somerville et al. (2012) adopted were chosen to match observational constraints on the average $\log L_{IR}/L_{UV}$ versus bolometric luminosity and metallicity for nearby galaxies (Buat et al., 2007; Cortese et al., 2006a). The ability of the Somerville et al. (2012) model to simultaneously match the local luminosity func-

tions from the rest UV through NIR, as well as the $z \sim 0$ total IR LF, demonstrates that *on average* the energy balance (fraction of starlight absorbed and re-emitted by dust) in the model galaxy population is realistic, at least at low redshift. However, these models were not designed to necessarily provide a good representation of the SEDs of extremely dusty galaxies such as LIRGs and ULIRGs, and their ability to reproduce these populations at low-z has not been investigated before. This is the focus of this study.

The details of the SAM utilized in this work are presented in Somerville et al. (2008c) and Somerville et al. (2012), and briefly summarized here:

4.3.1 SAM Basics

The backbone of the SAM is comprised of dark matter halo merger trees which we construct using the Extended Press-Schechter based method described in Somerville et al. (2008c). Our SAM results are nearly indistinguishable when we run the models on merger trees extracted from numerical N-body simulations (see e.g. Porter et al., 2014). The models track the accretion of gas from the intergalactic medium, based on the cosmological halo mass accretion histories, and the cooling of hot halo gas into galaxies based on a simple cooling flow model. Gas that has cooled is assumed to form a rotationally supported disk, and the disk size is estimated based on angular momentum conservation. Cold gas in disks is converted into stars using an empirical Kennicutt-Schmidt relation, and stars and supernovae are assumed to drive winds

that can eject some of the cold ISM from the galaxy. Mergers lead to a short, enhanced mode of star formation (starburst mode) and to the formation of a spheroidal component. Mergers also feed gas into the galactic nucleus, fueling the growth of a central supermassive black hole. Accreting black holes can drive winds that eject cold gas from the galaxy, and may also produce radio jets that keep the halo gas hot and suppress cooling. Chemical evolution is tracked using the instantaneous recycling approximation with a fixed yield.

The resulting star formation and chemical enrichment histories are convolved with the stellar population synthesis models of Bruzual & Charlot (2003), adopting a Chabrier IMF, to generate the unattenuated stellar SED.

4.3.2 Modeling dust attenuation

Our starting point for the present work is the dust treatment described in detail in S12, which we briefly summarize here. As suggested by Charlot & Fall (2000b), the dust model includes attenuation by two components. The first component is due to the diffuse dust in the interstellar medium of the disc and the second component is associated with the dust in the dense birth clouds surrounding young star forming regions. The V-band, face-on optical depth of the diffuse dust is given by

$$\tau_{V,0} = \tau_{dust,0} Z_{cold} \left(\frac{< N_H >}{2.1 \times 10^{21} \mathrm{atoms\,cm^{-2}}}\right) \tag{4.4}$$

where the mean Hydrogen column density is given by

$$< N_H >= \frac{M_{cold}}{1.4 m_p \pi r_{gas}^2} \text{atoms cm}^{-2} \tag{4.5}$$

$\tau_{\rm dust,0}$ is a free parameter, $Z_{\rm cold}$ is the metallicity of the cold gas, $M_{\rm cold}$ is the mass of the cold gas in the disc, and $r_{\rm gas}$ is the radius of the cold gas disc, which is assumed to be a fixed multiple of the stellar scale length and here we assume the gas scale length is equal to stellar disk scale length (De Lucia & Blaizot, 2007).

To compute the attenuation we assign a random inclination to each galaxy and use a standard slab model; i.e. the extinction in the V-band for a galaxy with inclination i is given by:

$$A_V = -2.5 \log_{10} \left[\frac{1 - \exp\left(\frac{-\tau_{V,0}}{\cos(i)}\right)}{\frac{\tau_{V,0}}{\cos(i)}} \right] \quad . \tag{4.6}$$

As we will discuss in the text, we also implemented a version of the mock library with the 'screen geometry' of dust with respect to the stars as this model would be a better match for starburst and merger samples. The attenuation in this case is computed by $A_V = 1.086 \times \tau_{V,0}$. Additionally, stars younger than $t_{\rm BC}$ (lifetime of the birth clouds) years, are enshrouded in a cloud of dust with optical depth $\tau_{\rm BC,V} = \mu_{\rm BC}\, \tau_{V,0}$, which is effective absorption depth in the birth clouds. We treat $t_{\rm BC}$ and $\mu_{\rm BC}$ as free parameters. Finally, to extend the extinction estimate to other wavebands, we assume a starburst attenuation curve (Calzetti, 1997, 2001b) for the diffuse dust component and a power-law extinction curve $A_\lambda \propto (\lambda/5500\text{Å})^n$, with $n = 0.7$, for the

birth clouds (Charlot & Fall, 2000b). This approach has been shown to provide a good representation, on average, of the attenuation curves predicted by numerical radiative transfer simulations (Fontanot et al., 2009b). Moreover, our model predictions are quite insensitive to the details of the assumed attenuation curve for the diffuse dust (e.g., Calzetti vs. a Galactic or a CF00-like power law).

There are three free parameters that control the dust attenuation in this model: the normalization of the face-on V-band optical depth $\tau_{\rm dust,0}$, the opacity of the birth clouds relative to the cirrus component $\mu_{\rm BC}$, and the time that newly born stars spend enshrouded in their birth clouds, $t_{\rm BC}$. Following S12, we adopt a default value of $\tau_{\rm dust,0} = 0.2$. The value of $\tau_{\rm dust,0}$ was obtained by matching the normalization of the observed relationship between $L_{\rm dust}/L_{\rm UV}$ vs. bolometric luminosity $L_{\rm bol}$ for nearby galaxies studied by Buat et al. (2007), where $L_{\rm dust}$ is the total luminosity absorbed by dust and re-emitted in the mid- to far-IR and $L_{\rm UV}$ is the luminosity in the far-UV (~ 1500 Å). With this normalization, the model also reproduces the observed relation between $L_{\rm dust}/L_{\rm UV}$ and gas phase metallicity of Cortese et al. (2006a).

The birth cloud parameters $\mu_{\rm BC}$ and $t_{\rm BC}$ mainly control the attenuation of UV light relative to longer wavelengths. Somerville et al. (2012) show that in the local Universe ($z = 0$), the g through K-band luminosity functions are insensitive to the birth cloud parameters, while the FUV through u-bands are quite dependent on them. S12 adjusted the parameters to match the $z = 0$ FUV and NUV observed luminosity functions, finding good agreement with $\mu_{\rm BC} = 4.9$ and $t_{\rm BC} = 2 \times 10^7$ yr, which we also

adopt as a starting point. However, S12 found that it was not possible to reproduce the observed rest-frame UV and optical luminosity functions at high redshift with fixed values of these parameters. Other studies (e.g. Lo Faro et al., 2009; Guo & White, 2009) have reached similar conclusions.

Somerville et al. (2012) can reproduce the observed UV LF at high redshifts with evolving the parameters of the CF00 model and (Kriek & Conroy, 2013a) has shown that CF00 model is able to reproduce the attenuation curves well out to redshifts $z < 2$ for all types of SEDs.

Using the formalism presented above, we can compute the total fraction of the energy emitted by stars that is absorbed by dust, over all wavelengths, for each galaxy in our simulation. We assume that all of this absorbed energy is re-radiated in the IR (we neglect scattering), and thereby compute the total IR luminosity ($L_{\rm IR}$) of each mock galaxy.

We make use of dust emission templates of Rieke et al. (2009b), hereafter R09, to determine the SED of the dust emission, based on the hypothesis that the shape of the dust SED is well-correlated with $L_{\rm IR}$.

4.4 SED fitting

We construct PDFs of the predicted L_{IR} based on the likelihood from the UV/optical SED fitting. The log-likelihood of the j th model, denoted as M_j, given the spectral

energy distribution of a galaxy can be written as

$$\ln P(M_j|\{O_i\}) = -\frac{1}{2}\sum_i \left(\frac{O_i - w_j M_{j,i}}{\sigma_i}\right)^2 , \tag{4.7}$$

where O_i and $M_{j,i}$ are the flux in the i th photometric band of the pseudo-galaxy and the j th model, respectively. σ_i is the uncertainty in O_i corresponding to the adopted signal-to-noise ratio, and

$$w_j = \left(\sum_i \frac{O_i M_{j,i}}{\sigma_i^2}\right)\left[\sum_i \left(\frac{M_{j,i}}{\sigma_i}\right)^2\right]^{-1} \tag{4.8}$$

is the model scaling factor that maximizes $P(M_j|\{O_i\})$. We do not select galaxies in the mock library to match the observed galaxies in a given criteria such as mass or H band magnitude. We do our SED fitting agains the whole library. Doing this we are assuming self-similarity of the galaxy in the library in that a small galaxy with some property could be scaled up to a larger galaxy. This is not the case in the real universe, however, when doing SED fitting we prefer to include this assumption instead of selection a specific subsample from the mock for each single galaxy according to mass or other parameters. The advantage of our approach would be less confusion in interpreting the result and we discuss this in detail in section 4.5.3.

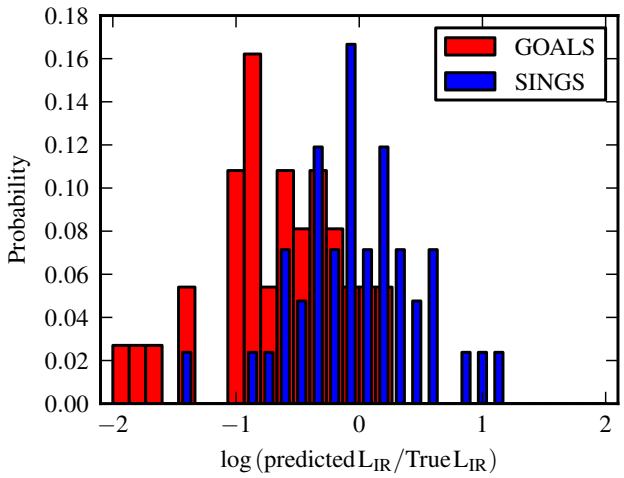

Figure 4.2: Predicting the infrared luminosity for both SINGS and GOALS samples with SED fitting in the UV-NIR range against a mock library with $\tau_{V,0} = 0.2$ with slab geometry. We find that our predicted IR luminosities are within $\pm$ 1 dex of the true infrared luminosity 95% of the time for SIGNS sample and 75% of the time for GOALS sample.

4.5 Results

Our library consists of a SAM output at redshift $z = 0$, distributed uniformly in logarithm of halo mass ($10.5 < \log M_h(M_\odot) < 13$). Figures 4.2 illustrate the ability to predict L_{IR} based on SED fitting using the bands in FUV-H range (0.15-1.6 μm).

Figures 4.2 shows that there is a negative bias when predicting the IR luminosity of the GOALS sample. The nature of the under prediction for the GOALS sample is investigated next.

4.5.1 color-color diagram

Color-color diagrams using three colors to place galaxies into different categories based on their star formation activity is a common practice in astronomy and widely used to distinguish between different class of objects. The often used combination of U, V and J color has been successful to distinguish between dead and dusty galaxies. We don't have the U data for the GOALS sample, therefore we use a proxy for the color-color diagram by using NUV instead of the U band. In figure 4.3 we plot the NUV-V-J diagram of the galaxies in our mock library (dots) and that of the GOALS sample(triangles). The points are color coded according to their ratio of IR luminosity over the H band luminosity. if we take the IR luminosity as a proxy for the star formation rate and the H band luminosity for the mass of the galaxies, then our color scheme could be interpreted as a proxy for the specific star formation rate. If the triangle is pointing up, it means the IR luminosity for that galaxy is over predicted and if it is pointing down, under predicted. The magnitude of the over or under prediction is indicated by the size of the triangles.

In the upper-left panel of Figure 4.3, the GOALS sample is shown with the library constructed based on 'slab' geometry with $\tau_{V,0} = 0.2$. In the upper panel, the result is shown when the library is constructed based on 'screen' geometry with $\tau_{V,0} = 0.2$. In the lower panel, the result is shown for the case of library with $\tau_{V,0} = 1.$ and 'screen' geometry and the case for $\tau_{V,0} = 5$ and screen geometry is shown in the lower-right panel. There are three points immediately clear from this plot:

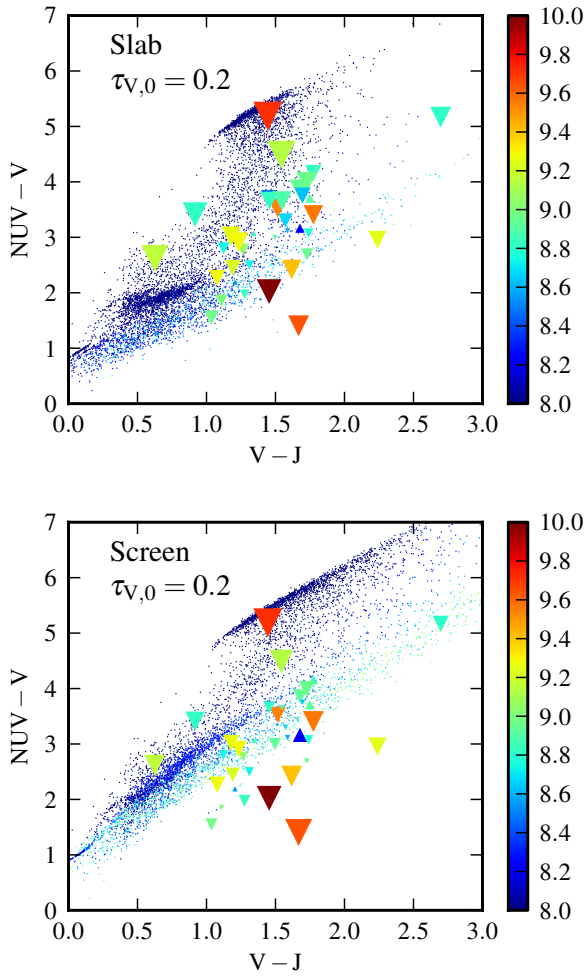

Figure 4.3: The (NUV-V-J) color-color diagram of the GOALS sample (triangles) and the galaxies in our mock library (dots). The color coding is based on the log L_{IR}/L_H to be a proxy for the specific star formation rate. If a triangle is pointing down, it means that the IR luminosity for that galaxy is under predicted and if it is pointing up, it is over predicted. The magnitude of the under or over prediction is shown by the size of the triangles. We show the result for four different libraries given the type of dust geometry applied and the magnitude of $\tau_{V,0}$. The slab geometry with $\tau_{V,0} = 0.2$ leads to a bias of -0.6 dex overall. The bias becomes negligible when we chose the library with screen geometry and $\tau_{V,0} = 5$.

1) The GOALS sample scatter in regions of the color-color- diagram that are not well populated with the mock galaxies. We have investigated whether there are

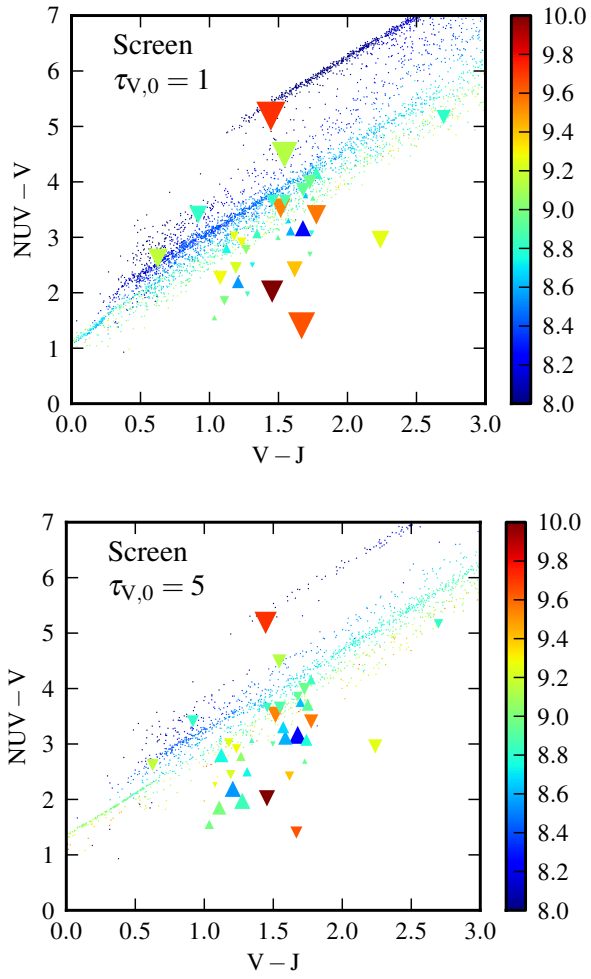

Figure 4.4: The same as Figure above, but for more extreme attenuation at V band.

possible emission lines that could be causing that, but we did not find a plausible theory for this. Those galaxies that are in far from the locus of the galaxies in the color-color diagram, are located far from the locus of the galaxies in other color-color diagrams as well.

2) There are GOALS galaxies that lie in the quenched part of the color-color diagram and therefore not surprisingly their IR luminosity is under predicted even in

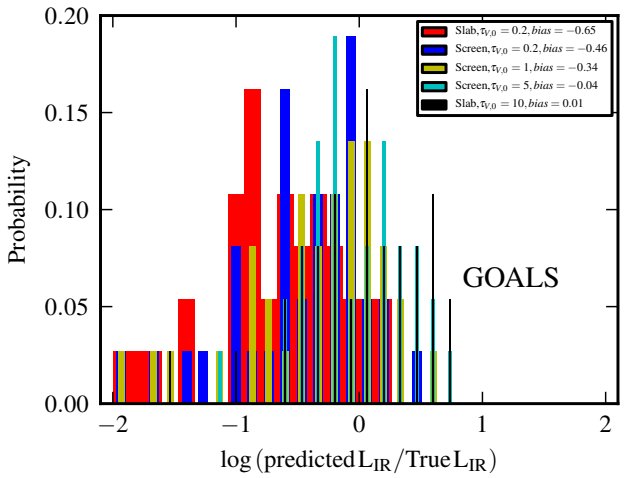

Figure 4.5: Shows how the choice of dust geometry and the amplitude of the extinction affects the outcome of the SED fitting for the GOALS sample. between two models with the same $\tau_{V,0}$, the one with screen geometry leads to lower bias compared with the slab model. As $\tau_{V,0}$ is increased, the magnitude of bias decreases such that continuous increase would eventually lead to over predicting the IR luminosity. The value of $\tau_{V,0}$ required to achieve zero bias in screen model is a factor of 2 less that what is required in slab model.

the dust model with screen mode and high τ_V value.

3) The bias is largely removed when the SED fitting is done against the dustiest library (screen mode and $\tau_V = 5.$) and the bias is most negative (under predicting the L_{IR}) in the dust model with slab geometry and $\tau_V = 0.2$.

4.5.2 L_{IR} and UV/optical slope

It is instructive to see the progress in the UV/optical SED of the mock library as a function L_{IR} . We show the trend with IR luminosity in Figure 4.6 for all the central (not satellites) galaxies in the mock library. There is no trend between the slope of the

median SEDs in the UV/optical with respect to the IR luminosity (although we would have a seen a trend with halo mass, as galaxies in more massive halos have redder slopes, either due to dust or quenching). The reason is that at a given L_{IR} there will be a mixture of star forming galaxies and quenched galaxies and the portion of each type contributing to each bin of L_{IR} varies. If we exclude the passive galaxies from the library we see a clear trend with the slope in the UV/optical and L_{IR} as shown in right panel of Figure 4.6. Over plotted are GOALS galaxies with L_{IR} in the range [11-11.3] in red and [11.6-11.8] in blue. The striking difference between the nature of the SEDs in mock library and GOALS sample is that local LIRGs become bluer as they become more infrared luminous which is contrary to the trend we observe in our mock library. The fact that bluer galaxies are dustier in the local LIRGs and the opposite holds for the galaxies in our mock library, explains part of the reason why we are under predicting the L_{IR} of the GOALS sample.

4.5.3 L_{IR} and H band luminosity

In the process of SED fitting as described in section 4.4, the using of the floating factor (w_j) has the inherent assumption that the galaxies are self-similar. In other words, if there is a galaxy in the mock library that matches that of the observed SED in the UV/optical, but with a normalization that is higher than the observed SED, the final predicted L_{IR} will be accordingly scaled down linearly. It is worth investigating if this is indeed the case both in the mock library and the observed

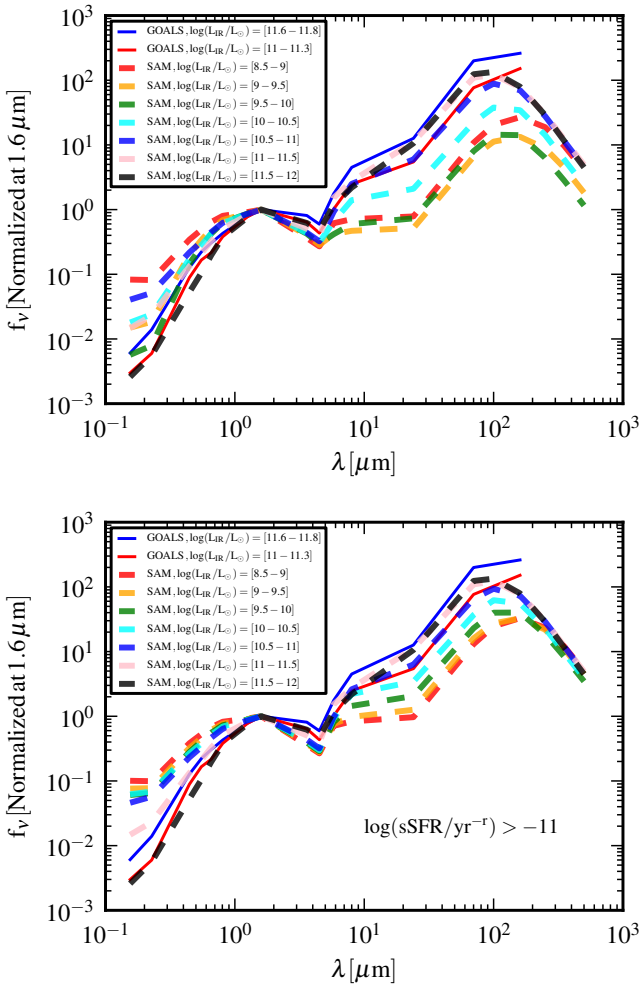

Figure 4.6: Left panel: Median of SEDs in the mock library for different bins in IR luminosity. There is no clear trend between the shape of the SED in the UV-optical range and L_{IR}. Right panel: Median of SEDs in the mock library for galaxies with $\log(sSFR/yr^{-1}) > -11$ for different bins in IR luminosity. A clear trend of SEDS becoming redder as they become more IR luminous is seen in the mock galaxies. The median SED of the GOALS sample galaxies with their $L_{IR}[L_{\odot}]$ in the range [11-11.3] and [11.6-11.8] is over plotted. Galaxies in the GOALS sample show to have *bluer* SED at higher L_{IR} unlike the trend in the mock library.

samples. We take the luminosity in H band as the proxy for the amplitude of the SEDs in UV/optical.

Figure 4.7 shows the ratio of the L_{IR}/L_H(Where L_H is H band luminosity) versus

the luminosity in H band. The GOALS sample is plotted as red squares, the mock library galaxies are shown in black, the SINGS sample is shown in orange. It is clear that SINGS sample don't show any correlation since they are a mixture of different types of galaxies. The GOALS sample show a *negative* correlation. It means that in GOALS sample, as the SEDs become more(less) luminous in H band luminosity, the L_{IR} decreases (increases) respectively, unlike the trend we see in our mock library, SINGS sample.

The impact of this would be to increase the dispersion in the predicted L_{IR} of the GOALS sample. If there is an SED in our mock library that matches that of a galaxy from the GOALS sample but the galaxy in the observed sample has higher H band luminosity, the SED fitting will boost the mock library SED to match the observed sample UV/optical SED and accordingly boosts the L_{IR} of the mock library SED and report it as the predicted L_{IR} . However, the assumption that higher H band luminosity is associated with higher L_{IR} is not satisfied in the GOALS sample and therefore in that case we are over predicting the L_{IR} . If the SED in the mock library is brighter in H band than the observed sample, applying the same logic leads to under prediction of the observed sample's L_{IR} . Both these effects will lead to increasing the dispersion in the predicted L_{IR} of the GOALS sample.

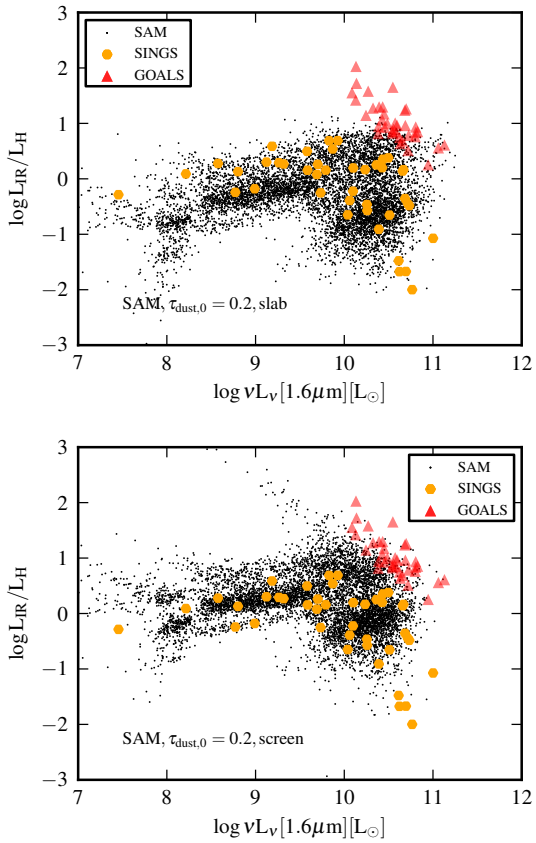

Figure 4.7: Shows the ratio of the L_{IR}/L_H(Where L_H is H band luminosity) versus the luminosity in H band. The GOALS sample is plotted as red squares, the mock library galaxies are shown in black dots and the SINGS sample is shown in orange hexagons. We are showing four different mock libraries, either slab or screen mode with different value for the $\tau_{V,0}$. Although the SINGS sample is scatted in the plane, the GOALS sample shows to have a strong negative correlation between the ratio of the IR luminosity over H band versus H band luminosity. This negative correlation stars to appear when the dust geometry is assumed to be in screen mode and becomes more strongly pronounced when the $\tau_{V,0}$ is increased.

4.6 Discussion

Similar analysis to what we have done in this paper has been carried out based on MAGPHYS library (da Cunha et al., 2008). da Cunha et al. (2008) have carried out an analysis on 54 GOODS-Herschel sample of galaxies with median redshift of

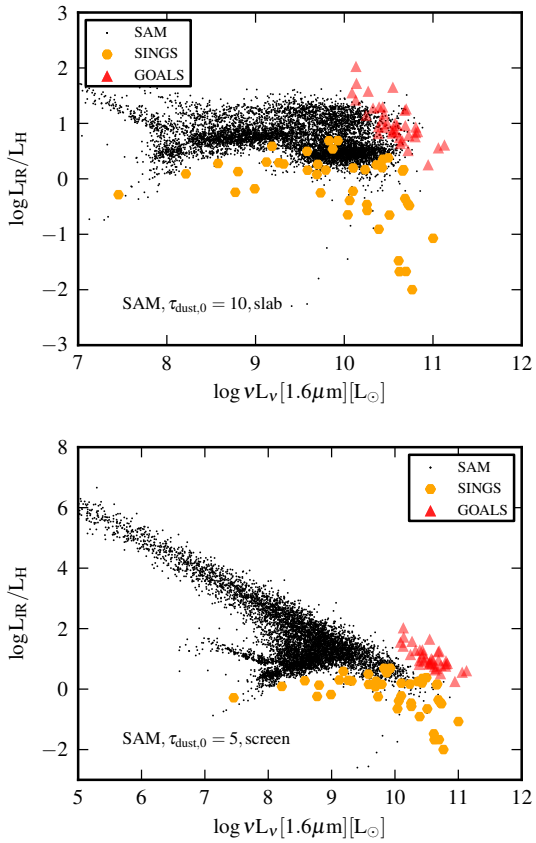

Figure 4.8: Same as in Figure 4.7, but for more extreme cases of dust attenuation.

1. They show that estimates of FIR luminosity based on using only bands from U to K in their SED fitting is biased low compared with the result based on including the FIR bands in the SED fitting and this bias is more pronounced for galaxies with higher IR luminosities. It needs further analysis to understand the nature of the bias in the MAGPHYS library.

Individual FIR measurements of high redshift galaxies are subject to confusion noise (Condon, 1974) and often stacking results are reported as the mean luminosity of galaxies belonging to a given class at a given redshift (Magdis et al., 2010a; Magnelli

et al., 2013a). A novel technique has been proposed by Safarzadeh et al. (2015a) to overcome the confusion noise in the *Herschel* images and therefore to measure individual galaxies' flux at FIR. This technique is Bayesian in nature and requires weak priors on the flux of the emitting galaxies at the observed FIR pass band. The weak priors come from the HST observations at rest-frame FUV-NIR part of the galaxies' SEDs which are not affected by confusion noise with reliable measurements available through deep extragalactic surveys such as CANDELS (Koekemoer et al., 2011; Grogin et al., 2011). A crucial step in the processes of de-confusing the FIR images would be to have a library of mock galaxies representative of the state of the galaxies at high redshift.

We conclude that the nature of UV/optical SEDs of GOALS sample are different from the SEDs in the mock library in three different ways:

- Local LIRGs become bluer in their UV/optical SED as they become more IR luminous. This is in agreement with the findings of (Casey et al., 2014b) that shows dusty galaxies with SFR more than 50 $M_{\odot}$ per year are bluer too. The reason being existence of a population of O and B stars that are not-enshrouded in dust. In other words, stellar population of the same age can have very different $\tau's$. However, this behavior is in contrast with the nature of the SEDs in SAM where they become redder in UV/optical as they become more IR luminous.

  This should come as no surprise since there is no mechanism in the current

dust treatment to leave a fraction of the young stars un attenuated such that SEDs could be both IR and FUV luminous at the same time. Libraries based on dusty radiative transfers applied to hydrodynamical simulations of galaxies formation should not have this issue in principle and future work on this will be presented soon in a separate paper.

- Some of the local LIRGs lie in the quenched region of the color-color diagram despite their high IR luminosity. This could be due to the fact that our local LIRGs are mostly mergers of two entirely different galaxies and the UV/optical SED of the one is dominating the other ones' while the FIR SED is originating from the companion galaxy mostly. One can account for this by changing the SED fitting procedure such that the model SEDs are combination of two distinct SEDs weighted by the stellar mass of the galaxies. We have not tried this idea in the current paper but is our immediate future goal to expand this to high redshift observation where this problem is more severe.

- The amplitude of the H band luminosity in local LIRGs decrease (increase) as their L_{IR} increase(decrease) respectively. This is contrast with the trends we see in our mock library where other than in the passive galaxies, there is a positive correlation between the amplitude of the H band luminosity and IR luminosity. This suggests that the assumption of the self similarity incorporated in the SED fittings *does not hold* when studying the local LIRGs sample. Part

of the dispersion in the predicted L_{IR} in both SINGS and GOALS sample could be explained by the fact that self similarity is not the correction assumption to make about these galaxies (and definitely the case for local LIRGs).

It is clear that CF00 model in its basic form can not reproduce the trend we see in local LIRGs in that they become bluer in their FUV/optical SED as they become more IR luminous. They way out would be to let a fraction of star formation not be enshrouded by dust to mimic the possibility that some of the O and B stars have disrupted their birth clouds on timescales much shorter than 2×10^7 years. If we decrease the t_{BC} in the SAM from 2×10^7 years to 2×10^6 years we still can not reproduce the trend of bluer and dustier because then the IR luminosities will drop in general. The solution would be to let only a fraction of the OB stars to be unattenuated by dust and the rest of the newly born stars to be left enshrouded in dust. Also we have to model it such that fraction of the OB stars that are not attenuated by dust to increase as the IR luminosity goes up.

In order to capture the observed trend in the GOALS sample that the amplitude of the optical SED anti-correlates with IR luminosity, in the sense that more IR luminous ones to be less bright in H band, would require either a different stellar population to be present in the galaxies when we are in the IR luminous regime in the SAM or a different attenuation curve. However, this trend is not observed in the normal star forming galaxies.

Whether these results based on the low redshift samples are applicable to high

redshift galaxies is an open question where we will be addressing in forthcoming paper.

4.7 Summary

As illustrated in Figure 4.2, the implementation of the modified CF00 dust treatment in the SAM can predict infrared luminosities to within ±1 dex of for normal star forming galaxies (with 95% probability) and that of the luminous infrared galaxies (with 75% probability). Although we are often within ± 1dex of the true IR luminosity in our predictions, we have demonstrated that we systematically under predict the IR luminosity of the local LIRGs. There are two reasons to account for this: 1) Some of the GOALS sample galaxies are red similar to the quenched galaxies as evident from where the lie in the color-color diagram. For these galaxies there is not much hope in the SED fitting to recover their L_{IR} correctly. 2) Local LIRGs become bluer as their L_{IR} increases in contrast to the galaxies in the mock library that become redder as they become IR bright galaxies.

Moreover, there is an anti-correlation between the amplitude of the SEDs in H band and the IR luminosity for the local LIRGs and the opposite to hold for the mock galaxies modeled with slab geometry. However, if dust model implemented is screen mode with high V band attenuation, we would get a similar trend (as shown in lower-right panel of Figure 6) to the GOALS sample. This indicates very high

obscuration in screen mode can potentially explain the trend we see in the GOALs sample.

Our examination of the low-redshift reference samples in this paper is in part motivated by our interest in predicting the FIR SEDs of high-redshift galaxies, to use as priors to address the problem of source confusion.

Chapter 5

IRX-β: Insights from simulations

5.1 Introduction

Dust plays a key role in many areas of astrophysics. In galaxies, it obscures emission from stars and active galactic nuclei (AGN), thereby making it more difficult to infer the properties of these objects, such as stellar ages. Various approaches are used to correct for the effects of dust attenuation; one popular approach is to use the so-called 'IRX-β' relation. Here, β refers to the ultraviolet (UV) continuum slope, which is defined by assuming that the UV regime of galaxy spectral energy distributions (SEDs) can be described by a power law, $f_\lambda \propto \lambda^\beta$ (e.g., Calzetti et al., 1994a; Meurer et al., 1999a). Dust reddening and older stellar populations both cause the UV continuum to be steeper and thus β to be more positive. IRX denotes the 'infrared excess' and is defined as IRX$\equiv L_{\rm IR}/L_{\rm FUV}$, where $L_{\rm IR}$ and $L_{\rm FUV}$ are the total

infrared (IR) and far-UV luminosities, respectively. Meurer et al. (1999a, hereafter M99) demonstrated that local starburst galaxies exhibit a relatively tight, monotonic relation between IRX and β.

Recent re-calibrations of the IRX $-$ β relation prefer lower values of IRX for the same UV slope compared with the M99 relation (Overzier et al., 2011; Takeuchi et al., 2012; Casey et al., 2014c; Álvarez-Márquez et al., 2016). It has been found that massive galaxies at high redshifts have similar IRX values as their low-redshift counterparts but with bluer UV slopes (Álvarez-Márquez et al., 2016), which implies that using the locally calibrated IRX-β relation would cause one to underestimate the SFRs of high-mass LBGs. Therefore, we should reconsider the similarity of the Lyman break galaxies (LBGs; Steidel et al., 1996b) at $z \sim 2$ to local starburst galaxies based on high-redshift LBGs falling onto the M99 relation (Reddy et al., 2012b).

Due to the sensitivity and confusion limits (Safarzadeh et al., 2015b) of current IR surveys, for many UV-selected galaxies, the IR luminosity is unknown; thus, inferring the dust obscuration from the UV slope β is highly desirable if one wishes to constrain the total star formation history of the Universe (e.g., Bouwens et al., 2009, 2012, 2014; Dunlop et al., 2012; Finkelstein et al., 2012). For galaxies for which M99 relation holds, the observed slope can in principle be used to infer the amount of UV light that has been obscured by dust, and thus one can obtain the intrinsic UV flux and total star formation rate (SFR) from UV observations alone.

If observations and/or simulations indicate that there is significant dispersion in

IRX for a fixed value of β, then it would be useful to determine whether there are other UV-optical observable properties of a galaxy that could be used to predict its location in the IRX $-$ β plane. It is known that (ultra-)luminous infrared galaxies [(U)LIRGs], alternatively referred to as dusty star-forming galaxies (DSFGs), do not obey any well-defined IRX-β relation (Goldader et al., 2002; Bell et al., 2002; Howell et al., 2010b; Casey et al., 2014c). Furthermore, recent studies have revealed more scatter than the original M99 work, even if (U)LIRGs are excluded. Assuming an exponentially declining star formation history (SFH), Kong et al. (2004) suggest that the dispersion in IRX-β can be explained by the ratio of the recent SFR to the SFR averaged over a longer timescale (a proxy for the SFH). Kong et al. (2004) show that the distance of galaxies from the M99 relation exhibits no correlation with the dust-sensitive H_α/H_β ratio (i.e., the Balmer decrement), thus suggesting that dust attenuation is not responsible for the dispersion in the relation. In contrast, Cortese et al. (2006b) conclude that different dust geometries can explain the observed dispersion, but this conclusion may be affected by calibration issues (Casey et al., 2014c). We discuss our results regarding the source of dispersion in Section 5.5.

The goal of this paper is to understand how galaxies might be *expected* to evolve in the IRX $-$ β plane given reasonable geometries, SFHs, merger parameters, etc. and accounting for viewing angle-related effects. We wish to address questions such as the following: how much of the dispersion in β at fixed IRX is due to viewing angle? How much of the dispersion is due to physical differences such as star formation histories

and dust geometries? How do galaxy mergers evolve in the IRX $-$ β plane? Are high-redshift DSFGs predominantly merger systems or isolated disks?

To address the above questions, we analyze a set of 51 idealized (i.e., non-cosmological) galaxy simulations, including both mergers and isolated disks, that are intended to be representative of both low-redshift ($z \sim 0$) and high-redshift ($z \sim 2-3$) galaxies. In post-processing, we perform dust radiative transfer on the simulated galaxies at various times to predict their UV–mm SEDs. This enables us to *forward-model* the positions of the simulated galaxies in the IRX-β plane. These or similar simulations have been shown to be in good agreement with the SEDs/colors of diverse classes of real galaxies, such as local normal star-forming galaxies (Jonsson et al., 2010), (U)LIRGs (Younger et al., 2009a; Jonsson et al., 2010; Lanz et al., 2014), high-redshift DSFGs (Narayanan et al. 2010a; Hayward et al. 2011a, 2012), obscured AGN (Snyder et al. 2013) and post-starburst galaxies (Snyder et al., 2011). We analyzed the same set of simulations in Safarzadeh et al. (2016), where we showed that the dispersion in the FIR SEDs of our simulated galaxies is determined primarily by the luminosity absorbed by dust and dust mass (i.e., dust geometry is subdominant).

The remainder of this paper is organized as follows: in Section 5.2, we summarize the details of the simulated galaxy SED dataset used in this work. Section 5.3 discusses how the SFR, observed and intrinsic UV continuum slopes, and IRX values of some representative isolated disk and galaxy merger simulations evolve in the IRX-β plane. Section 5.4 demonstrates how the results depend on the dust model assumed

in the radiative transfer calculations. In Section 5.5, we investigate the dispersion in the IRX-β relation. Section 5.6 discusses the location of DSFGs in the IRX-β plane. In Section 5.7, we compare our results with previous work. Section 5.8 presents some implications for interpreting observations. Section 5.9 discusses the limitations of this work and provides suggestions for future work, and Section 5.10 summarizes our conclusions.

5.2 Simulated galaxy SED dataset

Our low-redshift simulation dataset was presented in Lanz et al. (2014, hereafter L14). The four progenitor disk galaxies span a stellar (baryonic) mass range of $6 \times 10^8 - 4 \times 10^{10}\ M_\odot (10^9 - 5 \times 10^{10} M_\odot)$, and their properties were selected to represent typical star-forming galaxies in the local universe (Cox et al., 2008). Each of the four progenitors – together with the 10 different possible combinations of them as merger systems – were simulated for a single non-'special' orbital configuration for multiple gigayears (see L14 for details). The total dataset contains ~ 6000 SEDs.

The details of the second set of SEDs of simulated isolated disk and merging galaxies are presented in Hayward et al. (2013b, hereafter H13). For this dataset, the structural properties of the progenitor disk galaxies were scaled to $z = 3$ following Robertson et al. (2006), with the initial gas fractions of the disks (0.6-0.8) being significantly larger than those of the $z \sim 0$ simulations. Because the original purpose

of this suite of simulations was to model $z \sim 2-3$ DSFGs, the progenitor disks span a relatively narrow baryonic mass range of $\sim 1-4\times10^{11}M_{\odot}$, but a variety of merger orbits and mass ratios are included. This dataset contains 37 hydrodynamical simulations, from which $\sim 46,000$ SEDs were calculated.

The full methodology is described in the aforementioned works and references therein, so we will only summarize it here. First, idealized isolated (i.e., non-cosmological) galaxy models were created following the method described in Springel et al. (2005). Each initial disk galaxy is composed of a dark matter halo, stellar and gaseous disks, and a supermassive black hole (SMBH); for the $z \sim 0$ simulations only, a stellar bulge is also included. Then, the isolated galaxies and binary mergers of these galaxies were simulated using a heavily modified version of the GADGET2 N-body/smoothed-particle hydrodynamics (SPH) code (Springel, 2005).[1]

The simulations include the effects of gravity, hydrodynamical interactions, and radiative heating and cooling.[2] Star formation and stellar feedback are incorporated via the two-phase sub-resolution interstellar medium (ISM) model of Springel & Hernquist (2003), and BH accretion and AGN feedback are treated following Springel et al. (2005). Each gas particle is enriched with metals according to its associated SFR, assuming a yield of 0.02. Instantaneous recycling is assumed.

[1]Hayward et al. (2014b) demonstrated that the results of such simulations are insensitive to the inaccuracies inherent in the traditional density-entropy formulation of SPH, so the numerical scheme employed does not represent a significant source of error.

[2]The gravitational softening lengths for baryonic particles are $\sim 100-150$ pc, and those of the dark matter particles are $2-4$ times greater (see H13 and L14 for details). We have confirmed that our results are converged with respect to the resolution of the hydrodynamical simulations (see also Martínez-Galarza et al. 2016).

The UV-mm SEDs of the simulated galaxies are forward-modeled by post-processing the outputs of the 3-D hydrodynamical simulations at various times with the dust radiative transfer code SUNRISE (Jonsson, 2006; Jonsson et al., 2010). For a given snapshot, the SUNRISE calculation proceeds as follows: the stellar and BH particles in the GADGET2 simulation, which are the sources of radiation, are assigned source SEDs according to their properties (age and metallicity for the star particles and luminosity for the BH particles). The metal distribution from the simulation is projected onto an octree grid in order to calculate the dust optical depths. We use a fixed dust-to-metal ratio of 0.4 (e.g., Dwek, 1998b; James et al., 2002). The Milky Way (MW) $R_V = 3.1$ dust model of Draine & Li (2007) is used except for the runs with Small Magellanic Cloud (SMC)-type dust described in Section 5.4. After the source and dust properties are specified, radiation transfer is performed using the Monte Carlo method to calculate the effects of dust absorption, scattering, and re-emission. For each snapshot, this process yields spatially resolved UV–mm SEDs of the simulated galaxy/merger viewed from 7 viewing angles.

We tested whether varying multiple potentially important assumptions in the radiative transfer calculations affected our results. Of the various parameters and assumptions investigated, we found that only the assumed dust composition had a significant effect on our results (i.e., the evolution in the IRX-β plane); this is discussed in detail in Section 5.4. Changing other potentially relevant assumptions typically caused the resulting β value to differ by ~ 0.2 or less, and IRX was generally

negligibly affected.

5.3 Evolution of the simulated galaxies in the IRX-β plane

We will now discuss how the simulated galaxies evolve in the IRX-β plane. We present the results for two (one $z \sim 0$ and one $z \sim 2-3$) representative isolated disk galaxy simulations in Section 5.3.1, and two representative merger simulations are discussed in Section 5.3.2.

5.3.1 Isolated disks

Our simulation suite contains 8 isolated disk simulations, 4 of which are representative of $z \sim 0$ galaxies and 4 of which represent $z \sim 2-3$ galaxies. The details of these simulations are presented in L14 and H13, respectively.

The top panel Figure 5.1 shows the time evolution of both the attenuated and intrinsic UV slopes, IRX and log SFR for one of the simulated $z \sim 0$ isolated disks, the M3 simulation of L14.[3] After an initial transient owing to the initial conditions

[3]We measure the observed (intrinsic) UV continuum slope from the dust-attenuated (unattenuated) SED by least-squares fitting a functional form of $f_\lambda \propto \lambda^\beta$ to the SED in the wavelength range of 1400 Å $< \lambda <$ 2300 Å. We also measured the UV slope by convolving the SEDs with the GALEX FUV and NUV filter response curves, and we obtained slopes indistinguishable from those obtained by fitting the SEDs in the wavelength range of $1400-2300$ Å. The FUV luminosity is measured from the attenuated SEDs at $\lambda = 1600$ Å, i.e., $L_{FUV} = \lambda L_\lambda$ at $\lambda = 1600$ Å. The FIR luminosity ($L_{\rm FIR}$) is defined by integrating the SED from 8 to 1000 μm. We then calculate $IRX \equiv L_{FIR}/L_{FUV}$.

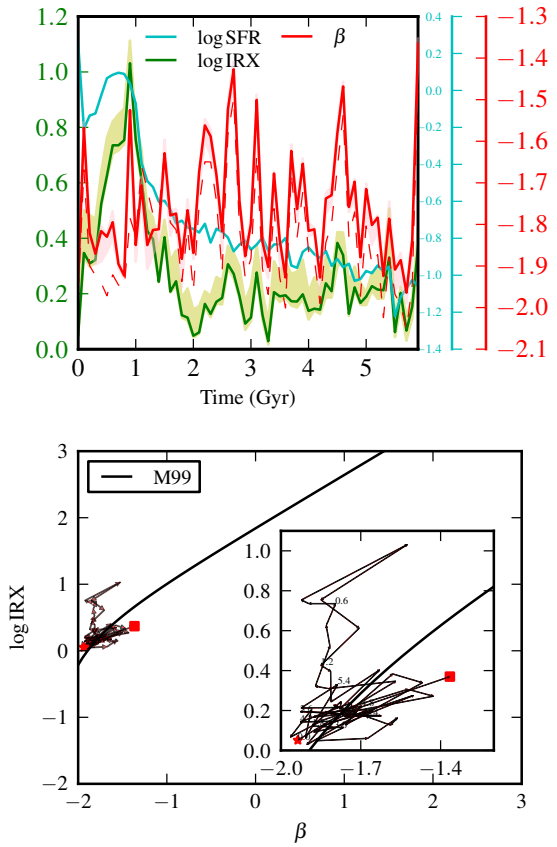

Figure 5.1: Results for a simulated $z \sim 0$ isolated disk galaxy, the M3 simulation of L14. *Top*: The time evolution of log (SFR/M$_\odot$ yr^{-1}) (cyan), the observed and intrinsic (i.e., unattenuated) UV slopes β (thick-solid and thin-dashed red lines, respectively), and log IRX $\equiv \log(L_{\rm FIR}/L_{\rm UV})$ (green line). The observed β and IRX values depend on viewing angle; the lines correspond to the average taken over the 7 viewing angles, and the shaded pink and yellow regions show the dispersion in the observed β and IRX values, respectively, over the different viewing angles (see text for details). The log IRX axis labels are provided on the lefthand side of the figure, and the β and log SFR values are provided on the right in red and cyan text, respectively. *Bottom*: The evolution of the simulated galaxy in the IRX-β plane. This figure utilizes axis ranges that will be used for all IRX-β plots in this work (see text for details); consequently, the data are concentrated in a small section of the plot. The inset shows a zoomed-in view of this region. The solid line shows the M99 relation. The red star indicates the initial time snapshot of the simulation, and the red square marks the final snapshot. The arrows connect individual snapshots (which are separated by 100 Myr), and the time elapsed in Gyr is labeled for a small subset of the snapshots. At all times, this simulated disk galaxy lies near the M99 relation; the 'spur' above the relation corresponds to early in the simulation (first $\sim$ 1 Gyr), when the galaxy is the most gas-rich, highly star-forming, and dust-obscured.

being slightly out of equilibrium, the SFR (the cyan line in the top panel) smoothly declines as the gas is depleted.[4] The UV slope measured from the attenuated SEDs is shown in red. It varies rapidly on a timescale of ~ 100 Myr, ranging from ~ -2 to ~ -1.5, and there seems to be no long-timescale trend. The pink shaded region shows the dispersion due to the viewing angle, which is calculated as the difference between the 84th and 16th percentiles of the distribution divided by two (for a Gaussian distribution, this is equivalent to 1σ). For this particular simulation, the dispersion due to viewing angle is clearly less than that due to the time evolution of the galaxy. The UV continuum slope measured from the intrinsic (i.e., unattenuated) SEDs is shown with a thinner red line, which is below the thicker red line at all times. Both of these lines are plotted on the same scale, and the values can be read from the red axis on the righthand side of the figure. The differences between the observed and intrinsic UV slopes are modest, which suggests that dust attenuation does not significantly alter this simulated galaxy's UV slope. The measured IRX is indicated by the green line, and the dispersion with viewing angle is denoted by the yellow shaded region. The IRX axis values are specified by the green numbers on the *left* side of the figure. The IRX value is high (~ 10) in the early stages of the simulation, when the galaxy is still gas-rich. As the gas reservoir is depleted and dust is locked into stars, thus decreasing the amount of dust attenuation, IRX becomes of order unity.

The bottom panel of Figure 5.1 shows the time evolution of this simulation in the

[4]Because these are idealized, non-cosmological simulations, no cosmological gas accretion is included.

$IRX - \beta$ plane. The main figure uses the axis ranges that will be used in all IRX-β plots shown in this work.[5] The inset shows a zoomed-in view of the region traversed by the galaxy. The initial snapshot of the simulation is marked by the red star, and the final snapshot is indicated by the red square. The arrows connect one snapshot to the next, tracing the galaxy in time. The thick black line is the M99 relation. As the simulation evolves, the galaxy wanders around the M99 relation and crosses it many times, but it is typically close to the relation. The 'spur' above the relation corresponds to the first ~ 1 Gyr, when the galaxy is still gas-rich and dust-obscured, as indicated by the high IRX values shown in the top panel.

Figure 5.2 shows the results for one of the $z \sim 2-3$ isolated disk simulations from H13, b6. This simulation differs from that shown in Figure 5.1 in a few important aspects: first, its baryonic mass is 4×10^{11} $M_{\odot}$, whereas that of the $z \sim 0$ simulation is 5×10^{10} $M_{\odot}$. The $z \sim 2-3$ disk galaxy has an initial gas fraction $f_g \equiv M_{\rm gas}/(M_{\rm stars} + M_{\rm gas}) = 0.8$, whereas the $z \sim 0$ disk has $f_g = 0.16$. The simulated $z \sim 0$ disk galaxy contains a bulge, which acts to stabilize the gas disk, whereas the $z \sim 2-3$ disk galaxy does not. The star particles in the initial conditions are assigned ages and metallicities appropriate for the assumed redshift; thus, a significant fraction of the initial stellar mass of the $z \sim 2-3$ disk is comprised of young and intermediate-age stars, whereas the stellar mass $z \sim 0$ disk is always dominated by old stellar

[5]The ranges were set based on the IRX-β region spanned by real galaxies (e.g., Takeuchi et al., 2012; Casey et al., 2014c). Use of common axes enables the reader to more easily compare the amount of evolution exhibited by the different simulations and the magnitude of the differences that result from the choice of dust model, for example.

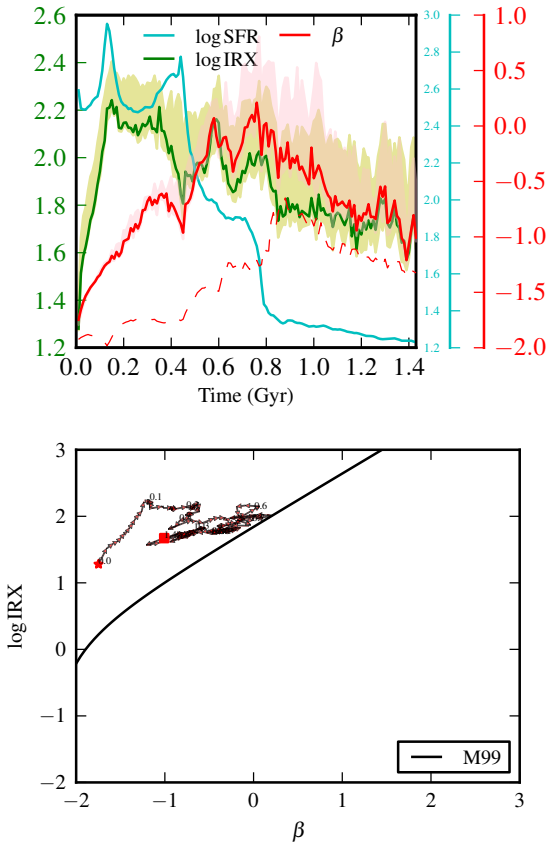

Figure 5.2: The time evolution (*top*) and IRX-β (*bottom*) plots shown in Figure 5.1 but for a simulated $z \sim 2-3$ isolated disk, b6 from H13. The difference between the UV slopes of the attenuated (thick-solid red line) and unattenuated (thin-dashed red line) SEDs is more pronounced compared with the $z \sim 0$ isolated disk shown in Figure 5.1. The simulated $z \sim 2-3$ isolated disk galaxy tends to lie above the M99 relation.

populations. Finally, the structural properties of this galaxy (e.g., dark matter halo and disk scalelength) have been scaled to $z = 3$ (see H13 for details). The above differences imply that the $z \sim 2-3$ disk has a much higher gas surface density, and thus SFR surface density, than does the $z \sim 0$ disk.

The top panel of Figure 5.2 shows that the time evolution of the SFR and IRX are qualitatively similar to those of the $z \sim 0$ galaxy discussed above, although both the SFR and IRX values are considerably greater than for the $z \sim 0$ disk owing to the much higher gas surface density (and thus attenuation) in the $z \sim 2-3$ simulation. In contrast with the $z \sim 0$ simulation, there is a long-term trend in β. The value of β tends to increase (i.e., the SED becomes redder) until ~ 0.7 Gyr, after which it decreases (the SED becomes bluer). The reason for this qualitatively different behavior is that in the $z \sim 2-3$ simulations, a significant fraction of the pre-existing stars have ages of a few hundred Myr and can thus contribute significantly to the UV emission. As these stars age, the UV slope becomes redder. The IRX values start a gradual decline after 700 Myr while the SED becomes bluer. Another significant difference is that for the $z \sim 2-3$ simulation, the difference between the UV slopes of the attenuated (thick red line) and intrinsic (thin red line) SEDs is considerable. The attenuated and intrinsic β values can differ by as much as ~ 2, which indicates that dust reddening significantly affects the UV slope measured for this galaxy, unlike for the $z \sim 0$ galaxy. Relatedly, the viewing-angle-dependent dispersion in β and IRX (the pink and yellow shaded regions, respectively) is significant, again in contrast

with the $z \sim 0$ disk galaxy simulation discussed above. It is worth noting that the difference between the observed and intrinsic β values varies with time, and it becomes less as the gas is depleted and the galaxy's ISM becomes less opaque to UV photons as dust is locked into stars.

The bottom panel of Figure 5.2 summarizes the evolution in the $IRX - \beta$ plane. The galaxy tends to lie above the M99 relation, and it comes close to the relation only at around the time when it experiences a sharp decline in SFR at ~ 0.7 Gyr. For such a galaxy, using the measured UV slope and the M99 relation to correct for dust would cause one to significantly underpredict the IR luminosity, sometimes by more than an order of magnitude.

5.3.2 Galaxy mergers

Our simulation suite includes 10 $z \sim 0$ mergers (see L14 for details) and 32 $z \sim 2 - 3$ mergers (see H13 for details). Figure 5.3 shows the time evolution of the observed and intrinsic UV slopes, IRX, log SFR and the separation of the central supermassive BHs (a proxy for merger stage) for the M3M3e; the evolution of the other $z \sim 0$ merger simulations in which a strong starburst is induced is similar. There is a strong increase in the SFR at ~ 2.3 Gyr, when the two galaxies are separated by less than 10 kpc. The peak of the starburst occurs at ~ 2.5 Gyr. This phase is followed by a quiescent, 'red and dead' phase owing to gas consumption during the starburst and AGN feedback. The time evolution of IRX is similar to

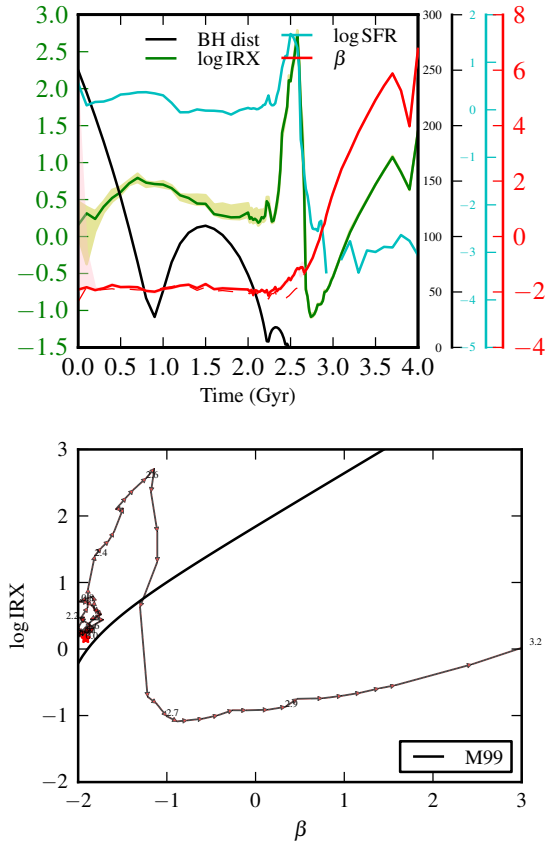

Figure 5.3: The time evolution (*top*) and IRX-β (*bottom*) plots shown in Figure 5.1 but for a simulated $z \sim 0$ equal-mass merger system, M3M3e from L14. *Top:* The black line in this panel corresponds to the separation of the central supermassive BHs in kpc; this is a proxy for merger stage. There is a strong starburst induced near final coalescence (at ~ 2.5 Gyr), immediately after which star formation is quenched because of gas consumption and AGN feedback. The time evolution of IRX is similar to that of the SFR. β has a relatively constant value of ~ -2 until the starburst, when it increases. Post-coalescence, $\beta > 0$ (i.e., the UV color is very red) owing to the star formation being quenched. The observed and intrinsic β values are almost identical except for during the starburst, and the variation in IRX and β with viewing angle is small; both of these results indicate that dust attenuation has minor effects on the UV slope in this case despite the system being a ULIRG at coalescence. *Bottom:* The merger is initially near the M99 relation, but it moves significantly above it during the coalescence-phase starburst. Subsequently, it moves rapidly below the relation as star formation is quenched and then moves to the right as its stellar population ages.

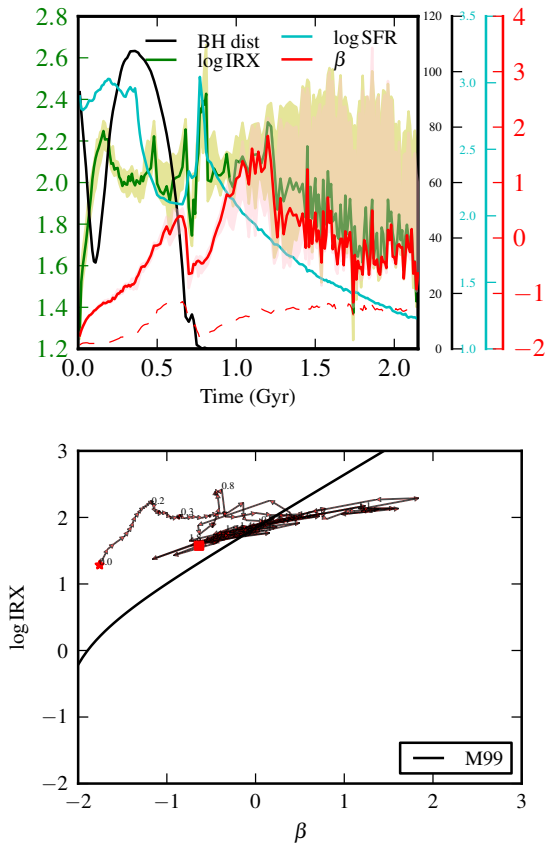

Figure 5.4: Similar to Figure 5.3 but for one of the simulated $z \sim 2-3$ equal-mass mergers from H13, b6b6m. *Top:* There is a strong starburst at merger coalescence ($\sim$ 800 Myr), after which the SFR decreases but not as rapidly as in the $z \sim 0$ merger presented above. At the end of the simulation, SFR ~ 20 $M_\odot$ yr^{-1}. As for the $z \sim 0$ merger, the evolution of IRX is similar to that of the SFR. However, the evolution of both the observed and intrinsic β values differ qualitatively from the $z \sim 0$ case: the intrinsic β (thin red line) increases as the relatively young stars present in the initial conditions age, decreases during the starburst, and then increases again. The time evolution of the observed β (thick red line) is similar except after ~ 1.2 Gyr, when it decreases because dust reddening is becoming less significant. The difference between the observed and intrinsic UV slopes is large throughout the simulation, reaching as high as ~ 3. This indicates that dust strongly affects the UV slope of this system. The viewing-angle-dependent dispersion in IRX and β (yellow and pink shaded regions, respectively) is very large in the post-starburst phase. *Bottom*: The system starts above the M99 relation and moves closer to it until the coalescence-phase starburst, when it moves back above the relation. The system then crosses the relation and moves back onto it, where it remains.

that of the SFR. Interestingly, after ~ 2.7 Gyr, IRX starts to increase because the intermediate-age and old stellar populations that dominate the dust heating in this phase emit increasingly less 1600 Å photons. Both the observed and intrinsic β values are relatively constant (~ -2) until the coalescence-phase starburst. During the starburst, the observed (intrinsic) β increases (decreases), and both increase in the post-starburst phase because star formation has been quenched and the stellar populations are passively evolving. The two β values are similar except during the starburst phase, and even then, the difference is modest compared with the $z \sim 2-3$ simulations. This indicates that dust reddening does not significantly affect the UV slope in this system despite the system having IRX > 1 (i.e., $L_{\rm FIR} > L_{\rm UV}$) for much of its evolution and being a ULIRG for a brief time during the starburst. For the same reason, the dispersion in IRX and β due to viewing angle is small.

The time evolution of the galaxy in the $IRX - \beta$ plane is shown in the bottom panel of Figure 5.3. As in the previous IRX-β plots, the points corresponding to different snapshots are connected by arrows to show the direction of time. The initial time snapshot is indicated with a red star, and the end of the simulation is marked with a red square. The system remains close to the M99 relation up until the start of the coalescence-phase starburst, during which there is a sharp increase in IRX without a significant change in the UV continuum slope. Consequently, the system moves above the relation. When star formation is quenched, the system moves rapidly

below the relation, and it then moves to the right as its stellar populations ages.[6]

The time evolution of one of the $z \sim 2-3$ equal-mass mergers (b6b6m from H13) is shown in Figure 5.4. The top panel shows that the starburst induced at merger coalescence occurs at $t \sim 0.8$ Gyr. In contrast with the $z \sim 0$ merger examined above, star formation is not fully quenched: at the end of the simulation, the SFR is still > 10 $M_\odot$ yr^{-1}. The IRX value tends to track the SFR. For example, during the coalescence-induced starburst, IRX increases sharply, as in the $z \sim 0$ merger shown in Figure 5.3. Pre-coalescence, the UV continuum slope, β, increases from ~ -1.8 to ~ 0.3, and it then decreases by ~ 1 during the coalescence phase. It subsequently increases from ~ -0.7 to ~ 1.8, indicating that the galaxy transitions from blue to red, and then it decreases to ~ -0.3 over the remainder of the simulation. Owing to the lack of quenching, the galaxy remains blue. The difference between the observed (thick red line) and intrinsic (thin red line) UV slopes is large throughout the simulation, reaching as high as ~ 3. This indicates that dust strongly affects the UV slope of this system. The viewing-angle-dependent dispersion in IRX and β (yellow and pink shaded regions, respectively) is very large in the post-starburst phase.

The bottom panel of Figure 5.4 shows the evolution of the $z \sim 2-3$ merger in the IRX-β plane. Initially, the system lies above the M99 relation. During the local minimum in the SFR at $t \sim 0.6$ Gyr, it moves onto the relation, and it subsequently

[6]Note that because of our use of common axes for all IRX-β plots, the system moves off the plot at 3.2 Gyr.

moves back above the relation during the starburst induced at final coalescence of the system. Shortly after coalescence, it crosses the relation, and a few 100 Myr later, it returns to near the relation, where it remains until the end of the simulation because the galaxy is still actively forming stars at a rate > 10 $M_\odot$ yr^{-1}.

5.4 Impact of dust composition

In the above analysis, the MW-type dust model of Draine & Li (2007) was used in the radiative transfer calculations. It is worthwhile to investigate how the dust composition affects the predicted UV slope and IRX value. In particular, the SMC extinction curve of Draine & Li (2007) differs considerably from the MW curve in the UV: whereas the MW extinction curve exhibits a 'bump' at ~ 2175 Å, the SMC curve does not. Thus, the two dust models can lead to different dust reddening in the UV and consequently different observed UV slopes for a fixed intrinsic UV slope (i.e., fixed stellar population). The potentially drastic impact of dust grain composition on the positions of galaxies in the IRX-β plane has been discussed in the literature (e.g., Bell et al., 2002; Shapley, 2011; Mao et al., 2014), but to the best of our knowledge, it has not been explored using the combination of hydrodynamical simulations and dust radiative transfer calculations that we employ in this work.

To investigate the impact of the dust grain composition, we performed radiative transfer on the $z \sim 0$ major merger simulation discussed above, M3M3e from L14,

assuming SMC-type dust instead of the fiducial MW-type dust. The results of these radiative transfer calculations are compared with those of the standard MW-dust run in Figure 5.5. The top panel shows how the assumed dust grain model impacts the evolution of the merger in the IRX-β plane. The blue arrows follow the evolution of the system when SMC-type dust is assumed, whereas the red arrows follow the evolution of the same system modeled with MW-type dust (this track is identical to that shown in the bottom panel of Figure 5.3). For the first $\sim$ 2.7 Gyr of the simulation, when the system is actively forming stars (see Figure 5.3), the assumed dust model has a very significant impact on the position of the system in the IRX-β plane. In general, β is greater (i.e., the SED is redder) when SMC-type dust is assumed. For this reason, at fixed time, the merger can lie above the M99 relation if MW-type dust is assumed in the radiative transfer calculation but below it if SMC-type dust is used. The effect is greatest during the coalescence-phase starburst ($t \sim 2.4 - 2.6$ Gyr): when MW dust is assumed, the merger-driven starburst causes the system to move above the relation, but when SMC dust is assumed, the system moves *closer* to the relation during the starburst.

The bottom panel of Figure 5.5 illustrates why the assumed dust model has such a drastic impact on the system's position in the IRX-β plane. The black line is the intrinsic SED of the system at $t = 2.4$ Gyr, and the red (blue) line is the attenuated SED obtained when MW-type (SMC-type) dust is used in the radiative transfer calculation. The yellow shaded region denotes the wavelength range that is used to

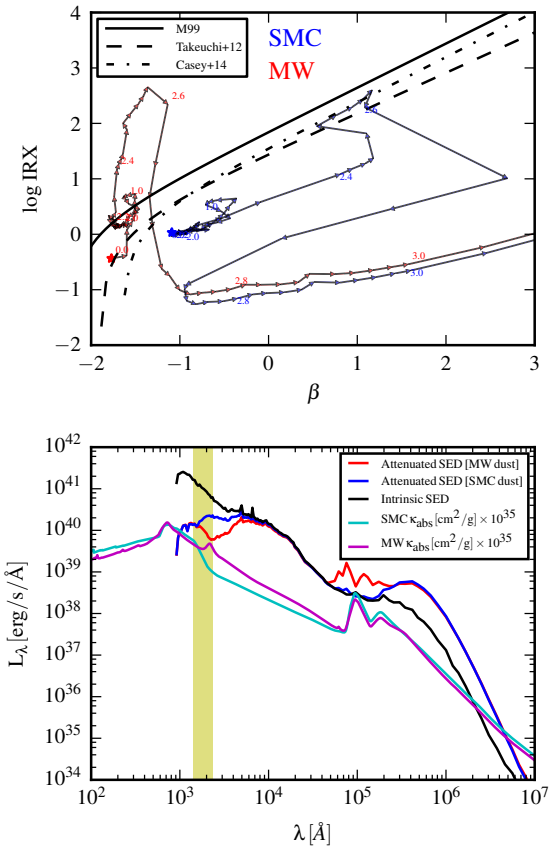

Figure 5.5: Demonstration of the impact of the assumed dust grain model on the final IRX and β values. *T*op: The evolution of the M3M3e $z \sim 0$ major merger simulation in the IRX-β plane when MW-type (red arrows) and SMC-type (blue arrows) dust is used in the radiative transfer calculations. For the first ~ 2.7 Gyr of the simulation, when the system is actively forming stars, the assumed dust model *qualitatively* changes the evolution of the merger in the IRX-β plane. β is greater (i.e., the SED is redder) when SMC-type dust is assumed; IRX is relatively insensitive to the assumed dust model except for low IRX values. *B*ottom: Comparison of the SEDs of the M3M3e simulation at $t = 2.4$ Gyr. The intrinsic SED of the galaxy is shown in black. The attenuated SEDs (including dust re-emission) predicted when MW-type and SMC-type dust are assumed are shown in red and blue, respectively. The yellow region indicates the wavelength range that is used to compute the UV slope. The absorption cross-section per unit mass of the MW (magenta line) and SMC (cyan line) dust models (renormalized as indicated in the legend) are also shown. It is clear that the two SEDs have very different UV slopes: β is negative (positive) when MW (SMC) dust is assumed. The extinction curves clearly show that the difference between the UV slopes obtained with the two dust models is due to the presence of the UV bump at 2175 Å in the MW curve and the change in the slope of the SMC curve in this wavelength range.

compute the UV slope (1300 Å $< \lambda <$ 2300 Å). The magenta and cyan curves show the absorption cross-section per unit mass (in arbitrary units) for the MW- and SMC-type dust models, respectively. As is evident from comparing the SEDs, the 2175 Å, feature present in the MW curve results in a more negative UV slope compared with the SMC dust model. The SMC curve starts to decrease more steeply with increasing wavelength near where the 2175 Å feature becomes evident in the MW curve, which exacerbates the difference in the UV slopes of the two SEDs. The difference between the two observed UV slopes, which is completely due to the assumed dust composition, is approximately 2. Although there is a large difference in the UV slope due to the dust grain model, the effect on IRX is modest for the following reasons: when IRX is high, the vast majority of UV photons from the young stars that dominate the intrinsic UV luminosity are absorbed regardless of whether MW- or SMC-type dust is assumed. Thus, $L_{\rm FIR}$ is insensitive to the dust model. Because the observed UV is dominated by unobscured stars (i.e., the UV and IR emission are essentially decoupled), $L_{\rm UV}$ is also not significantly affected. Thus, when IRX is high, it is not affected by the dust model. For example, comparing the $t = 2.4$ Gyr points in the IRX-β plane in the top panel reveals that the two SEDs have the same IRX value but very different UV slopes. Thus, the difference in β is the primary driver of the difference in the IRX$-\beta$ evolution.

After the starburst, when star formation has been quenched, the choice of dust model matters little. The MW track tends to be slightly above the SMC track because

for fixed dust column density, the MW dust model yields a greater optical depth in the UV–optical regime. When IRX is low (as it is in this phase), and thus the galaxy is not opaque to UV photons, the increase in the optical depth caused by assuming MW-type rather than SMC-type dust can lead to a non-negligible increase in the IR luminosity and decrease in the observed luminosity, thus causing a non-negligible (but small) increase in IRX.

5.5 Dispersion in the UV slope

Various factors can in principle lead to dispersion in the IRX-β plane, including dust geometry (Cortese et al., 2006b), SFH (Kong et al., 2004), the mean age of the stellar population (Mao et al., 2012; Grasha et al., 2013) or stellar mass (Álvarez-Márquez et al., 2016). Boquien et al. (2012) studied a set of face-on normal star forming spiral galaxies to understand why normal star-forming galaxies deviate from starburst galaxies in terms of their positions in the IRX-β plane. They found that the intrinsic dispersion in the UV slope correlates most strongly with the distance from the M99 relation. Kong et al. (2004) suggest that the dispersion results from differences in the SFHs of galaxies (by considering the birth rate parameter b, which is the ratio of the current to past SFR; note that this parameter can be quite sensitive to how one defines 'current' when the SFR is highly variable; e.g., Sparre et al. 2015a). Both studies point to the importance of underlying SFH for the observed dispersion

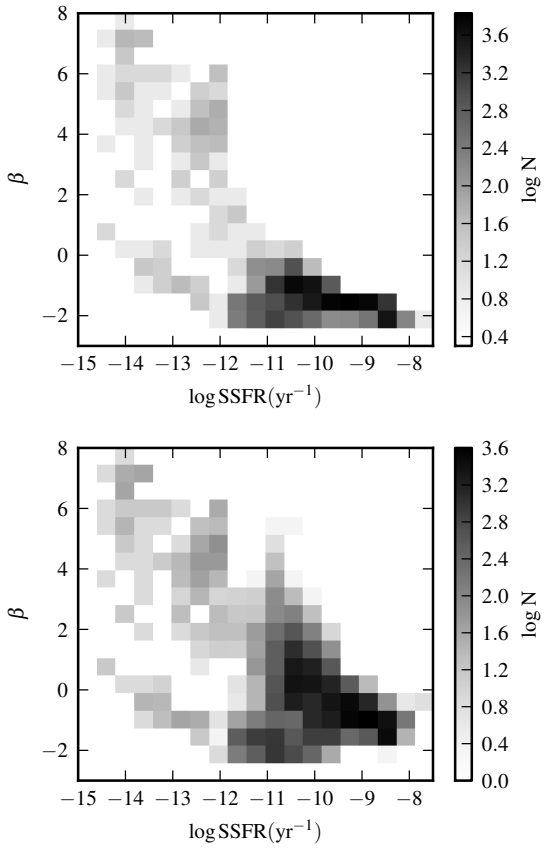

Figure 5.6: 2D histograms of the intrinsic (*top*) and observed (i.e., attenuated; *bottom*) β values versus log (SSFR/yr^{-1}) for all simulated galaxies analyzed in this work (i.e., both the $z \sim 0$ and $z \sim 2-3$ datasets). Note that the colorbar indicates the logarithm of the number of SEDs in a given pixel. Both the intrinsic and observed β values are anti-correlated with SSFR because in more actively star-forming galaxies, young, massive stars dominate the luminosity and cause the UV slope to be blue. The scatter at fixed SSFR is also anticorrelated with SSFR because the past SFH does not affect the UV slope if very young stars dominate the UV luminosity. A comparison of the two histograms reveals that for galaxies with high SSFR, dust attenuation causes the observed UV slope to be redder than the intrinsic slope. For passive systems, β is essentially unaffected by dust attenuation. The bifurcation evident for SSFR $< 10^{-11}$ yr^{-1} is due to the inclusion of both low- and high-redshift simulations: at fixed SSFR, the $z \sim 0$ simulations tend to have lower β values.

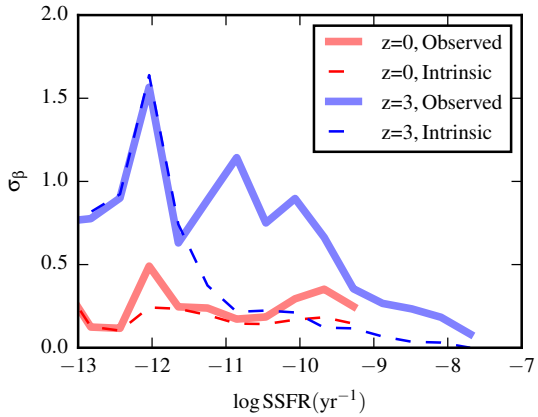

Figure 5.7: Dispersion in β versus log (SSFR/yr^{-1}). σ_β is defined by dividing the difference between the 16th and 84th percentile values of the β distribution (including all simulations and viewing angles) in a given SSFR bin by 2. The red (blue) lines correspond to the $z \sim 0$ ($z \sim 2-3$) simulations. The solid (dashed) lines denote the dispersion in the observed (intrinsic) β values. The dispersion in both the intrinsic and observed β values is anticorrelated with SSFR, as already observed from Figure 5.6. In the $z \sim 0$ simulations with high SSFR, SFH variations and dust attenuation contribute comparably to the dispersion; in lower-SSFR systems, SFH history variations dominate. In contrast, in the $z \sim 2-3$ simulations with SSFR $> 10^{-11.5}$ yr^{-1}, the β variation due to dust attenuation (related to both viewing angle-related effects and differences in dust geometry among different time snapshots and simulations) is much greater than that due to SFH variations. For actively star-forming galaxies, the dispersion in the observed β is greater for the $z \sim 2-3$ simulations than for the $z \sim 0$ simulations. Our results suggest that even if low-redshift galaxies obey a relatively tight IRX-β relation, this should not be the case at higher redshifts.

of galaxies in the IRX-β plane. Álvarez-Márquez et al. (2016) studied a stacked sample of LBGs at $z \sim 3$ and concluded that stellar mass best predicts deviations from the IRX-β relation. They found that more-massive LBGs have bluer colors and higher dust attenuation. This is in agreement with the trend observed by Casey et al. (2014c) for DSFGs. Mao et al. (2012) studied spatially resolved normal star-forming galaxies from the SINGS (Kennicutt Jr et al., 2003a; Dale et al., 2007a) sample by separating a galaxy into UV-emitting clusters and background disk and bulge regions. The found the mean stellar population age contributes significantly to the dispersion in the IRX-β plane, and the location of the galaxy as a whole in the IRX-β plane is determined largely by the local background regions.

We can distinguish between scatter due to different SFHs and that due to dust geometry by comparing the dispersions in the intrinsic and observed (i.e., attenuated) β values because the intrinsic UV slope depends only on the SFH, whereas the latter also includes the viewing angle-dependent effects of dust. In Figure 5.6, we show 2D histograms of the intrinsic (*top*) and observed (*bottom*) β values versus specific SFR (SSFR$\equiv$SFR/M$_\star$). All simulations analyzed in this work (i.e., both isolated disks and mergers at both $z \sim 0$ and $z \sim 2-3$) are shown here. Both the intrinsic and observed β values are anticorrelated with SSFR. This implies that in the most actively star-forming systems, young, massive stars dominate the UV emission and thus make the UV slope blue. Moreover, the dispersion at fixed SSFR is anticorrelated with SSFR, which implies that the past SFH affects β less in actively star-forming systems. A

comparison of the two panels reveals that for galaxies with SSFR $> 10^{-12}$ yr^{-1}, dust attenuation causes β to increase (i.e., the UV slope to become redder), whereas for systems with lower SSFR values, the intrinsic and observed β distributions are similar. The bifurcation evident for SSFR $< 10^{-11}$ yr^{-1} is due to the inclusion of both low- and high-redshift simulations: at fixed SSFR, the $z \sim 0$ simulations tend to have lower β values.

Figure 5.7 shows the dispersion in β, σ_β, versus SSFR. σ_β is computed by binning the SEDs in terms of their corresponding SSFR values and then dividing the difference between the 16th and 84th percentiles by two; for a normal distribution, this measure would equal the standard deviation. σ_β thus incorporates variations due to viewing angle, the time evolution of a given system, and the differences among the simulations. The solid (dashed) lines correspond to the observed (intrinsic) β values, and red (blue) denotes $z \sim 0$ ($z \sim 2-3$). This figure reinforces our conclusion from Figure 5.6 that the dispersions in both the intrinsic and observed β values are anticorrelated with SSFR. Considering the $z \sim 0$ simulations, we note that the dispersions in the intrinsic and observed β values differ by a modest amount, and the difference is greater at high SSFR. Computing the difference between the intrinsic and observed σ_β values in quadrature, which characterizes the contribution of dust attenuation to the dispersion (related to both viewing angle-related effects and differences in dust geometry among different time snapshots and simulations), we find that dust adds at most 0.4 to σ_β, and it typically adds < 0.2. Thus, in the actively star-forming $z \sim 0$ simulations,

dust attenuation and SFH variations contribute comparably to the dispersion in the observed β values, whereas in systems with lower SSFR, SFH variations dominate the dispersion.

In contrast, for the $z \sim 2-3$ simulations, the difference between the intrinsic and observed β dispersions is significant. Again computing the difference in the σ_β values in quadrature, we find that the variation due to dust attenuation dominates that due to SFH variations in all bins with SSFR $> 10^{-11.5}$ yr^{-1}, in contrast with the $z \sim 0$ simulations. For systems with lower SSFR values, the intrinsic and observed β dispersions are almost identical, which indicates that SFH variations dominate the dispersion. Finally, we note that for actively star-forming galaxies, the dispersion in the observed β values at fixed SSFR is greater for the $z \sim 2-3$ simulated galaxies than for those intended to be representative of $z \sim 0$ galaxies. Consequently, our results suggest that even if low-redshift galaxies obey a tight IRX-β relation (i.e., the M99 relation), this is unlikely to be the case at higher redshift. Moreover, the above results suggest that the sought-after 'second parameter' (i.e., what property best predicts deviations from the M99 relation) may depend on the galaxy type and redshift considered.

5.6 DSFGs in the IRX-β plane

Many DSFGs at $z \sim 2-3$ have very blue UV continuum slopes (i.e., negative β values) and high IRX values (Casey et al., 2014c), which makes them lie above the M99 relation. Very blue and dusty systems were also found in a study of 16 individually *Herschel* PACS 100-μm- and 160-μm-detected LBGs at $z \sim 3$ (Oteo et al., 2013a). Although these samples are biased by the IR selection, the results may indicate that massive galaxies tend to have bluer UV slopes and higher IRX values compared with less-massive galaxies (Álvarez-Márquez et al., 2016). Moreover, where DSFGs reside in the IRX-β plane may yield insights into the origin of their extremely high SFRs: Casey et al. (2014c) argue that the fact that DSFGs lie above the M99 relation is evidence that they are short-timescale starbursts rather than 'main sequence' galaxies (i.e., galaxies near the approximately linear SFR–stellar mass relation).

We can directly address this question using our simulation suite. In Figure 5.8, we show the locations of our simulated $z \sim 2-3$ DSFGs in the IRX-β plane; the top panel shows the results of the simulated $z \sim 2-3$ mergers, whereas the bottom panel shows the simulated $z \sim 2-3$ isolated disk galaxies. The orange, green, and blue points correspond to simulated LIRGs ($10^{11} < L_{IR}/L_{\odot} < 10^{12}$), ULIRGs ($10^{12} < L_{IR}/L_{\odot} < 10^{13}$) and hyper-LIRGs (HyLIRGs; $L_{IR} > 10^{13} L_{\odot}$), respectively. (There are no blue points in the bottom panel because the simulated isolated disks never attain $L_{IR} > 10^{13} L_{\odot}$.) In both panels, the red points correspond to real $z \sim 2.5-3.5$

DSFGs selected from the COSMOS survey (Scoville et al., 2007), the IRX and β values of which were presented in Casey et al. (2014c).

In both panels, the regions in the IRX-β plane spanned by the real and simulated DSFGs are broadly consistent, although for log IRX $\gtrsim 2.5$, the specific simulations used here do not span the full range of β spanned by real DSFGs, which can be both slightly bluer and significantly redder than the simulated galaxies (see also Wuyts et al., 2009). For the mergers (*top*), the offset from the M99 relation tends to increase with IR luminosity; all of the simulated HyLIRGs are well above the M99 relation, which indicates that despite having effectively all of their luminosity absorbed and reradiated by dust ($L_{IR}/L_{UV} > 100$), they have blue UV continuum slopes. The reason for our simulated DSFGs having blue UV colors is that in these IR-luminosity-selected systems, the UV and IR are essentially decoupled: the IR luminosity is powered by stars that are invisible in the UV, whereas the UV emission originates from a 'frosting' of unobscured young stars. This holds for both the simulated mergers and isolated disks.

Notably, the bottom panel shows that our simulated gas-rich $z \sim 2-3$ isolated disk galaxies are similar to DSFGs in terms of their location in the IRX-β plane. These galaxies are *not* undergoing merger-driven starbursts by construction. Thus, our results demonstrate that the position of DSFGs in the IRX-β plane does not necessarily imply that they are short-lived starbursts, contrary to the claim of Casey et al. (2014c); instead, DSFGs well above the M99 relation can be steadily star-

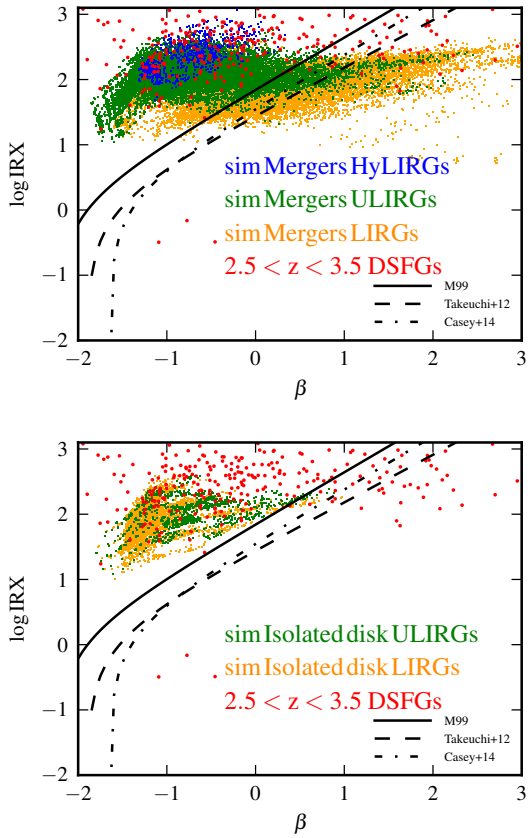

Figure 5.8: The positions of our simulated $z \sim 2-3$ DSFGs in the IRX-β plane. The mergers (isolated disks) are shown in the *top* (*bottom*) panel. The points are color-coded according to IR luminosity: orange, green, and blue points correspond to simulated LIRGs ($10^{11} < L_{IR}/L_{\odot} < 10^{12}$), ULIRGs ($10^{12} < L_{IR}/L_{\odot} < 10^{13}$) and hyper-LIRGs (HyLIRGs; $L_{IR} > 10^{13} L_{\odot}$), respectively. In both panels, the red points correspond to the observed $z \sim 2.5-3.5$ DSFGs from Casey et al. (2014c). It is evident that both the simulated mergers and isolated disk can become (U)LIRGs during their evolution. However, only the mergers can reach $L_{IR} > 10^{13} L_{\odot}$ and log IRX > 2.5. Because the simulated isolated disks overlap with observed DSFGs in the IRX-β plane, the fact that some real DSFGs lie well above the M99 relation is not evidence that they are powered by short-lived starbursts.

forming, massive, gas-rich disks as long as they are sufficiently dust-obscured, which is a natural outcome for high-gas-fraction, metal-enriched galaxies. Consequently, high-z DSFGs may represent a heterogeneous population of massive, gas-rich, steadily star-forming galaxies, merger-induced starbursts, and obscured AGN (e.g., Hopkins et al., 2010b; Hayward et al., 2011a, 2012, 2013b,a; da Cunha et al., 2015; Koprowski et al., 2016). We do find that all of the simulated galaxies with $L_{IR} > 10^{13} L_{\odot}$ (see also Hopkins et al. 2010b) and, of the lower-luminosity simulated galaxies, those with the highest IRX values (log IRX > 2.5) are exclusively mergers, and in the simulations, these HyLIRGs are typically powered by combination of merger-induced starbursts and obscured AGN (Roebuck et al., submitted). However, we cannot determine whether these are physical limits or simply artifacts of the specific parameter space spanned by the simulations.

However, it should be noted that the IRX and β values plotted in Figure 5.8 are those obtained when MW-type dust is used in the radiative transfer calculations. As we have shown in section 5.4, using MW-type dust yields more negative UV slopes than when SMC-type dust is assumed. Consequently, if we were to assume SMC-type dust when performing the radiative transfer calculations, our simulated galaxies might not populate the low-β, high-IRX region that is occupied by a significant fraction of real DSFGs. Thus, it is possible that the location of DSFGs in the IRX-β plane may encode information regarding their dust composition. This is an interesting topic that could be explored with future simulations.

5.7 comparison with previous work

We now compare our results with those of some previous theoretical works. The evolutionary tracks of galaxies in the IRX-β plane were previously studied in the context of semi-analytic models (SAMs) coupled with radiative transfer calculations assuming simplified geometries (GRASIL; Silva et al., 1998) by Granato et al. (2000a, hereafter G00). G00 find that in the early stages of a starburst, the UV slopes of their model galaxies become bluer (more negative). When the SFR decreases, and consequently older stellar populations dominate the intrinsic UV slope, the system evolves towards more positive (redder) β and lower IRX values. In G00's model, the strength of the burst defines the evolutionary path on the IRX-β plane. Stronger starbursts have only slightly negative or positive (red) UV slopes ($\beta \gtrsim -0.5$), initially because they experience high attenuation on timescales longer than the exponential decay timescale of the SFR and later because the stellar population has turned old. Their IRX values are generally $\gtrsim 10$. In contrast, weaker starbursts span a larger dynamical range in the IRX-β plane because these galaxies quickly exhaust their gas, which causes the attenuation to decrease rapidly and makes them evolve towards low IRX and negative β values. We note that G00 assume MW dust, as have we in our fiducial calculations, and can reproduce the Calzetti attenuation law, despite the conclusion of Gordon et al. (1997) that SMC-type dust is needed to reproduce the Calzetti law.

Unlike G00, when a strong burst occurs in our simulations (e.g., the M3M3e

simulation shown in Figure 5.3), the system moves almost vertically in the IRX-β plane because IRX increases by a large amount, whereas the UV slope becomes only slightly redder. The two results might seem contradictory, but the difference lies in how we define the onset of starburst. If consider the evolution of the M3M3e merger system starting with the peak of the starburst (during the coalescence phase), which corresponds to G00's definition (because they assume an exponentially declining SFH for the burst), we see a similar trend: the galaxy maintains a relatively flat UV slope while moving toward lower IRX values. The further evolution of the system when the stellar population becomes old is similar to the starbursts modeled in G00. The starbursts modeled by G00 lie on the M99 relation as long as the age of the starburst is < 50 Myr. However, a comparison of figure 7 of G00 with Figure 5.8 indicates that the starbursts in the G00 model never occupy the high-IRX, low-β region spanned by both our simulated DSFGs and observed DSFGs. This discrepancy may be a result of the parameter space that they considered, their assumption of an exponentially declining SFH for bursts, or/and the simplified geometry assumed in their radiative transfer calculations.

Khakhaleva-Li & Gnedin (2016) performed radiative transfer on galaxies formed in cosmological simulations from the "Cosmic Reionization on Computers" (CROC) project (Gnedin, 2014) to compare the UV and IR properties of their simulated $z > 5$ galaxies, including their positions in the IRX-β plane, with observations. They find that in order to match the observed UV luminosity function at $z > 5$, they must

include the effects of dust destruction via sublimation in supernova shocks; otherwise, their galaxies are too dusty and thus UV-faint to explain the observed UV luminosity function. Their simulated galaxies lie near the M99 relation, although IRX can vary by approximately an order of magnitude at fixed β. The locus of their simulated galaxies in the IRX-β plane is consistent with some $z > 5$ galaxies for which both β and IRX have been measured (Capak et al., 2015), but the galaxies with log IRX > 0.5 from Capak et al. (2015) and the $z \sim 7.5$ galaxy presented by Watson et al. (2015) lie outside the region spanned by the simulated galaxies. Because our simulations and theirs cover disjoint regions of parameter space in terms of redshift and mass, it is not possible to make detailed comparisons between our results and theirs. However, their results highlight the potential importance of dust destruction for accurately predicting the UV properties of simulated galaxies and provide motivation for future studies that include more complex treatments of dust production, growth and destruction.

5.8 Implications for observations

Our simulation results suggest that there is not a tight relation between IRX and β that applies to all galaxies at all redshifts. The $z \sim 0$ simulated galaxies tend to lie near the M99 relation, which was determined based on observations of galaxies in the local Universe. However, during merger-induced starbursts, even the $z \sim 0$ galaxies can depart significantly from the relation: because IRX increases significantly but

β is almost unaffected, the $z \sim 0$ merger-induced starbursts, such as that shown in Figure 5.3, tend to lie above the M99 relation. The $z \sim 2-3$ simulations – of both disk galaxies and mergers – deviate more significantly from the M99 relation: even when they are not undergoing starbursts, they tend to lie above the relation.

These results are consistent with observational works that have demonstrated that some classes of galaxies deviate significantly from the M99 relation. As already discussed above, observed DSFGs tend to lie above the M99 relation and do not exhibit any relationship between IRX and β (e.g., Goldader et al., 2002; Bell et al., 2002; Howell et al., 2010b; Casey et al., 2014c). Conversely, some galaxies lie significantly below the M99 relation (i.e., have lower IRX than expected from the relation given their β). This was demonstrated for the lensed galaxies cB58 at $z \sim 2.7$ (Pettini et al., 1999) and the Cosmic Eye (Smail et al., 2007) at $z \sim 3.07$. Similarly, Reddy et al. (2012b) found that young systems (age < 100 Myr) at $z \sim 2$ lie below the M99 relation.

Moreover, we have demonstrated that the dust composition – specifically the strength of the 2175 Å feature – can have a very dramatic effect on the UV slope. Consequently, extrapolation of the locally calibrated IRX-β relation to regimes for which it is not observationally constrained may be problematic if, e.g., the dust composition of high-redshift galaxies is significantly different from that of $z \sim 0$ galaxies. How the strength of the UV bump varies with galaxy properties and redshift is still poorly understood, but there are some useful observational constraints. The com-

monly employed Calzetti et al. (1994a) attenuation law, which was defined based on observations of local-Universe starburst galaxies, does not exhibit a UV bump. Based on a study of ∼10,000 $z < 0.1$ star-forming galaxies, Battisti et al. (2016) derived an average attenuation curve that does *not* have a significant 2175 Å feature. However, Motta et al. (2002) presented evidence for the UV bump in a gravitationally lensed normal early type galaxy at $z = 0.83$. Since then, other detections for high-redshift galaxies have been reported in the literature (Noll et al., 2009; Buat et al., 2011; Kriek & Conroy, 2013b). Conroy et al. (2010) studied attenuation as a function of inclination using a sample of nearby disk galaxies. Trends due to dust attenuation alone can be identified in such studies because stellar population properties are unrelated to inclination. The trends observed by Conroy et al. (2010) suggest the presence of the 2175 Å feature with an amplitude ∼80% of the canonical MW value. Studying ~ 30 galaxies at $z > 1$, Buat et al. (2011) detected a significant UV bump at 2175 Å but with an amplitude $\sim 35\%$ of that of the MW extinction curve. For a sample of galaxies in the redshift range $0.5 < z < 2$, Kriek & Conroy (2013b) found evidence for a UV bump whose strength increases with the slope of the attenuation curve. Given the above mixed and perhaps even contradictory results, more effort clearly needs to be invested in understanding how the composition of dust varies across cosmic time and among different galaxy populations.

The IRX-β relation is often applied to classes of galaxies (in terms of properties such as mass and redshift) for which the IRX-β relation is not directly constrained.

The above discussion suggests that it is unlikely that there is a universal IRX-β relation; instead, variations in both global galaxy properties and dust composition can cause significant deviations from the M99 relation. Constraints on the SFH of the Universe at $z \gtrsim 3$ are almost exclusively based on dust-correcting the UV luminosity using the M99 relation to obtain the SFR (e.g. Bouwens et al., 2009, 2012; Dunlop et al., 2012; Finkelstein et al., 2012; Bouwens et al., 2014). Use of the M99 relation can cause one to underestimate the SFRs of galaxies that lie above the M99 relation, such as DSFGs, possibly by multiple orders of magnitude. If such galaxies contribute non-negligibly to the SFH of the Universe, the UV-based constraints would not recover the true SFR density. For this reason, it is crucial to obtain direct constraints on obscured star formation via rest-frame IR observations of galaxies at higher redshift ($z \gtrsim 3$) and with less-extreme SFRs ($\lesssim 100$ $M_\odot$ yr^{-1}) than has been possible with surveys performed with, e.g., the JCMT and *Herschel*. ALMA is an excellent tool with which to address this challenge, and some very interesting constraints have already been obtained (e.g., Capak et al., 2015; Watson et al., 2015), but more work needs to be done.

5.9 limitations and future work

Although our simulations have yielded insights into the evolution of galaxies in the IRX-β plane, they are of course subject to some limitations. First, they are idealized

non-cosmological simulations. The advantage of such simulations is that they enable one to explore a significant region of the relevant parameter space while achieving the resolution necessary to perform radiative transfer on the simulated galaxies. However, their non-cosmological nature implies that effects such as cosmological gas accretion and subsequent mergers are not included, and the demographics of our simulation suite are not cosmologically representative. Moreover, we employ the Springel & Hernquist (2003) sub-resolution model for the structure of the ISM and the effects of supernova feedback. Although this model is still widely used, simulations that resolve the small-scale structure of the ISM and feature more sophisticated treatments of stellar feedback have been presented (e.g., Hopkins et al. 2014a; Agertz & Kravtsov 2015). It would be of great interest to repeat our analysis using such simulations. Finally, we have not employed a detailed model for dust production and destruction but rather assumed that the dust-to-metal density ratio is constant. As Khakhaleva-Li & Gnedin (2016) have noted, the details of dust production and destruction may have important implications for the UV and IR properties of simulated galaxies. It would thus be useful to perform an analysis similar to ours using simulations that include a detailed treatment of the relevant dust production and destruction channels (e.g., McKinnon et al., 2016b).

5.10 conclusions

We have analyzed a set of 51 hydrodynamical simulations of idealized (i.e., non-cosmological) galaxies, including both isolated disk galaxies and mergers at both $z \sim 0$ and $z \sim 2-3$, on which dust radiative transfer was performed in post-processing to yield UV–mm SEDs, from which we measured the UV continuum slope (β) and IRX. This method enables us to forward-model the evolution of the simulated galaxies in the IRX-β plane. Our primary conclusions are as follows:

- The simulated $z \sim 0$ isolated disk galaxies tend to reside near the M99 relation, whereas the $z \sim 2-3$ disks are generally above it (i.e., at fixed β, they have higher IRX values than expected from the M99 relation).

- In the simulated mergers, when a strong starburst is induced near coalescence, the systems tend to move almost vertically in the IRX-β plane because IRX increases significantly but β remains similar. In the post-starburst phase, if star formation is quenched via gas consumption and AGN feedback, IRX decreases rapidly, and β increases (i.e., the UV slope becomes redder) as the stellar population ages.

- The dust type that is assumed in the radiative transfer calculations drastically impacts the resulting 'observed' UV continuum slope. MW-type, for which the extinction curve exhibits a 'bump' at 2175 Å, results in a significantly more negative (i.e., bluer) UV slope than SMC-type dust, for which the extinction

curve does not exhibit the 2175 Å bump and has a steeper slope in the UV compared with MW-type dust. When the simulated galaxies are actively forming stars, the effects of the assumed dust model on the galaxies' positions in the IRX-β plane are more significant than the dispersion due to differences in galaxy properties, such as mass and SFH, the dispersion due to viewing angle, and model uncertainties other than the dust composition.

- The dispersion in both the intrinsic and observed β values is anticorrelated with SSFR. Considering actively star-forming simulated galaxies, dust attenuation dominates the dispersion in β for the $z \sim 2-3$ simulations, whereas in the $z \sim 0$ simulations, the contributions from SFH variations and dust attenuation are similar. At low SSFR, SFH variations dominate the β dispersion at both redshifts. These results suggest that the sought-after 'second parameter' (i.e., what property best predicts deviations from the M99 relation) should depend on the galaxy type and redshift considered.

- When SSFR $> 10^{-11.5}$ yr^{-1}, the dispersion in the observed β at fixed SSFR is higher in the $z \sim 2-3$ simulations than in the $z \sim 0$ simulations. This result indicates that even if a relatively tight IRX-β relation is obeyed by low-redshift galaxies, this should not be the case for galaxies at higher redshift.

- The simulated $z \sim 2-3$ DSFGs tend to lie above the M99 relation (i.e., have high IRX values yet blue UV slopes), similar to observed $z \sim 2-3$ DSFGs

(although this result may be sensitive to the assumed dust model). Consequently, in contrast with some previous claims in the literature, the position of DSFGs in the IRX-β plane is not evidence that they are powered by short-lived starburst events; rather, they may also be 'main sequence' galaxies as long as they are sufficiently dust-obscured. However, the simulations with $L_{IR} > 10^{13}$ or/and log IRX $\gtrsim 2.5$ are exclusively merger-driven starbursts, sometimes with a significant contribution from obscured AGN.

Our work adds to the growing consensus that a well-defined IRX-β relation is *not* obeyed by all galaxy populations. DSFGs, in particular, can deviate significantly, and inferring the SFR by dust-correcting the UV luminosities of such galaxies using the M99 or a different IRX-β relation would cause their SFRs to be underestimated, potentially by multiple orders of magnitude. Consequently, the UV-inferred star formation rate density may be more unreliable than is generally believed. This highlights an urgent need for current and future observatories, such as ALMA, the Large Millimeter Telescope, and the Chajnantor Submillimeter Survey Telescope, to directly constrain the obscured SFRs of galaxies at higher redshift and lower SFRs than are probed by existing surveys.

Chapter 6

Conclusion

Understanding galaxy formation as a whole is a very difficult task in that the proper theoretical framework has to be able to describe different disjoint observations and yet be simple and comprehensible. Key observations that a proper theory needs to explain include the following: 1) The evolution of the luminosity function of galaxies. 2) The observed number counts in different bands. 3) The observed background emission from UV to FIR. 4) The correlation function of different classes of galaxies and their cross correlation function with quasars and background light. 5) The dead versus active dichotomy that is present out to redshifts $z < 3$. 6) The main sequence of star formation that is observed out to redshifts $z < 4$. 7) The size evolution of galaxies. 8) The morphological transformations of galaxies and 9) the star formation rate density evolution.

All the above are entangled with each other such that it is not possible to give

a comprehensible picture that explains a specific observation without affecting our knowledge about the rest of the observations. For example, the observations of SMGs at high redshifts can not be interpreted only through the lens of dust content of galaxies and star formation rate density at high redshift. The observed correlation function of SMGs suggests they reside in halos with mass $M > 10^{13} M_{\odot}$ but it is not yet known how a galaxy can have access to cold gas reservoir in such massive halos in order to explain the estimated SFR needed to account for SMG's UV to FIR luminosities. Therefore, we need to think more about our dark matter halo model for the SMGs. Meanwhile our observations need to be critically examined and carefully modeled and interpreted.

In this thesis we have examined in detail current theoretical models for dust obscuration, scattering and emission in galaxies. We have looked at semi analytic approaches and more sophisticated RT solutions. Each approach comes with its advantages and disadvantages. For example, the simple dust treatment applied in the SAMs' framework, although computationally cheap to provide large statistical sample, has limited power to explain detailed UV-FIR observations. The RT simulations on the other hand, although more physically motivated, are computationally very expensive (in that as of writing this thesis, there is no cosmological simulation with galaxies being post-processed with dusty RT with sufficient resolution and volume to adequately assess the validity of the simulations framework in the light of NIR-FIR observations). Furthermore, the RT techniques used in the cosmological simulations

still rely on sub-grid assumptions that can significantly impact the final outcome of these simulations (see FIRE suite of simulations outputs, Hopkins et al., 2014b).

The outcome of the hydro simulations (for example in the case of tidal disruption of the sub-halos) are sometimes parametrized and implemented in the SAM framework. This should also be done in the context of the RT simulations with caution. Galaxies that are processed in RT simulations are not necessarily the same as galaxies in the SAMs in nature. On the other hand, it is encouraging that for cosmological outputs, the SAMs run on the same merger trees that the hydro-cosmological simulations use.

Both of these approaches come with assumptions on different scales. The free parameters that need to be defined when performing dusty RT on the output of hydrodynamical simulation using the code SUNRISE (Jonsson, 2006; Jonsson et al., 2006, 2010) are as follows:

- The mass opacity of dust grains (κ), albedo (ω) and scattering phase function (angular distribution of the scattered photons) on wavelength. The phase function that is widely used is that of (Henyey & Greenstein, 1941):

$$\Phi_s(\cos\theta) = \frac{1-g^2}{4\pi(1+g^2-2g\cos\theta)^{3/2}}, \tag{6.1}$$

  where θ is the scattering angle and $g = \langle\cos\theta\rangle$, the phase function asymmetry, parameterizes the degree to which the scattering is isotropic or mostly forward/backward.

- The dust grain chemistry and size distribution which are normally adopted following model by Li & Draine (2001); Weingartner & Draine (2001). This is necessary if we are to model the emergent IR radiation, otherwise knowing κ, ω and g is enough.

- The dust to metal ratio (normally taken to be 0.4) however it is known to vary within a galaxy and be dependent on the metallicity of the system.

- the covering fraction of the photo-dissociation regions f_{PDR}.

- The compactness of stellar clusters and the volume of the simulation that is assigned to them.

- The luminosity function of the HII regions. In RT simulations it is assumed that the stellar clusters all have the same mass, or a massive one is divided into smaller ones all with the same mass. Distributing the stellar clusters following the HII LF of the observed galaxies would be an improvement.

In the case of SAMs, dust follows the cold gas component of the galaxy and the cold gas is modeled as an exponential profile ($\Sigma_{gas}(r) \propto e^{-r}$) similar to the stellar disk of the galaxies (Somerville et al., 2008a; Fontanot & Somerville, 2011; Somerville et al., 2012; Lu et al., 2013). This simple geometry is sufficient to match the observed low redshift galaxies' color by tuning the parameters of the model to follow the distribution of local star forming galaxies in ($\log L_{IR}/L_{FUV}$)- ($12 + \log(O/H)$) plane, as

well as fitting for the observed relation between $\log(L_{IR}/L_{FUV})$ and the total bolometric luminosity (L_{Bol}) of these galaxies. The parameters obtained through fitting these dependencies are very sensitive to the sample of galaxies that are chosen for tuning the models. For example, the local star forming galaxies in the SINGS sample likely give different fitting parameters than the sample of local galaxies compiled and studied by Buat et al. (2006). Other than the issue of finding fitting parameters, these types of dust treatments are formulated with redshift as a parameter. This redshift dependence is needed to match the observed UV luminosity function of galaxies across cosmic time (Somerville et al., 2008a). These are often ad-hoc treatment when it comes to redshift evolution, because there is often no physics behind the redshift evolution parametrization. Here we highlight a few short comings of the current SAM dust treatment:

- The simple assumption that dust follows the cold gas needs to be revisited in the light of new simulations carried by Khakhaleva-Li & Gnedin (2016) where the dust in the HII regions must be sublimated in order to match the observed UV luminosity function of galaxies at $z > 4$.

- Hopkins & Lee (2015) show that the dynamics of dust is not coupled with the gas in turbulent molecular clouds and the behavior of dust depends on the grain size.

- The scattering of the UV photons is generally swept under the rug and it is

assumed that the UV photons only experience absorption by dust. It would not be sufficient to model a fraction of UV photons to be scattered off of the dust grains. The scattered photons can severely change the rest-frame colors of the galaxies.

- If the star formation occurs in the outskirts of the galaxies, some of the OB stars will not be enshrouded in dust and will contribute significantly to the observed UV emission and make the galaxy look blue while being FIR bright at the same time. This decoupling of the young stars and their contribution to the color of the galaxy is observed in the hydro-sims but the implantation of this is not yet done in the SAMs.

There are many open avenues to improve the treatment of dust in models of galaxy formation. The final goal to constrain all the dust parameters would involve running a large MCMC simulation and this is only done in the context of SAM's parameters. We need to run a cosmological simulation with all the dust physics implemented. Then compute the observed colors of each galaxy based on sophisticated RT simulation. Then make the images of the sky in all the observed bands from FUV to FIR and compare to the observed images from HST to *Herschel*. Then update all the variables and re-run the cosmological simulation again and perform the χ^2 statistics and update the priors on each parameter involved in the simulation until the chains are converged. However, the prospect for having such computational power is dim and alternative path ways needs to be thought of to constrain the models using all the information

available from all the telescopes. Nevertheless, what can be done to accelerate the convergence in this large MCMC calculation? We should design observations that can immediately disfavor a large part of the parameter space that still needs to be explored and thereby further constrain the still possible models. Besides designing deep FIR telescope with lower levels of confusion noise, we need to think about best approaches to constrain the cold-gas fraction of galaxies and its evolution with redshift. The search for proxies (such as ion line ratios) of the FIR emission that could be studied with near future telescopes such as JWST is another valuable approach that needs to be studied in detail.

Bibliography

Adelberger, K. L., & Steidel, C. C. 2000, arXiv.org, 218

Adelberger, K. L., Steidel, C. C., Shapley, A. E., Hunt, M. P., Erb, D. K., Reddy, N. A., & Pettini, M. 2004, The Astrophysical Journal, 607, 226

Agertz, O., & Kravtsov, A. V. 2015, The Astrophysical Journal, 804, 18

Agertz, O., Kravtsov, A. V., Leitner, S. N., & Gnedin, N. Y. 2013, The Astrophysical Journal, 770, 25

Akaike, H. 1974, IEEE Transactions on Automatic Control, 19, 716

Álvarez-Márquez, J., et al. 2016, Astronomy & Astrophysics, 587, A122

Armus, L., et al. 2009a, Publications of the Astronomical Society of Pacific, 121, 559

—. 2009b, 121, 559

Asano, R. S., Takeuchi, T. T., Hirashita, H., & Nozawa, T. 2013, Monthly Notices of the Royal Astronomical Society, 432, 637

Barcons, X. 1992, The Astrophysical Journal

Barcons, X., & Fabian, A. C. 1990, Monthly Notices of the Royal ...

Bartlett, J. G., & Melin, J. B. 2006, Astronomy & Astrophysics, 447, 405

BIBLIOGRAPHY

Battisti, A. J., Calzetti, D., & Chary, R. R. 2016, The Astrophysical Journal, 818, 13

Baugh, C. M., Lacey, C. G., Frenk, C. S., Granato, G. L., Silva, L., Bressan, A., Benson, A. J., & Cole, S. 2005a, Monthly Notices of the Royal Astronomical Society, 356, 1191

—. 2005b, 356, 1191

—. 2005c, 356, 1191

Beckwith, S., Stiavelli, M., & Koekemoer, A. M. 2006, The Astronomical ...

Bell, E. F., Gordon, K. D., Kennicutt, R. C. J., & Zaritsky, D. 2002, The Astrophysical Journal, 565, 994

Bernhard, E., Béthermin, M., Sargent, M., Buat, V., Mullaney, J. R., Pannella, M., Heinis, S., & Daddi, E. 2014, Monthly Notices of the Royal Astronomical Society, 442, 509

Bertin, E., & Arnouts, S. 1996, Astronomy and Astrophysics Supplement ...

Béthermin, M., et al. 2012, 757, L23

Béthermin, M., Wang, L., Doré, O., Lagache, G., Sargent, M., Daddi, E., Cousin, M., & Aussel, H. 2013, MNRAS, 557, A66

Blain, A. W., Ivison, R. J., & Smail, I. 1998, Monthly Notices of the Royal Astronomical Society, 296, L29

Boquien, M., et al. 2012, Astronomy & Astrophysics, 539, A145

—. 2016, arXiv.org, arXiv:1603.09340

Boselli, A., et al. 2010, Publications of the Astronomical Society of the Pacific, 122,

BIBLIOGRAPHY

261

Bouwens, R. J., et al. 2009, The Astrophysical Journal, 705, 936

—. 2012, The Astrophysical Journal, 754, 83

—. 2014, The Astrophysical Journal, 793, 115

Bowler, R. A. A., et al. 2015, Monthly Notices of the Royal Astronomical Society, 452, 1817

Boyer, M. L., et al. 2015a, The Astrophysical Journal, 800, 51

—. 2015b, The Astrophysical Journal Supplement Series, 216, 10

Brassington, N. J., Zezas, A., Ashby, M. L. N., Lanz, L., Smith, H. A., Willner, S. P., & Klein, C. 2015, ApJS, 218, 6

Bruzual, G., & Charlot, S. 2003, 344, 1000

Buat, V., et al. 2011, Astronomy & Astrophysics, 533, A93

—. 2007, 173, 404

—. 2006, arXiv.org, 404

Burgarella, D., Buat, V., Gruppioni, C., Cucciati, O., Heinis, S., & Team, t. P. H. 2013, arXiv.org, arXiv:1310.3497

Calzetti, D. 1997, The Astronomical Journal, 113, 162

—. 2001a, Publications of the Astronomical Society of the Pacific, 113, 1449

—. 2001b, Publications of the Astronomical Society of the Pacific, 113, 1449

Calzetti, D., Kinney, A. L., & Storchi-Bergmann, T. 1994a, The Astrophysical Journal, 429, 582

—. 1994b, 429, 582

Capak, P. L., et al. 2015, MNRAS, 522, 455

Casey, C. M., Narayanan, D., & Cooray, A. 2014a, MNRAS, 541, 45

Casey, C. M., et al. 2014b, 796, 95

—. 2014c, The Astrophysical Journal, 796, 95

Chakrabarti, S., Cox, T. J., Hernquist, L., Hopkins, P. F., Robertson, B., & Di Matteo, T. 2007, 658, 840

Chakrabarti, S., Fenner, Y., Cox, T. J., Hernquist, L., & Whitney, B. A. 2008, The Astrophysical Journal, 688, 972

Chakrabarti, S., & Whitney, B. A. 2008, The Astrophysical Journal, 690, 1432

Chanial, P., Flores, H., Guiderdoni, B., Elbaz, D., Hammer, F., & Vigroux, L. 2007, 462, 81

Chapman, S. C., Smail, I., Blain, A. W., & Ivison, R. J. 2004, 614, 671

Charlot, S., & Fall, S. M. 2000a, arXiv.org, 718

—. 2000b, 539, 718

Chary, R., & Elbaz, D. 2001a, 556, 562

—. 2001b, 556, 562

Condon, J. J. 1974, The Astrophysical Journal, 188, 279

Condon, J. J., et al. 2012, The Astrophysical Journal, 758, 23

Conroy, C. 2013, Annual Review of Astronomy and Astrophysics, 51, 393

Conroy, C., Schiminovich, D., & Blanton, M. R. 2010, The Astrophysical Journal,

718, 184

Cortese, L., et al. 2006a, 637, 242

—. 2006b, The Astrophysical Journal, 637, 242

—. 2014, Monthly Notices of the Royal Astronomical Society, 440, stu175

Cowley, W. I., Lacey, C. G., Baugh, C. M., & Cole, S. 2015, 446, 1784

Cox, T. J., Jonsson, P., Somerville, R. S., Primack, J. R., & Dekel, A. 2008, Monthly Notices of the Royal Astronomical Society, 384, 386

Crowder, J., & Cornish, N. J. 2004, Physical Review D, 70, 082004

da Cunha, E., Charlot, S., & Elbaz, D. 2008, Monthly Notices of the Royal Astronomical Society, 388, 1595

da Cunha, E., et al. 2013, The Astrophysical Journal, 766, 13

—. 2015, MNRAS, 806, 110

Daddi, E., et al. 2010, The Astrophysical Journal, 713, 686

Daddi, E., Cimatti, A., Renzini, A., Fontana, A., Mignoli, M., Pozzetti, L., Tozzi, P., & Zamorani, G. 2004, The Astrophysical Journal, 617, 746

Dahlen, T., et al. 2013, The Astrophysical Journal, 775, 93

Dale, D. A., et al. 2012, 745, 95

Dale, D. A., De Paz, A. G., & Gordon, K. D. 2007a, The Astrophysical ...

Dale, D. A., et al. 2007b, The Astrophysical Journal, 655, 863

Dale, D. A., & Helou, G. 2002a, 576, 159

—. 2002b, 576, 159

BIBLIOGRAPHY

Dale, D. A., Helou, G., Contursi, A., Silbermann, N. A., & Kolhatkar, S. 2001, 549, 215

Davé, R., Finlator, K., Oppenheimer, B. D., Fardal, M., Katz, N., Kereš, D., & Weinberg, D. H. 2010, Monthly Notices of the Royal Astronomical Society

De Geyter, G., Baes, M., Camps, P., Fritz, J., De Looze, I., Hughes, T. M., Viaene, S., & Gentile, G. 2014, 441, 869

De Geyter, G., et al. 2015, Monthly Notices of the Royal Astronomical Society, 451, 1728

De Looze, I., Baes, M., Fritz, J., & Verstappen, J. 2011, Monthly Notices of the Royal Astronomical Society, 419, 895

De Looze, I., et al. 2014, 571, A69

De Lucia, G., & Blaizot, J. 2007, 375, 2

Desert, F. X., Boulanger, F., & Puget, J. L. 1990, 237, 215

Devriendt, J. E. G., & Guiderdoni, B. 2000, 363, 851

Devriendt, J. E. G., Guiderdoni, B., & Sadat, R. 1999, 350, 381

Dopita, M. A., et al. 2005, The Astrophysical Journal, 619, 755

Draine, B. T. 2003a, The Astrophysical Journal, 598, 1017

—. 2003b, The Astrophysical Journal, 598, 1026

Draine, B. T., et al. 2007a, The Astrophysical Journal, 663, 866

—. 2007b, 663, 866

Draine, B. T., & Li, A. 2007, 657, 810

BIBLIOGRAPHY

Dunlop, J. S., McLure, R. J., Robertson, B. E., Ellis, R. S., Stark, D. P., Cirasuolo, M., & de Ravel, L. 2012, Monthly Notices of the Royal Astronomical Society, 420, 901

Dunne, L., Eales, S. A., & Edmunds, M. G. 2003, Monthly Notices of the Royal Astronomical Society, 341, 589

Dunne, L., et al. 2011a, Monthly Notices of the Royal Astronomical Society, 417, 1510

—. 2011b, Monthly Notices of the Royal Astronomical Society, 417, 1510

Dwek, E. 1998a, The Astrophysical Journal, 501, 643

—. 1998b, 501, 643

Dwek, E., et al. 2011, The Astrophysical Journal, 738, 36

Eckart, A., et al. 2012, SPIE Astronomical Telescopes + Instrumentation, 8445, 84451F

Edmunds, M. G., & Eales, S. A. 1998, Monthly Notices of the Royal Astronomical Society, 299, L29

Efstathiou, A., Rowan-Robinson, M., & Siebenmorgen, R. 2000, 313, 734

Egami, E., et al. 2010, Astronomy & Astrophysics, 518, L12

Elbaz, D., et al. 2011, Astronomy & Astrophysics, 533, A119

Finkelstein, S. L., et al. 2012, The Astrophysical Journal, 756, 164

—. 2015, The Astrophysical Journal, 810, 71

Fischera, J., Dopita, M. A., & Sutherland, R. S. 2003, The Astrophysical Journal,

599, L21

Fontanot, F., & Somerville, R. S. 2011, Monthly Notices of the Royal Astronomical Society, 416, 2962

Fontanot, F., Somerville, R. S., Silva, L., Monaco, P., & Skibba, R. 2009a, Monthly Notices of the Royal Astronomical Society, 392, 553

—. 2009b, 392, 553

Foreman-Mackey, D., Hogg, D. W., Lang, D., & Goodman, J. 2013, Publications of the Astronomical Society of the Pacific, 125, 306

Fritz, J., Franceschini, A., & Hatziminaoglou, E. 2006, 366, 767

Fukugita, M. 2011, arXiv.org, arXiv:1103.4191

Fukugita, M., & Peebles, P. J. E. 2004, The Astrophysical Journal, 616, 643

Gall, C., Andersen, A. C., & Hjorth, J. 2011, Astronomy & Astrophysics, 528, A13

Gelman, A., & Rubin, D. B. 1992, Statistical science

Gnedin, N. Y. 2014, MNRAS, 793, 29

Goldader, J. D., Meurer, G., Heckman, T. M., Seibert, M., Sanders, D. B., Calzetti, D., & Steidel, C. C. 2002, The Astrophysical Journal, 568, 651

González, J. E., Lacey, C. G., Baugh, C. M., & Frenk, C. S. 2011, 413, 749

Gordon, K. D., Calzetti, D., & Witt, A. N. 1997, The Astrophysical Journal, 487, 625

Gordon, K. D., Misselt, K. A., Witt, A. N., & Clayton, G. C. 2001a, The Astrophysical Journal, 551, 269

—. 2001b, The Astrophysical Journal, 551, 269

Granato, G. L., Lacey, C. G., Silva, L., Bressan, A., Baugh, C. M., Cole, S., & Frenk, C. S. 2000a, The Astrophysical Journal, 542, 710

—. 2000b, The Astrophysical Journal, 542, 710

Granato, G. L., Ragone-Figueroa, C., Dominguez-Tenreiro, R., Obreja, A., Borgani, S., De Lucia, G., & Murante, G. 2015, Monthly Notices of the Royal Astronomical Society, 450, 1320

Grasha, K., Calzetti, D., Andrews, J. E., Lee, J. C., & Dale, D. A. 2013, arXiv.org, 174

Grogin, N. A., et al. 2011, The Astrophysical Journal Supplement, 197, 35

Groves, B., Dopita, M. A., Sutherland, R. S., Kewley, L. J., Fischera, J., Leitherer, C., Brandl, B., & van Breugel, W. 2008, 176, 438

Groves, B., et al. 2012, Monthly Notices of the Royal Astronomical Society, 426, 892

Gruppioni, C., et al. 2013, arXiv.org, 23

Guo, Q., & White, S. D. M. 2009, 396, 39

Hauser, M. G., et al. 1998, The Astrophysical Journal, 508, 25

—. 1984, Astrophysical Journal, 278, L15

Hayward, C. C., Behroozi, P. S., Somerville, R. S., Primack, J. R., Moreno, J., & Wechsler, R. H. 2013a, 434, 2572

Hayward, C. C., Jonsson, P., Kereš, D., Magnelli, B., Hernquist, L., & Cox, T. J. 2012, 424, 951

BIBLIOGRAPHY

Hayward, C. C., Kereš, D., Jonsson, P., Narayanan, D., Cox, T. J., & Hernquist, L. 2011a, 743, 159

Hayward, C. C., Narayanan, D., Jonsson, P., Cox, T. J., Kereš, D., Hopkins, P. F., & Hernquist, L. 2011b, in UP2010: Have Observations Revealed a Variable Upper End of the Initial Mass Function? ASP Conference Proceedings, 369–

Hayward, C. C., Narayanan, D., Kereš, D., Jonsson, P., Hopkins, P. F., Cox, T. J., & Hernquist, L. 2013b, 428, 2529

Hayward, C. C., & Smith, D. J. B. 2015, MNRAS, 446, 1512

Hayward, C. C., Torrey, P., Springel, V., Hernquist, L., & Vogelsberger, M. 2014a, Monthly Notices of the Royal Astronomical Society, 442, 1992

—. 2014b, MNRAS, 442, 1992

Henyey, L. G., & Greenstein, J. L. 1941, Astrophysical Journal, 93, 70

Hogg, D. W. 2001, The Astronomical Journal, 121, 1207

Hopkins, P. F., Kere, D., Oñorbe, J., Faucher-Giguère, C. A., Quataert, E., Murray, N., & Bullock, J. S. 2014a, Monthly Notices of the Royal Astronomical Society, 445, 581

Hopkins, P. F., Kereš, D., Oñorbe, J., Faucher-Giguère, C.-A., Quataert, E., Murray, N., & Bullock, J. S. 2014b, Monthly Notices of the Royal Astronomical Society, 445, 581

Hopkins, P. F., & Lee, H. 2015, arXiv.org, 4174

Hopkins, P. F., Younger, J. D., Hayward, C. C., Narayanan, D., & Hernquist, L.

2010a, 402, 1693

—. 2010b, MNRAS, 402, 1693

Howell, J. H., et al. 2010a, 715, 572

—. 2010b, The Astrophysical Journal, 715, 572

James, A., Dunne, L., Eales, S., & Edmunds, M. G. 2002, Monthly Notices of the Royal Astronomical Society, 335, 753

Jonsson, P. 2006, Monthly Notices of the Royal Astronomical Society, 372, 2

Jonsson, P., Cox, T. J., Primack, J. R., & Somerville, R. S. 2006, The Astrophysical Journal, 637, 255

Jonsson, P., Groves, B. A., & Cox, T. J. 2010, Monthly Notices of the Royal Astronomical Society, 403, 17

Kajisawa, M., Morishita, T., Taniguchi, Y., Kobayashi, M. A. R., Ichikawa, T., & Fukui, Y. 2015, The Astrophysical Journal, 801, 134

Kelly, B. C., Shetty, R., Stutz, A. M., Kauffmann, J., Goodman, A. A., & Launhardt, R. 2012, MNRAS, 752, 55

Kennedy, G. M., & Wyatt, M. C. 2012, Monthly Notices of the Royal Astronomical Society, 426, 91

Kennicutt Jr, R. C., et al. 2003a, Publications of the Astronomical Society of the Pacific, 115, 928

—. 2003b, Publications of the Astronomical Society of the Pacific, 115, 928

Khakhaleva-Li, Z., & Gnedin, N. Y. 2016, arXiv.org, arXiv:1601.00641

BIBLIOGRAPHY

Kirkpatrick, A., Pope, A., Sajina, A., Roebuck, E., Yan, L., Armus, L., Díaz-Santos, T., & Stierwalt, S. 2015, The Astrophysical Journal, 814, 9

Koekemoer, A. M., et al. 2011, The Astrophysical Journal Supplement, 197, 36

Kong, X., Charlot, S., Brinchmann, J., & Fall, S. M. 2004, Monthly Notices of the Royal Astronomical Society, 349, 769

Koprowski, M. P., et al. 2016, MNRAS

Kovács, A., et al. 2010, The Astrophysical Journal, 717, 29

Kriek, M., & Conroy, C. 2013a, 775, L16

—. 2013b, 775, L16

Lacey, C. G., Baugh, C. M., Frenk, C. S., Benson, A. J., Orsi, A., Silva, L., Granato, G. L., & Bressan, A. 2010, MNRAS, 405, 2

Lacey, C. G., Baugh, C. M., Frenk, C. S., Silva, L., Granato, G. L., & Bressan, A. 2008, MNRAS, 385, 1155

Laidler, V. G., et al. 2007, Publications of the Astronomical Society of the Pacific, 119, 1325

Lanz, L., Hayward, C. C., Zezas, A., Smith, H. A., Ashby, M. L. N., Brassington, N., Fazio, G. G., & Hernquist, L. 2014, 785, 39

Lanz, L., et al. 2013, The Astrophysical Journal, 768, 90

Lee, N., et al. 2013, MNRAS, 778, 131

Lee, S.-K., Ferguson, H. C., Somerville, R. S., Giavalisco, M., Wiklind, T., & Dahlen, T. 2014, The Astrophysical Journal, 783, 81

BIBLIOGRAPHY

Lee, S. K., Ferguson, H. C., Somerville, R. S., Wiklind, T., & Giavalisco, M. 2010, 725, 1644

Li, A., & Draine, B. T. 2001, The Astrophysical Journal, 554, 778

Lo Faro, B., Monaco, P., Vanzella, E., Fontanot, F., Silva, L., & Cristiani, S. 2009, 399, 827

Lu, Y., Wechsler, R. H., Somerville, R. S., & Croton, D. 2013, arXiv.org

Lu, Y., et al. 2014a, The Astrophysical Journal, 795, 123

—. 2014b, 795, 123

Madau, P., & Dickinson, M. 2014, Annual Review of Astronomy and Astrophysics, 52, 415

Maeder, A. 1992, Astronomy and Astrophysics (ISSN 0004-6361), 264, 105

Magdis, G. E., et al. 2012a, The Astrophysical Journal, 760, 6

—. 2012b, MNRAS, 760, 6

Magdis, G. E., Elbaz, D., Daddi, E., Morrison, G. E., Dickinson, M., Rigopoulou, D., Gobat, R., & Hwang, H. S. 2010a, The Astrophysical Journal, 714, 1740

Magdis, G. E., et al. 2010b, The Astrophysical Journal, 720, L185

Magnelli, B., et al. 2012, Astronomy & Astrophysics, 539, A155

—. 2013a, Astronomy & Astrophysics, 553, A132

—. 2013b, Astronomy & Astrophysics, 553, A132

Mancini, M., Schneider, R., Graziani, L., Valiante, R., Dayal, P., Maio, U., Ciardi, B., & Hunt, L. K. 2015, Monthly Notices of the Royal Astronomical Society: Letters,

451, L70

Mao, Y.-W., Kennicutt, R. C. J., Hao, C.-N., Kong, X., & Zhou, X. 2012, The Astrophysical Journal, 757, 52

Mao, Y.-W., Kong, X., & Lin, L. 2014, The Astrophysical Journal, 789, 76

Maraston, C., Pforr, J., Renzini, A., Daddi, E., Dickinson, M., Cimatti, A., & Tonini, C. 2010, MNRAS, 407, 830

Martínez-Galarza, J. R., et al. 2016, The Astrophysical Journal, 817, 76

Martini, P., Dicken, D., & Storchi-Bergmann, T. 2013, The Astrophysical Journal, 766, 121

McKinnon, R., Torrey, P., & Vogelsberger, M. 2016a, Monthly Notices of the Royal Astronomical Society, 457, 3775

—. 2016b, MNRAS, 457, 3775

Melchior, P., & Viola, M. 2012, Monthly Notices of the Royal Astronomical Society, 424, 2757

Ménard, B., & Fukugita, M. 2012, The Astrophysical Journal, 754, 116

Meurer, G. R., Heckman, T. M., & Calzetti, D. 1999a, The Astrophysical Journal, 521, 64

—. 1999b, 521, 64

Michałowski, M. J. 2015a, MNRAS, 577, A80

—. 2015b, Astronomy & Astrophysics, 577, A80

Misselt, K. A., Gordon, K. D., Clayton, G. C., & Wolff, M. J. 2001a, The Astrophys-

ical Journal, 551, 277

—. 2001b, 551, 277

Motta, V., et al. 2002, arXiv.org, 719

Muñoz Arancibia, A. M., Navarrete, F. P., Padilla, N. D., Cora, S. A., Gawiser, E., Kurczynski, P., & Ruiz, A. N. 2014, Monthly Notices of the Royal Astronomical Society, 446, 2291

Muñoz-Mateos, J. C., et al. 2009, The Astrophysical Journal, 703, 1569

Murdoch, H. S., Crawford, D. F., & Jauncey, D. L. 1973, Astrophysical Journal, 183, 1

Narayanan, D., et al. 2010a, MNRAS, 407, 1701

Narayanan, D., Hayward, C. C., Cox, T. J., Hernquist, L., Jonsson, P., Younger, J. D., & Groves, B. 2010b, 401, 1613

Negrello, M., Magliocchetti, M., Moscardini, L., De Zotti, G., Granato, G. L., & Silva, L. 2004, Monthly Notices of the Royal Astronomical Society, 352, 493

Nguyen, H. T., et al. 2010, Astronomy & Astrophysics, 518, L5

Niemi, S. M., Somerville, R. S., Ferguson, H. C., Huang, K. H., Lotz, J., & Koekemoer, A. M. 2012, MNRAS, 421, 1539

Noeske, K. G., et al. 2007, The Astrophysical Journal, 660, L43

Noll, S., et al. 2009, Astronomy & Astrophysics, 499, 69

Ostriker, J., & Silk, J. 1973, Astrophysical Journal, 184, L113

Oteo, I., et al. 2014, Monthly Notices of the Royal Astronomical Society, 439, 1337

—. 2013a, Astronomy & Astrophysics, L3

—. 2013b, Monthly Notices of the Royal Astronomical Society, 435, 158

Overzier, R. A., et al. 2011, The Astrophysical Journal Letters, 726, L7

Pacifici, C., Charlot, S., Blaizot, J., & Brinchmann, J. 2012, Monthly Notices of the Royal Astronomical Society, 421, 2002

Pacifici, C., et al. 2014, Monthly Notices of the Royal Astronomical Society, 447, 786

Pettini, M., Steidel, C. C., Adelberger, K. L., Dickinson, M., & Giavalisco, M. 1999, arXiv.org, 96

Pforr, J., Maraston, C., & Tonini, C. 2012, MNRAS, 422, 3285

Pilbratt, G. L., et al. 2010a, Astronomy & Astrophysics, 518, L1

—. 2010b, Astronomy & Astrophysics, 518, L1

Poglitsch, A., et al. 2010, Astronomy & Astrophysics, 518, L2

Pope, A., et al. 2008, The Astrophysical Journal, 675, 1171

Popescu, C. C., Tuffs, R. J., Dopita, M. A., Fischera, J., Kylafis, N. D., & Madore, B. F. 2011, Astronomy & Astrophysics, 527, A109

Porter, L. A., Somerville, R. S., Primack, J. R., & Johansson, P. H. 2014, MNRAS, 444, 942

Reddy, N., et al. 2012a, MNRAS, 744, 154

—. 2012b, The Astrophysical Journal, 744, 154

Rieke, G. H., Alonso-Herrero, A., Weiner, B. J., Pérez-González, P. G., Blaylock, M., Donley, J. L., & Marcillac, D. 2009a, MNRAS, 692, 556

—. 2009b, MNRAS, 692, 556

Robertson, B., Hernquist, L., Cox, T. J., Di Matteo, T., Hopkins, P. F., Martini, P., & Springel, V. 2006, 641, 90

Rowlands, K., Gomez, H. L., Dunne, L., Aragón-Salamanca, A., Dye, S., Maddox, S., da Cunha, E., & van der Werf, P. 2014a, MNRAS, 441, 1040

Rowlands, K., Gomez, H. L., Dunne, L., Aragón-Salamanca, A., Dye, S., Maddox, S., da Cunha, E., & Werf, P. v. d. 2014b, Monthly Notices of the Royal Astronomical Society, 441, 1040

Rujopakarn, W., Rieke, G. H., Eisenstein, D. J., & Juneau, S. 2011, MNRAS, 726, 93

Rujopakarn, W., Rieke, G. H., Weiner, B. J., Pérez-González, P., Rex, M., Walth, G. L., & Kartaltepe, J. S. 2013, The Astrophysical Journal, 767, 73

Ryan, R. E. J., et al. 2014, The Astrophysical Journal Letters, 786, L4

Safarzadeh, M., Ferguson, H. C., Lu, Y., Inami, H., & Somerville, R. S. 2015a, 798, 91

—. 2015b, The Astrophysical Journal, 798, 91

Safarzadeh, M., Hayward, C. C., Ferguson, H. C., & Somerville, R. S. 2016, The Astrophysical Journal, 818, 62

Scheuer, P. A. G. 1957, Mathematical Proceedings of the Cambridge Philosophical Society, 53, 764

Schmidt, S. J., Ménard, B., Scranton, R., Morrison, C. B., Rahman, M., & Hopkins,

BIBLIOGRAPHY

A. M. 2015, Monthly Notices of the Royal Astronomical Society, 446, 2696

Scoville, N., et al. 2007, 172, 1

—. 2015

Shapley, A. E. 2011, Annual Review of Astronomy and Astrophysics, 49, 525

Siebenmorgen, R., & Krügel, E. 2007, 461, 445

Silva, L., Fontanot, F., & Granato, G. L. 2012, Monthly Notices of the Royal Astronomical Society, 423, 746

Silva, L., Granato, G. L., Bressan, A., & Danese, L. 1998, 509, 103

Smail, I., et al. 2007, The Astrophysical Journal, 654, L33

Smith, D. J. B., et al. 2013, MNRAS, 436, 2435

Snyder, G. F., Cox, T. J., Hayward, C. C., Hernquist, L., & Jonsson, P. 2011, MNRAS, 741, 77

Snyder, G. F., Hayward, C. C., Sajina, A., Jonsson, P., Cox, T. J., Hernquist, L., Hopkins, P. F., & Yan, L. 2013, 768, 168

Somerville, R. S., & Davé, R. 2014, MNRAS

Somerville, R. S., Gilmore, R. C., Primack, J. R., & Domínguez, A. 2012, Monthly Notices of the Royal Astronomical Society, 423, 1992

Somerville, R. S., Hopkins, P. F., Cox, T. J., Robertson, B. E., & Hernquist, L. 2008a, Monthly Notices of the Royal Astronomical Society, 391, 481

—. 2008b, 391, 481

—. 2008c, 391, 481

Sparre, M., et al. 2014, The Astrophysical Journal, 785, 150

Sparre, M., Hayward, C. C., Feldmann, R., Faucher-Giguère, C.-A., Muratov, A. L., & Hopkins, P. F. 2015a, arXiv.org, arXiv:1510.03869

Sparre, M., et al. 2015b, 447, 3548

Springel, V. 2005, Monthly Notices of the Royal Astronomical Society, 364, 1105

Springel, V., Di Matteo, T., & Hernquist, L. 2005, Monthly Notices of the Royal Astronomical Society, 361, 776

Springel, V., & Hernquist, L. 2003, 339, 289

Stalevski, M., Fritz, J., Baes, M., Nakos, T., & Popović, L. Č. 2012, Monthly Notices of the Royal Astronomical Society, 420, 2756

Steidel, C. C., Adelberger, K. L., Giavalisco, M., Dickinson, M., & Pettini, M. 1999, The Astrophysical Journal, 519, 1

Steidel, C. C., Adelberger, K. L., Shapley, A. E., Pettini, M., Dickinson, M., & Giavalisco, M. 2003, The Astrophysical Journal, 592, 728

Steidel, C. C., Giavalisco, M., Pettini, M., Dickinson, M., & Adelberger, K. L. 1996a, ApJ, 462, L17

—. 1996b, 462, L17

Stierwalt, S., et al. 2014, MNRAS, 790, 124

Stone, J. M., Eisner, J. A., Monnier, J. D., Woillez, J., Wizinowich, P., Pott, J. U., & Ghez, A. M. 2012, The Astrophysical Journal, 754, 151

Symeonidis, M., et al. 2013, Monthly Notices of the Royal Astronomical Society, 431,

2317

Takagi, T., Arimoto, N., & Hanami, H. 2003, Monthly Notices of the Royal Astronomical Society, 340, 813

Takeuchi, T. T., & Ishii, T. T. 2004, The Astrophysical Journal, 604, 40

Takeuchi, T. T., Yuan, F.-T., Ikeyama, A., Murata, K. L., & Inoue, A. K. 2012, The Astrophysical Journal, 755, 144

Tateuchi, K., et al. 2015, 217, 1

Thacker, C., et al. 2013, The Astrophysical Journal, 768, 58

U, V., et al. 2012, 203, 9

van der Wel, A., et al. 2014, The Astrophysical Journal, 788, 28

Vargas, C. J., et al. 2014, The Astrophysical Journal, 783, 26

Watson, D., Christensen, L., Knudsen, K. K., Richard, J., Gallazzi, A., & Michałowski, M. J. 2015, MNRAS, 519, 327

Weingartner, J. C., & Draine, B. T. 2001, The Astrophysical Journal, 548, 296

Whitaker, K. E., van Dokkum, P. G., Brammer, G., & Franx, M. 2012, The Astrophysical Journal Letters, 754, L29

Witt, A. N., & Gordon, K. D. 1996a, The Astrophysical Journal, 463, 681

—. 1996b, 463, 681

—. 2000a, The Astrophysical Journal, 528, 799

—. 2000b, 528, 799

Wuyts, S., Cox, T. J., Hayward, C. C., Franx, M., Hernquist, L., Hopkins, P. F.,

BIBLIOGRAPHY

Jonsson, P., & van Dokkum, P. G. 2010, 722, 1666

Wuyts, S., et al. 2009, MNRAS, 700, 799

—. 2011, The Astrophysical Journal, 738, 106

Younger, J. D., Hayward, C. C., Narayanan, D., Cox, T. J., Hernquist, L., & Jonsson, P. 2009a, Monthly Notices of the Royal Astronomical Society: Letters, 396, L66

—. 2009b, 396, L66

Vita

Mohammadtaher Safarzadeh was born in Tehran, Iran, on August 30, 1985. He received a B.Sc. in material sciences from Iran university of science and technology in 2008. He then got a M.Sc. from Chalmers university of technology in Sweden majoring in space science and technology. In 2010, he moved to the U.S. and recieved a Ph.D. in astronomy at Johns Hopkins university in June 2016.